The Implementation of Evaporated Ethanol as an Alternative Fuel for the Natural Gas-Fired Power Plant in Killingholme.

Tijn van Eil

Technische Universiteit Delft

TU Delft Delft University of Technology

Challenge the future

The Implementation of Evaporated Ethanol as an Alternative Fuel for the Natural Gas-Fired Power Plant in Killingholme.

by

Tijn van Eil

in partial fulfillment of the requirements for the degree of

Master of Science
in Energy, FLow and Process Technology (Mechanical Engineering)

at the Delft University of Technology.

Supervisors:	Prof. dr. ir. S. Klein,	TU Delft
	S. Aukema,	Uniper
	C. Goy,	Uniper
Thesis committee:	Dr. ir. M. Pourquié,	TU Delft
	Dr. D. Abbott,	Uniper

TU Delft Delft University of Technology

Preface

This thesis will be my final project to conclude my Master's Degree in Mechanical Engineering at the Delft University of Technology. These past months have been challenging for me, but I have always enjoyed working on a project that was initiated to find solutions to decarbonize the industry. Luckily, I was not on my own, as I had a lot of support, guidance, and expertise from several individuals and institutions whom I am privileged to acknowledge.

This thesis project was performed in close collaboration with Uniper. My sincere appreciation extends to Uniper for their invaluable collaboration and provision of resources that made this research possible. In particular, I would like to thank some supervisors from Uniper. First of all, I would like to thank Sander Aukema for his support here in the Netherlands and his important role in the initiation phase of this project. Next, I want to thank David Abbott for his perfect guidance throughout the project. Working with you was a pleasure, and I appreciate that you reserved so much time for our discussions. Lastly, I want to thank Cath Goy for her support and for providing me with the right contacts within Uniper.

I would also like to express my sincerest gratitude to Prof. dr. ir. Sikke Klein for all his assistance and for guiding me (and the project) in the right direction. The consistent guidance and critical reflections were crucial factors for the success of this project. Additionally, I want to thank Dr. ir. Mathieu Pourquié for his guiding role. Although he was not directly involved in this thesis project, he was willing to make time to help me through my CFD study. And lastly, I want to thank Teja Donepudi for his interest and help in this project.

This project has provided me with valuable insights into the world of combustion. Hopefully, this project will contribute to finding the right solutions for the energy transition. Enjoy reading!

Tijn van Eil
Delft, January 2024

Abstract

Decarbonization is an important step to achieve the goals set by the Paris Agreement. Greenhouse gas emissions should be reduced to zero, and therefore, the reliability of fossil fuels should be reduced. This causes a shift of interest towards more renewable solutions. However, the intermittent nature of renewable energy sources such as solar and wind energy leaves a gap in the energy supply. Currently, this gap is still filled by natural gas, but biofuels could potentially help in decarbonizing this gap. Biofuels could be prevaporized and used as an alternative fuel within existing natural gas-fired power plants. Ethanol is an interesting biofuel as it has a relatively low boiling point, meaning that it is relatively easy to evaporate. Next to that, ethanol has a similar Wobbe Index (WI) compared to natural gas, meaning that it could be potentially used with only minor adjustments to the gas turbine. This research will focus on implementing ethanol as an alternative fuel for the Killingholme power plant, a 600 MW power plant in an open cycle gas turbine (OCGT) configuration that Uniper operates in the United Kingdom.

This research focused on the effect of ethanol on the process design and combustion characteristics, where the process design was only briefly touched upon. It was found that ethanol should be heated to a temperature of 467 K to be in vapor form at the relevant gas turbine conditions. A process design was made for the baseload operation, where the required heat for the evaporation process was provided by the flue gas flowing out of the gas turbine. Next to that, the use of ethanol requires slightly higher volume flow rates, meaning that the pipes and fittings should be adjusted to keep the desired fuel pressure. The effect of ethanol on combustion characteristics was researched by a kinetic modeling study and a CFD study focusing on fuel-air mixing, where the results will be compared to methane. A RANS study was performed for the CFD study, which showed that the use of ethanol results in a better quality of mixing. From the kinetic modeling study, it was found that ethanol has a lower autoignition delay time than methane. This will probably not lead to the autoignition of the fuel-air mixture in the mixing section, but it could lead to periodic flashes in regions close to the recirculation zones within the burner. It was also found that ethanol has a 78% higher laminar flame speed than methane. Next to that, it was found that ethanol has an effective Lewis number of 1.56 at the relevant gas turbine conditions, whereas methane has an effective Lewis number close to unity. From the laminar flame speed and the effective Lewis number, it was concluded that the use of ethanol results in an increase in turbulent flame speed. The increased turbulent flame speed and better quality of mixing of ethanol suggest a decrease in flame length. The decrease in flame length and increase in turbulent flame speed lead to higher flashback risks, but it is expected that this will be within the flashback margin of the burner. Based on the kinetic modeling study and the fuel-air mixing study, it was concluded that ethanol will have NOx emissions similar to methane and that the driving energy source of the combustion dynamics will probably shift to higher frequencies.

Recommendations for further research are the gas turbine's start-up, ethanol contaminants, extended CFD study of the burner, and the blending of ethanol and natural gas. Further research could complement the already promising results from this report, and eventually, this could lead to combustion tests where ethanol will be used as fuel.

Nomenclature

Abbreviations

AIT	Autoignition Temperature
CCGT	Combined-Cycle Gas Turbine
CO	Carbon monoxide
ERZ	External Recirculation Zone
FAR	Fuel-to-Air Ratio
HHV	Higher Heating Value
IRZ	Internal Recirculation Zone
JICF	Jet in crossflow
LHV	Lower Heating Value
LIF	Laser Induced Fluorescence
LPP	Lean, Premixed and Prevaporized
MWI	Modified Wobbe Index
NOx	Nitrogen oxides
OCGT	Open-Cycle Gas Turbine
PIV	Particle Image Velocimetry
RANS	Reynolds Averaging Navier-Stokes
UHC	Unburned hydrocarbons
WI	Wobbe Index

Symbols

S	Mass flow weighted standard deviation of the fuel distribution
G_τ	Axial flux of swirl momentum
α	Thermal diffusivity
β	Zeldovich number
ΔH_{comb}	Heat of combustion
δ_{ij}	Kronecker delta
$\dot{m}$	Mass flow rate
ϵ	Dissipation rate
κ	Von Kármán constant
μ	Dynamic viscosity
ν	Kinematic viscosity
ν_τ	Eddy viscosity
ω	Dissipation per unit turbulent kinetic energy
ϕ	Equivalence ratio
ρ	Density
τ_{ig}	Autoignition delay time
A	Area
D	Mass diffusivity
Da	Damköhler number
E_a	Activation energy
G_s	Specific gravity
G_x	Axial flux of axial momentum
J	Momentum flux ratio
K	Flame stretch rate
k	Turbulent kinetic energy
l_0	Length scale for turbulent eddies
L_M	Markstein length
Pr	Prandtl number
R	Universal gas constant
Re	Reynolds number
S_{ij}	Strain-rate tensor
S_L	Laminar flame speed
S_L^0	Laminar flame speed unstretched flame
S_T	Turbulent flame speed
T	Temperature
t	Time

T_{ad}	Adiabatic flame temperature	y^+	Wall coordinate
t_{ij}	Stress tensor	Ka	Karlovitz number
u'	Turbulent intensity	Le	Lewis number
u	Velocity	Ma	Markstein number
u^+	Dimensionless velocity	Sc	Schmidt number

List of Figures

List of Tables

Contents

1

Introduction

According to the Paris Agreement, the effects of climate change should be mitigated by limiting the temperature increase to $2°C$ with respect to the pre-industrial level, and preferably to a maximum of $1.5°C$ [22]. These goals can only be reached by striving for a net zero industry, where greenhouse gas emissions should be reduced to zero or balanced by removing these emissions. In the power generation sector, the focus is shifting from the use of fossil fuels, such as coal and natural gas, to renewable energy sources, such as wind and solar energy. This trend can also be observed in the United Kingdom as shown in Figure 1.1. It can be seen that coal was the dominant energy source in the nineties, where natural gas and renewables are currently the primary sources for electricity generation. The share of renewables in the fuel mix will only increase more in the future.

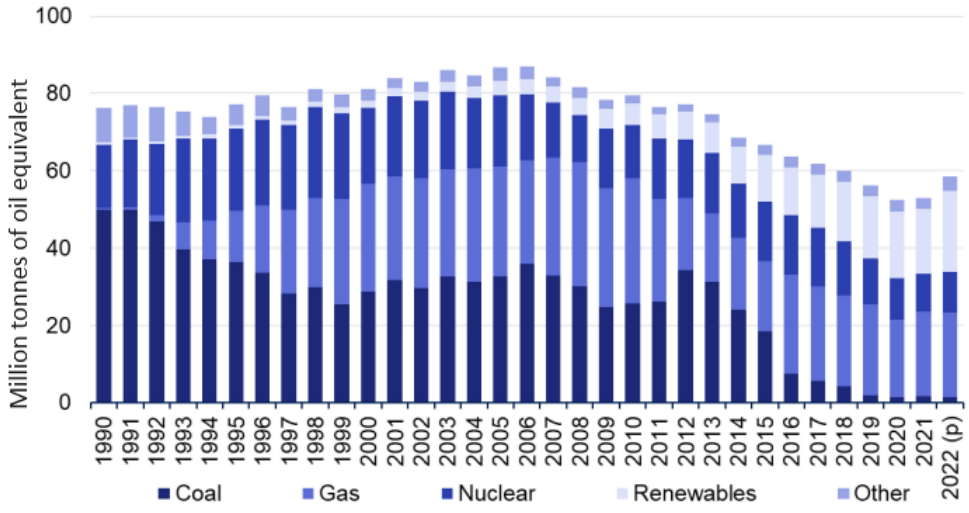

Figure 1.1: Fuel mix for the electricity generation in the United Kingdom between 1990-2022 [1].

However, due to their intermittent nature, solar and wind energy can not solely supply all required energy in the future. The intermittency of these sources requires a complementing and reliable energy source. This gap is currently filled by natural gas, but the industry's focus will shift to using hydrogen and other biofuels to decarbonize the energy supply further. These biofuels are made from biomass so that a closed carbon cycle is established.

1.1. LPP Combustion of Ethanol

Traditionally, gas turbines in the power generation sector used combustors that host diffusion flames. However, due to stringent NOx emissions regulations, lean and premixed combustion became more desirable, and it is now the standard technology in many gas turbines. This is also the case for the

Killingholme power plant, which is a natural gas-fired power plant owned by Uniper.

Lean, premixed, and prevaporized (LPP) combustion offers the possibility of using biofuels as an alternative fuel within existing natural gas-fired power plants without requiring many alterations to the gas turbine. Liquid biofuels will be prevaporized and premixed with compressed air to mimic natural gas characteristics. A study has shown that the LPP combustion of biofuels could potentially lower the NOx emissions of a gas turbine during startup [23]. Ethanol is an interesting biofuel for LPP combustion, as it has a relatively low boiling point, which makes it relatively easy to vaporize [24]. Next to that, ethanol has a similar Wobbe Index (WI) compared to natural gas, meaning that it could be potentially used with only minor adjustments to the gas turbine. Another advantage of ethanol is that conventional bioethanol production is already significant as it is widely used in the transportation sector, pharmaceutical industry, and chemical industry, and it is used for producing alcoholic beverages [25]. The advantages of ethanol over methanol are the higher calorific value and slightly higher flashpoint of ethanol, and the fact that ethanol is less toxic when compared to methanol [18].

1.2. Killingholme

The Killingholme Power Station was originally built as a 900 MW natural gas-fired closed-cycle gas turbine (CCGT) power station and was commissioned in 1992. Later, parts of the Killingholme power station were removed, turning the power station into a 600 MW open-cycle gas turbine (OCGT) configuration. The Killingholme power station is located in North Lincolnshire, which is an area that is next to the Humber and is located on the east coast of Northern England. The area surrounding the Humber is very industrial and will be one of the UK's target locations for decarbonization.

Figure 1.2 gives an overview of Uniper's site in Killingholme when it was still operating in combined-cycle configuration. However, Killingholme is currently operating in an open-cycle configuration, and the steam turbine cycle was disassembled in 2016 by removing the chimneys of the heat-recovery steam generator, the steam turbines, and the cooling towers.

Figure 1.2: Uniper's Killingholme site before 2016 [2].

Siemens SGT5-2000E

The Uniper site in Killingholme has installed four 150 MW Siemens SGT5-2000E (or V94.2) gas turbines in open cycle configuration. As can be seen in Figure 1.3, the Siemens SGT5-2000E gas turbines have a sixteen-stage compressor, a four-stage turbine, and two silo combustors [26]. The Siemens SGT5-2000E gas turbines have a specified efficiency of 37.6% and 53.3% in, respectively, open and combined cycle application [3].

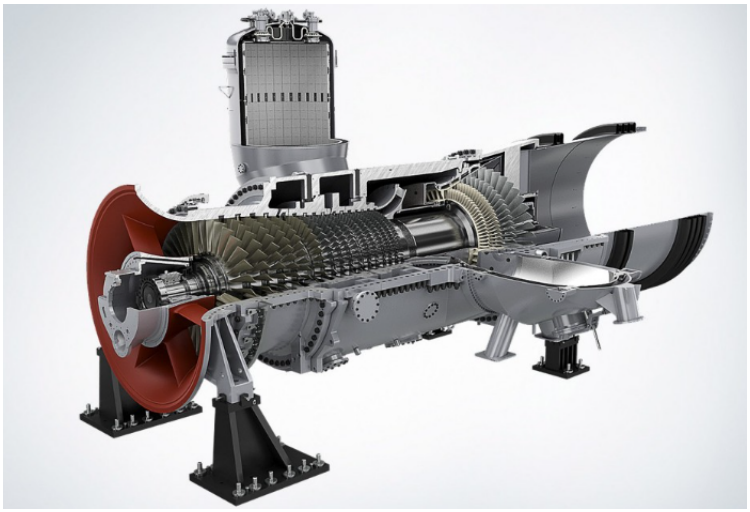

Figure 1.3: Siemens SGT5-2000E gas turbines [3].

Each silo combustor contains eight Siemens HR3 burners. These are revised hybrid burners, meaning they can operate in diffusion and premixed mode. A sketch of these HR3 burners can be seen in Figure 1.4. For the premixed mode, the main airflow will enter a diagonal swirler located concentrically around the diffusion burner. This diagonal swirler consists of twenty blades, and each blade contains five fuel inlets on each side of the blade. This is demonstrated in Figure 1.5.

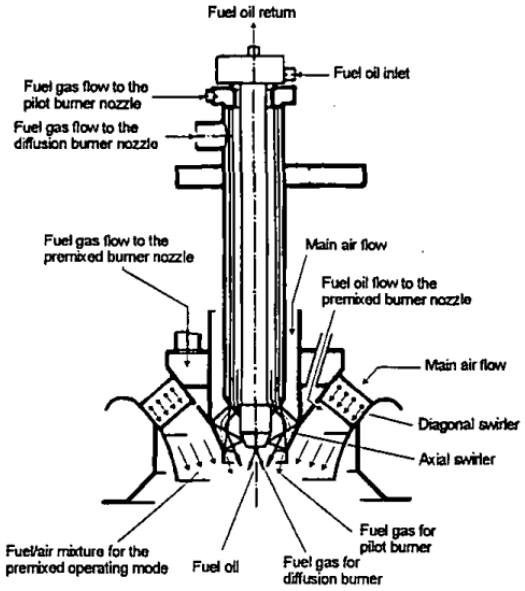

Figure 1.4: Sketch of the Siemens HR3 burner [4].

Figure 1.5: Actual cross section of a HR3 burner.

1.3. Research Objective

This research aims to get a better overview of how the implementation of ethanol will affect the Killingholme power plant. The study will focus on how ethanol affects the power plant's process design and the gas turbine's combustion characteristics, where a comparison will be made between ethanol and methane for the combustion characteristics. It is essential to remember that the research mainly focuses on combustion characteristics and that the process design is only discussed for completeness. The research question and relevant subquestions are listed below:

How does the use of ethanol affect the process design and the combustion characteristics of the natural gas-fired power plant at Killingholme?

Process Design:

- What are the opportunities for heat integration to evaporate the ethanol during baseload operation?
- How can ethanol be implemented in terms of storage and fuel handling?

Combustion Characteristics:

- Are there any increased risks of autoignition?
- How does the use of ethanol affect the flame length/position?
- Does the use of ethanol introduce any increased flashback/blowoff risks?
- How does the use of ethanol affect the NOx emissions?
- What would be the effect of ethanol on the combustion dynamics?

1.4. Thesis Outline

To answer the aforementioned research questions, the relevant theory behind process design and combustion will be discussed in Chapter 2. This chapter will be followed by Chapter 3, which will serve as the bridge between the theory and this research. Then, the effects of ethanol on the process design will be evaluated in Chapter 4. After the process design, the impact of ethanol on the combustion characteristics will be assessed with a kinetic modeling study (Chapter 5) and a fuel-air mixing study (Chapter 6). Then, all findings will be concluded in Chapter 7, and recommendations for future research will be given.

2

Theoretical Background

This chapter gives the theoretical background required to study the effect of the implementation of ethanol on the Killingholme power plant. First, Section 2.1 discusses the different thermodynamic cycles that form the basis for a power plant. Then, Section 2.2 and Section 2.3 give an introduction to turbulent flows and turbulence modeling. And finally, from Section 2.4 to the end of this chapter, relevant aspects regarding combustion in gas turbines will be discussed.

2.1. Thermodynamic Cycles

In the power generation sector, gas turbines are used in power plants to convert the chemical energy of a fuel into mechanical energy, which can be converted into electricity using a generator. The Brayton and Rankine cycle can be considered the building blocks of power plants; the Brayton cycle is the reference cycle for gas turbines and the Rankine cycle for steam turbines. Gas turbine cycles can be divided into open-cycle and combined-cycle gas turbines. The former depicts the situation where the flue gases from the gas turbine are exhausted into the environment, and the latter denotes the situation where the flue gas from the gas turbine is used as heat source for a Rankine cycle.

Brayton Cycle

The Brayton cycle is a continuous flow process using air as the working fluid. The air is drawn from the environment, and later on, it will be discharged back into the environment in the form of flue gas. The Brayton cycle consists of three components, as can be seen in Figure 2.1, namely, a compressor, a combustor (shown as a heat exchanger), and a turbine. There are four thermodynamic processes present in the Brayton cycle, which are summarized below:

- **1. Air compression (1-2)**
- **2. Heat addition (2-3)**
- **3. Flue gas expansion (3-4)**
- **4. Heat extraction (4-1)**

The four thermodynamic processes can also be seen in Figure 2.2, where a real Brayton cycle is denoted by the curves connecting $1-2-3-4$ [5]. First, air will be drawn from the environment and compressed to a higher pressure (1-2). The air compression stage can be considered adiabatic, as the heat transfer with the surroundings is negligible. Next to that, air compression is an irreversible process because of the increase in entropy. The increase in pressure causes an increase in the air temperature. The air compression stage requires external power for the process to be carried out.

Heat addition is the next thermodynamic process in the Brayton cycle (2-3). A fraction of the compressed air will be mixed with fuel before the mixture will be combusted. The combustion reaction turns the mixture into carbon dioxide and water, and this reaction releases heat into the process, which will

be absorbed by the combustion products. The heat addition can be considered quasi-isobaric, as the pressure loss is relatively small. Again, the process is irreversible due to an increase in entropy.

The combustion products will be cooled by the remaining compressed air (that was not used for the combustion reaction) to ensure acceptable temperature levels. The aforementioned mixture is denoted as flue gas, which will be fed into the turbine to be expanded (3-4). This flue gas expansion is again considered to be adiabatic and irreversible. The flue gas expansion causes a pressure drop in the flue gas, where the pressure ratio is usually similar to that of the compression stage. The decrease in pressure leads to a decrease in temperature. This thermodynamic process offers the possibility to extract work from the working fluid.

After expansion, the flue gas will be discharged into the environment (4-1). Heat will be extracted from the flue gas until the flue gas reaches the temperature of the environment. These pressure losses are rather small, so the heat extraction is considered to be quasi-isobaric. Next to that, this process is irreversible.

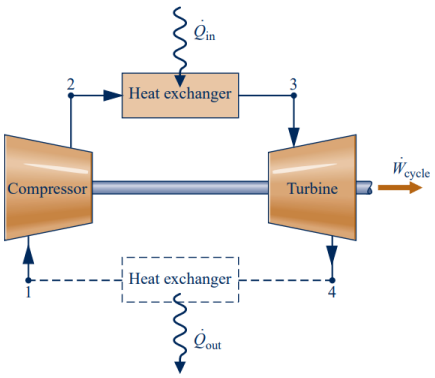

Figure 2.1: Schematic of the basic (open and closed) Brayton cycle [5].

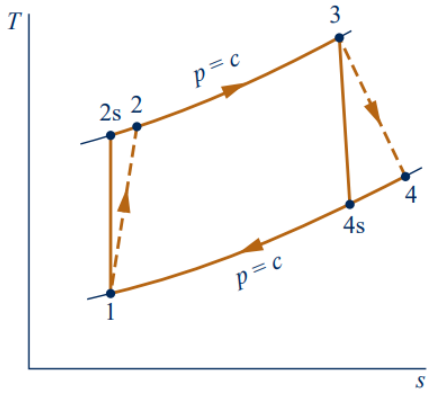

Figure 2.2: T-s diagram for the basic (ideal and real) Brayton cycle [5].

Rankine Cycle

In contrast to the Brayton cycle, the basic Rankine cycle uses water as the working fluid. The Rankine cycle is a closed thermodynamic cycle that converts heat into work, where the working fluid will undergo a phase change. The Rankine cycle is the reference cycle for steam plants. The basic Rankine cycle combines a steam generator, a turbine, a condenser, and a pump, which can be seen in Figure 2.3. A Rankine cycle, including a superheater and a reheater, consists of six thermodynamic processes, which are summarized below:

- **1. Water pumping (5-6)**
- **2. Heat addition (6-1)**
- **3. High-pressure vapor expansion (1-2)**
- **4. Vapor reheating (2-3)**
- **5. Low-pressure vapor expansion (3-4)**
- **6. Heat extraction (4-5)**

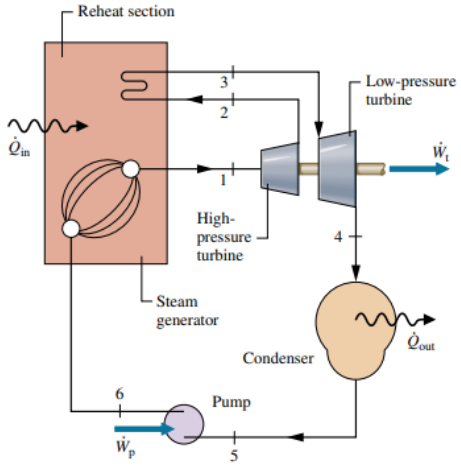

Figure 2.3: Schematic of the reheat Rankine cycle [5].

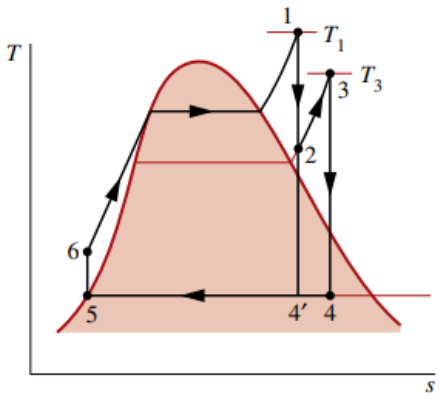

Figure 2.4: T-s diagram for the ideal reheat Rankine cycle [5].

Figure 2.4 shows the six thermodynamic processes of the real reheat Rankine cycle in a T-s diagram ($1-2-3-4-5-6$). First, the pressure of the water will be increased by the pump (5-6). The water pump is comparable to an air compressor, and following the same reasoning as for the Brayton cycle, water pumping is considered to be adiabatic and irreversible. The temperature increase of the fluid is usually minimal in the pumping stage. Power is required for the water pumping, but this is relatively low due to the high density of the liquid water.

Then the water is fed into the steam generator, where heat is added to the water (6-1). Water will be preheated before it is vaporized, resulting in steam, which will be superheated. These processes are quasi-isobaric and irreversible. The steam reaches its maximum temperature after the steam superheating. The superheated steam is then expanded for the first time in a steam turbine, where the enthalpy of the steam will be converted into work (1-2). The steam expansion results in a pressure and temperature drop. The low-pressure steam is then reheated, resulting in a low-pressure, high-temperature steam (2-3). The steam is again fed into the turbine for a last expansion stage, where the pressure and temperature are decreased (3-4). This leads to the working fluid being in the liquid-vapor region, and this is called wet steam. Both expansion stages are adiabatic and irreversible. Lastly, heat will be extracted from the working fluid, resulting again in water at starting conditions (4-5). The water is then fed into the pump, which results in a closed cycle.

2.2. Laminar and Turbulent Flows

Fluid flows can be classified based on the Reynolds number. The Reynolds number is a non-dimensional parameter, which is a ratio of the inertial forces to viscous forces within a fluid. The Reynolds number is given in Equation 2.1.

$$Re = \frac{uL}{\nu} \tag{2.1}$$

Where u is the characteristic velocity of the fluid, L is the characteristic length, and ν is the kinematic viscosity. Laminar flows occur for Reynolds numbers lower than 2300; for higher Reynolds numbers, the flow will be turbulent [7].

A flow is determined to be laminar when the viscous forces are dominant, and a turbulent flow depicts the situation where the inertial term dominates. Laminar flows are smooth and have a layered structure. Turbulent flows have a chaotic structure and are characterized by continuous velocity fluctuations. The difference between laminar and turbulent flows is visualized in Figure 2.5. The velocity fluctuations in turbulent flows are caused by eddies, which are described by the circular motion that deviates from the general fluid flow. Eddies vary in size, where the larger eddies tend to break down

into smaller eddies, which will, in turn, break down into even smaller eddies. This phenomenon, named the energy cascade, continues until the eddies have become so small that viscous forces cannot be neglected anymore.

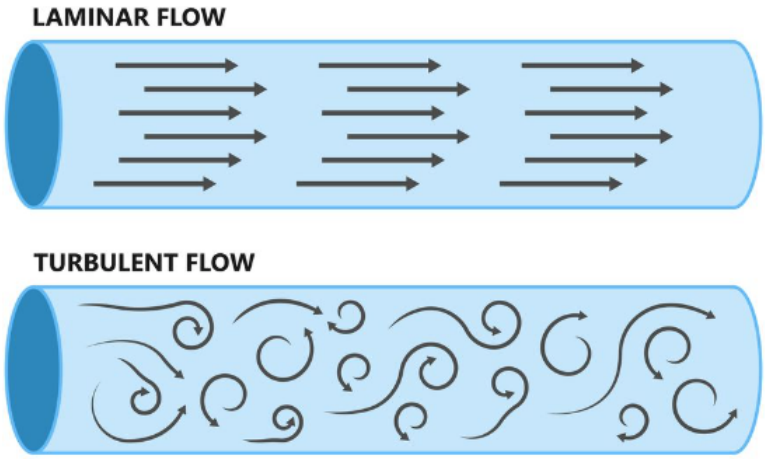

Figure 2.5: Visualization of the difference between laminar and turbulent flows [6].

Law of the Wall

Turbulent flows are affected by the presence of walls. In the regions close to the wall, viscous damping reduces the streamwise velocity component, and kinematic blocking causes reduced normal velocity fluctuations. Further away from the wall, the turbulence is rapidly enlarged by the production of turbulence kinetic energy due to large gradients in mean velocity.

Experiments have revealed that the near-wall region can be divided into three layers: the viscous sub-layer, where the flow is almost laminar, and molecular viscosity plays a crucial role in momentum, heat, or mass transfer. Then there is the fully turbulent layer, where turbulence dominates and the log-law (Equation 2.2 and Equation 2.3) is valid. Lastly, there is an interim region between the viscous sub-layer and the fully turbulent layer, where the effects of molecular viscosity and turbulence are equally significant.

$$u^+ = \frac{1}{\kappa} \ln y^+ + C^+ \tag{2.2}$$

$$y^+ = \frac{y u_\tau}{\nu}, \qquad u_\tau = \sqrt{\frac{\tau_w}{\rho}} \quad \text{and} \quad u^+ = \frac{u}{u_\tau} \tag{2.3}$$

Where κ is the Von Kármán constant, C^+ is a constant, u_τ is the shear velocity, and τ_w is the wall shear stress.

Figure 2.6 shows the three aforementioned layers. In Figure 2.6, the black line denotes the actual relationship between u^+ and y^+. It can be seen that in the viscous sub-layer, the actual relationship is best described by the blue line, which equals $u^+ = y^+$. In the fully-turbulent layer, the black line follows the green line, which is the log-law.

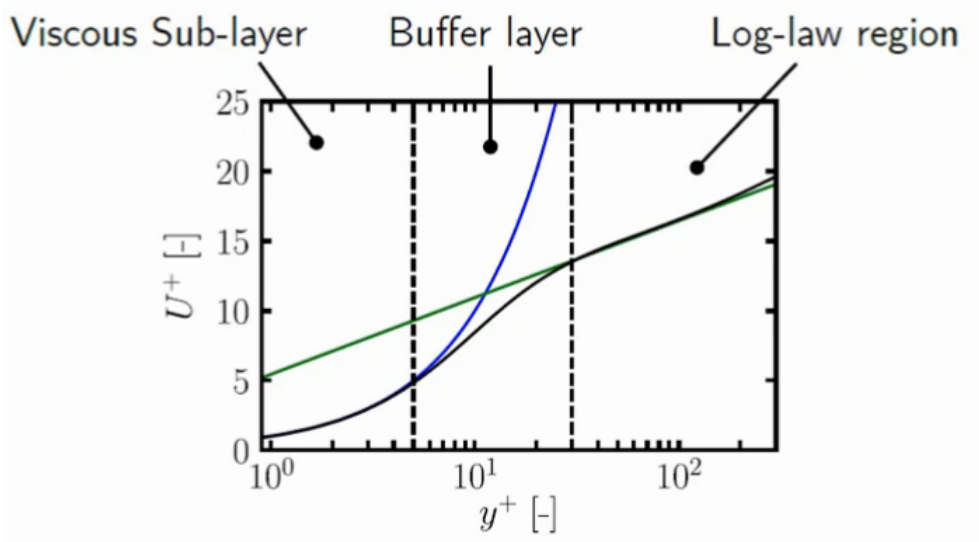

Figure 2.6: Boundary layer division according to the Law of the Wall [7].

2.3. Turbulence Modeling

The Navier-Stokes equations form the basis of fluid mechanics and are derived from the conservation of mass, momentum, and energy. The differential form of the equations for the conservation of mass and momentum are respectively given by Equation 2.4 and Equation 2.5 [7].

$$\frac{\partial \rho}{\partial t} + \frac{\partial}{\partial x_i}(\rho u_i) = 0 \tag{2.4}$$

where ρ is the density, t is the time, u is a velocity vector, x is a positional vector.

$$\frac{\partial}{\partial t}(\rho u_i) + \frac{\partial}{\partial x_j}(\rho u_i u_j) = -\frac{\partial p}{\partial x_i} + \frac{\partial t_{ij}}{\partial x_j} \tag{2.5}$$

Where t_{ij} is the stress tensor, which is second-order and symmetric. Assuming a Newtonian fluid, this stress tensor can be defined as $t_{ij} = \mu S_{ij}$. μ is the dynamic viscosity and S_{ij} is the strain-rate tensor and is defined as $S_{ij} = (\frac{\partial u_i}{\partial x_j} + \frac{\partial u_j}{\partial x_i}) - \frac{2}{3}\frac{\partial u_k}{\partial x_k}\delta_{ij}$. δ_{ij} denotes the Kronecker delta.

Reynolds and Favre Averaging

To save computational time, Reynolds Averaging Navier-Stokes (RANS) simulations solve the aforementioned Navier-Stokes equations by dividing flow variables into a mean and a fluctuating component, as is shown in Equation 2.6.

$$\phi_i(x,t) = \overline{\phi_i}(x,t) + \phi_i'(x,t) \tag{2.6}$$

Where the mean of the flow variable is determined by time averaging, as can be seen in

$$\overline{\phi_i}(x,t) = \lim_{T\to\infty} \frac{1}{T} \int_t^{t+T} \phi_i(x,t)dt \tag{2.7}$$

The density is assumed to be constant for incompressible flows, which simplifies the continuity equation to $\frac{\partial u_i}{\partial x_i} = 0$. Reynolds averaging the continuity and momentum equations leads to the RANS equations for incompressible flows, given by Equation 2.8 and Equation 2.9. As can be seen, an extra term was introduced to the momentum equation in the form of $\overline{u_i' u_j'}$, which is called the Reynolds-stress tensor. The Reynolds-stress tensor is second-order and symmetric and is a direct result of Reynolds averaging. The addition of the Reynolds-stress tensor leads to six extra unknowns and should be modeled to solve the RANS equations.

$$\frac{\partial \overline{u_i}}{\partial x_i} = 0 \tag{2.8}$$

$$\frac{\partial \overline{u_i}}{\partial t} + \frac{\partial \overline{u_i u_j}}{\partial x_j} = -\frac{1}{\rho}\frac{\partial \overline{p}}{\partial x_i} + \frac{\partial}{\partial x_j}[\nu S_{ij} - \overline{u_i' u_j'}] \tag{2.9}$$

When considering a compressible flow, extra unclosed terms will be introduced as the density is not constant anymore and will have a fluctuating component. Favre introduced a mass average of the velocity $\tilde{u_i}$ in the compressible Navier-Stokes equations. For Favre averaging of the velocity, the fluctuating part of the velocity is given as u_i''. The compressible RANS equations are given by [7]:

$$\frac{\partial \overline{\rho}}{\partial t} + \frac{\partial}{\partial x_i}(\overline{\rho}\tilde{u_i}) = 0 \tag{2.10}$$

$$\frac{\partial}{\partial t}(\overline{\rho}\tilde{u_i}) + \frac{\partial}{\partial x_j}(\overline{\rho}\tilde{u_i}\tilde{u_j}) = -\frac{\partial \overline{p}}{\partial x_i} + \frac{\partial}{\partial x_j}[\overline{t_{ji}} - \overline{\rho u_j'' u_i''}] \tag{2.11}$$

$$\begin{aligned}\frac{\partial}{\partial t}\left[\bar{\rho}\left(\tilde{e} + \frac{\tilde{u_i}\tilde{u_i}}{2}\right) + \frac{\overline{\rho u_i'' u_i''}}{2}\right] + \frac{\partial}{\partial x_j}\left[\bar{\rho}\tilde{u_j}\left(\tilde{h} + \frac{\tilde{u_i}\tilde{u_i}}{2}\right) + \tilde{u_j}\frac{\overline{\rho u_i'' u_i''}}{2}\right] \\ = \frac{\partial}{\partial x_j}\left[-q_j - \overline{\rho u_j'' h''} + \overline{t_{ji} u_i''} - \overline{\rho u_j'' \frac{1}{2} u_i'' u_i''}\right] + \frac{\partial}{\partial x_j}\left[\tilde{u_i}\left(\bar{t}_{ij} - \overline{\rho u_i'' u_j''}\right)\right]\end{aligned} \tag{2.12}$$

Closing the Compressible RANS Equations

This section briefly describes some approximations that are used to close the terms of Equation 2.11 and Equation 2.12 [7].

Reynolds-Stress Tensor

The Reynolds-Stress Tensor can be related to flow variables using the Boussinesq approximation, which is given by Equation 2.13.

$$\bar{\rho}\tau_{ij} \equiv \overline{-\rho u_i'' u_j''} = 2\mu_T\left(S_{ij} - \frac{1}{3}\frac{\partial \tilde{u}_k}{\partial x_k}\delta_{ij}\right) - \frac{2}{3}\bar{\rho}k\delta_{ij} \tag{2.13}$$

When an incompressible flow is considered, the term $-\frac{1}{3}\frac{\partial \tilde{u}_k}{\partial x_k}\delta_{ij}$ will be equal to zero.

Turbulent Kinetic Energy

The term $\frac{\overline{\rho u_i'' u_i''}}{2}$ denotes the turbulent kinetic energy per unit volume k. This gives us:

$$\frac{1}{2}\overline{\rho u_i'' u_i''} = \bar{\rho}k \tag{2.14}$$

Turbulent Heat-Flux Vector

The most used approximation to close the turbulent heat-flux vector q_{T_j} is the classical analogy between momentum and heat transfer as proposed by Reynolds. This is given by

$$q_{T_j} = \overline{\rho u_j'' h''} = -\frac{\mu_T c_p}{Pr_T}\frac{\partial \tilde{T}}{\partial x_j} = -\frac{\mu_T}{Pr_T}\frac{\partial \tilde{h}}{\partial x_j} \tag{2.15}$$

Where the turbulent Prandtl number Pr_T is often assumed to be 0.89 or 0.9 [7]. This means the thermal diffusivity will be slightly larger than the momentum diffusivity.

Molecular Diffusion and Turbulent Transport

Molecular diffusion and turbulent transport are usually so small that they can be neglected for subsonic flows. However, they can be modeled by assuming that the terms are proportional to the turbulent kinetic energy gradient:

$$\overline{t_{ji}u_i''} - \overline{\rho u_j'' \frac{1}{2} u_i'' u_i''} = \left(\mu + \frac{\mu_T}{\sigma_k}\right) \frac{\partial k}{\partial x_j} \tag{2.16}$$

Where σ_k is the turbulent Prandtl number for k and is defined as a constant in the two-equation eddy viscosity models.

Two-Equation Eddy Viscosity Models

To close all terms in Equation 2.11 and Equation 2.12, two-equation eddy viscosity models determine the eddy viscosity ν_T (or μ_T for compressible flows) based on turbulence parameters and dimensional analysis. First, there is the $k-\epsilon$ model, which uses the turbulent kinetic energy k and the dissipation rate ϵ. Different versions of the $k-\epsilon$ model exist, but they all use the following relation:

$$\nu_T \sim \frac{k^2}{\epsilon}, \qquad l \sim \frac{k^{3/2}}{\epsilon} \tag{2.17}$$

Where l is the turbulent length scale.

Another two-equation eddy viscosity model is the $k-\omega$ model, where ω is defined as the dissipation per unit turbulence kinetic energy. This leads to the following relation:

$$\nu_T \sim \frac{k}{\omega}, \qquad l \sim \frac{k^{1/2}}{\omega}, \qquad \epsilon \sim \omega k \tag{2.18}$$

The difference between both models is that the $k-\omega$ model performs better in the viscous regions near the wall and is better in accounting for the effects of streamwise pressure gradients [27]. However, far away from the wall, $k-\epsilon$ models tend to perform better. The $k-\omega$ model becomes dependent on the boundary conditions for non-turbulent free streams, which may become unphysical [28]. The Menter SST model blends both aforementioned models. Close to the walls, the Menter SST model is similar to the $k-\omega$ model, but away from the walls, the $k-\epsilon$ model will be used [29]. The Menter SST model defines ϵ in terms of ω; therefore, an extra transport equation is not required. A blending function determines when the $k-\omega$ model or $k-\epsilon$ model is used.

The transport equations and constants for the realizable $k-\epsilon$ and Menter SST $k-\omega$ models can be found in Appendix A.

2.4. Combustion Theory

As explained in section 2.1, heat addition occurs in a gas turbine by a combustion reaction of the fuel and air mixture. This section gives an introduction to combustion theory based on some relevant combustion parameters.

Stoichiometric condition and Fuel-to-Air equivalence ratio

Combustion is a chemical reaction between a fuel and an oxidant, mainly occurring at high temperatures. A combustion reaction is exothermic, which means that heat will be released. Another result of a combustion reaction is the production of different by-products. The combustion reactions of ethanol and methane are given in Equation 2.19 and Equation 2.20. The combustion of methane releases 890kJ/mol of energy, and the combustion of ethanol releases 1367kJ/mol of energy [24]. It can be seen that the combustion of ethanol and methane produces water and carbon dioxide. As ethanol is made from organic materials, the carbon dioxide emissions are compensated.

$$C_2H_5OH + 3O_2 \longrightarrow 2CO_2 + 3H_2O \qquad \Delta H_{comb} = -890kJ/mol \tag{2.19}$$

$$CH_4 + 2O_2 \longrightarrow CO_2 + 2H_2O \qquad \Delta H_{comb} = -1367kJ/mol \tag{2.20}$$

An optimum fuel-to-oxygen ratio was considered for both combustion reactions, meaning the reactants are fully converted into carbon dioxide and water. This situation is known as the stoichiometric combustion. In other words, there is a specific mass ratio of fuel and air to ensure complete combustion, known as the stoichiometric fuel-to-air ratio FAR_{st}. Based on the molecular weights and the combustion reactions, the mass-based FAR_{st} of ethanol and methane were calculated to be respectively 0.10 and 0.055. The mixture is considered lean if the fuel and air mixture contains more air than the stoichiometric quantity. When the mixture contains less air than the stoichiometric quantity, the mixture is considered to be rich. This is best described by the fuel-to-air equivalence ratio, as given in Equation 2.21.

$$\phi = \frac{FAR}{FAR_{st}} \tag{2.21}$$

$\phi > 1$ means the mixture is rich and $\phi < 1$ denotes a lean mixture.

Adiabatic flame temperature

When a fuel-air mixture is assumed to burn adiabatically at a constant pressure, it can be deduced from a heat balance that the reactants' absolute enthalpy equals the products' absolute enthalpy. The adiabatic flame temperature T_{ad} is the temperature of the products reached under the aforementioned ideal conditions. As seen in Figure 2.7, the adiabatic flame temperature is a function of the equivalence ratio for the combustion of a specified mixture.

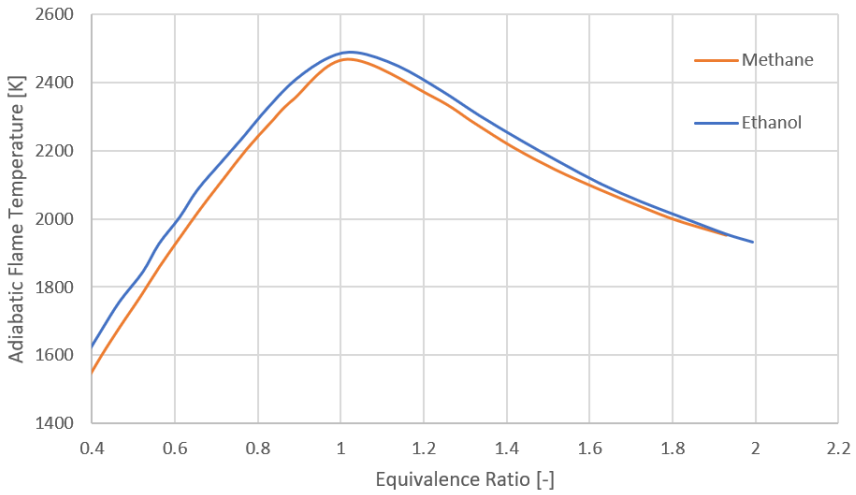

Figure 2.7: Adiabatic flame temperature versus the fuel-to-air equivalence ratio for ethanol and methane at typical gas turbine pressure and temperature conditions [8].

Heat of combustion and (Modified) Wobbe Index

Another important parameter in the combustion process is the heat of combustion, which indicates the amount of energy released during the combustion reaction of a specified amount of fuel. There are different forms of the heat of combustion, for example, the Lower Heating Value (LHV) and the Higher Heating Value (HHV). The HHV considers that all the produced water from a combustion reaction has condensed into a liquid, and for the LHV, it is assumed that all the produced water is vapor. This means that the difference between both values is caused by the latent heat of vaporization of water in the products.

A measure for the interchangeability of fuels is given as the Wobbe Index (WI) and is defined as in Equation 2.22. When considering gas turbines, similar WIs of two fuels mean that both fuels will have a similar energy output for the same fuel inlet pressure and valve settings [30]. In other words, fuels with the same WI will deliver the same heat for a given orifice.

$$WI = \frac{LHV}{\sqrt{G_s}} = \frac{LHV}{\sqrt{\frac{\rho_{f,ref}}{\rho_{air,ref}}}} \tag{2.22}$$

Where G_s is the specific gravity, and $\rho_{f,ref}$ and $\rho_{air,ref}$ are, respectively, the density of the fuel and air at specified standard conditions. It is also important to note that some literature uses the HHV instead of the LHV to define the WI. Equation (2.22) can be modified leading to Equation 2.23. This Modified Wobbe Index (MWI) has an extra density term, which makes the formula dependent on the fuel temperature [31].

$$MWI = LHV \frac{\rho_{f,(T)}}{\sqrt{\frac{\rho_{f,(T)}}{\rho_{air,ref}}}} \tag{2.23}$$

An empirical relation between the gas turbine power to the combustor pressure drop and MWI is given in Equation 2.24 [30]. The combustor pressure drop of a specified combustor geometry can be linked to the air and fuel flow rates. Gas turbine manufacturers usually specify a maximum allowable deviation of the MWI to ensure acceptable operation of the gas turbine.

$$P \propto WI\sqrt{\Delta p} \tag{2.24}$$

2.5. Chemical Kinetics

In chemistry, chemical kinetics is considered the study of the rate of chemical reactions and the factors that influence this rate. Insight into these chemical reaction rates provides information to predict the formation of products out of reactants. The rate law for a general case can be described by Equation 2.25 [32].

$$A + B + C \xrightarrow{k} D + E + F \qquad \pm \Delta H \tag{2.25}$$

For this reaction, the rate of consumption of species A is given as in Equation 2.26.

$$\frac{d[A]}{dt} = -k[A]^a[B]^b[C]^c \tag{2.26}$$

Where k is the rate coefficient of the reaction, [A], [B], and [C] are the molar concentrations of the different reactants, and a, b, and c are reaction orders of the different species. The reaction order quantifies the reaction rate's dependence on the reactants' concentrations and is often determined by experiments. The rate coefficient of the chemical reaction depends nonlinearly on the temperature. This relation is described by the adjusted Arrhenius Law given in Equation 2.27 [32, 33].

$$k = A'T^b e^{-\frac{E_a'}{RT}} \tag{2.27}$$

In this equation, A' is the pre-exponential factor, and E_a' is the activation energy of the reaction, which is defined as the minimum energy required for a chemical reaction to occur. R and T are the universal gas constant and the temperature, respectively.

Kinetic Mechanisms

A kinetic mechanism will be used for the study of different combustion parameters. A kinetic mechanism describes a chemical reaction and consists of information about species that will be formed due to intermediate reactions. Next, the kinetic mechanism consists of data for the A', b, and E_a values of each intermediate reaction to determine the reaction rates.

A broadly accepted mechanism for the combustion of methane is the GRI-Mech 3.0, developed at the Gas Research Institute of the University of Berkeley [21]. This mechanism consists of information about 53 species and 325 intermediate reactions and is validated with experiments determining the autoignition delay time, laminar flame speed, and species profiles. An example of some data present in GRI-Mech 3.0 is given in Table 2.1.

Table 2.1: Some data from the GRI-Mech 3.0 [21].

#	Reaction	A'	b	E_a
R18	$O + CH_3OH \Leftrightarrow OH + CH_2OH$	3.88e05	2.5	3100.0
R19	$O + CH_3OH \Leftrightarrow OH + CH_3O$	1.3e05	2.5	5000.0
R20	$O + C_2H \Leftrightarrow CH + CO$	5.0e13	0.0	0.0
R21	$O + C_2H_2 \Leftrightarrow H + HCCO$	1.35e07	2.0	1900.0

Chapter 5 will discuss kinetic mechanisms that can potentially be used to model the combustion of ethanol and methane.

2.6. Premixed versus Diffusion Flames

Flames in a combustion process can be ordered based on the level of premixedness and flow regime (laminar or turbulent). The difference between premixed and diffusion (or non premixed) flames will be discussed in this section, where the difference between laminar and turbulent flow was discussed in Section 2.2.

Premixed flames are the result of mixing the fuel and oxidizer prior to the combustion so that a homogeneous mixture is delivered to the combustion chamber. Diffusion flames denote the situation where the fuel and oxidizer are fed separately, and mixing occurs in the combustion chamber due to diffusion. The difference between premixed and diffusion flames regarding their fuel supply can be seen in Figure 2.8. Figure 2.9 shows actual premixed and diffusion flames where biogas (60% CH_4/40% CO_2) is used as fuel.

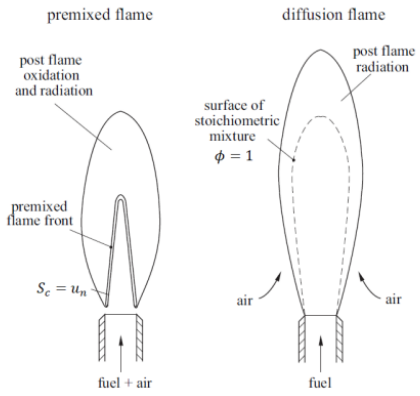

Figure 2.8: Schematic showing premixed and diffusion flames [9].

Figure 2.9: Premixed versus diffusion (non premixed) flames with biogas a fuel [10].

One of the main advantages of premixed combustion is an enhanced control of the combustion with respect to the equivalence ratio and, thereby, the flame temperature. Lean premixing is beneficial for pollutant formation because lower flame temperatures are maintained, resulting in less thermal NOx formation [32]. NOx formation mechanisms will be discussed later in this report. As it is crucial to minimize NOx emissions, only premixed flames will be discussed in this report.

2.7. Laminar Premixed Flames

Unstretched and Planar Flames

An essential property of laminar premixed flames is the laminar flame speed. The laminar flame speed is defined as the speed at which the flame front will propagate relative to the unburned reactants [34]. For the determination of the laminar flame speed, a planar flame is assumed to consist of a preheat zone and a reaction zone, as seen in Figure 2.10 [11]. The unburned reactants are continuously heated up to the ignition temperature by the upstream heat diffusion through the layers of the unburned gas [35].

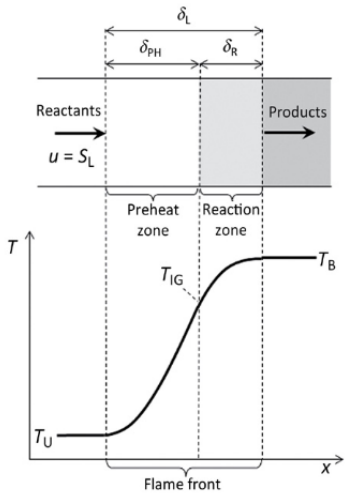

Figure 2.10: Overview of the different zones in a flame front [11].

There is heat diffusion from the reaction zone into the preheat zone. In contrast, there will be mass diffusion from the preheat zone to the reaction zone, as the reactants will diffuse due to a difference in concentration. The heat and mass diffusion can be related in the form of the Lewis number as given in Equation 2.28.

$$Le = \frac{\alpha}{D} \tag{2.28}$$

Where α and D denote the thermal and mass diffusivity, respectively. A Lewis number larger than unity means that the heat diffusion outbalances the diffusion of the reactants. For a Lewis number of unity, and by assuming that the preheat zone is significantly larger than the reaction zone, an estimation of the laminar flame speed S_L^0 could be given as [36]:

$$S_L^0 \sim \frac{D}{\delta_{PH}} \sim \frac{\alpha}{\delta_L} \tag{2.29}$$

Where S_L^0 is the laminar flame speed of an unstretched flame, and δ_{PH} and δ_L are, respectively, the preheat zone and flame front length. This relation can also be used to estimate the flame front length for different fuels with the use of their laminar flame speeds.

Bunsen Flame

The Bunsen burner is a classical device to produce a laminar premixed flame. Gaseous fuel, entering through an orifice, and air, entering through adjustable openings, are mixed in the mixing chamber. The flame will have a stationary conical shape when the flow is steady, premixed, and laminar. The kinematic balance for a Bunsen flame is described in Figure 2.11. The velocity of the unburnt mixture v_u approaches the flame front and can be deconstructed in a tangential component $v_{t,u}$ and a normal component $v_{n,u}$. When the flow has crossed the flame front, it is refracted, and the normal velocity component increases with the density ratio of the unburnt mixture over the burnt mixture. Since the flame front is stationary, the laminar flame speed should equal the normal component of the unburnt mixture. This means that the laminar flame speed can be related to the unburnt mixture velocity as in:

$$S_L^0 = v_u sin(a_c) \tag{2.30}$$

Where a_c is the cone angle.

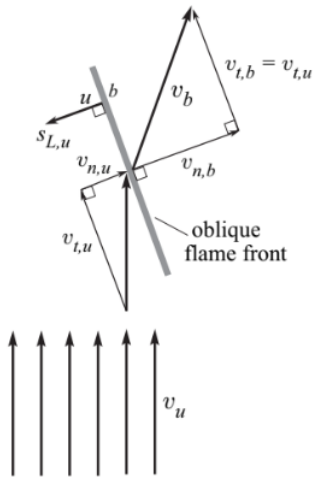

Figure 2.11: Kinematic balance for a bunsen flame [12].

Effect of Flame Stretch

The aforementioned relations for the laminar flame speed were deduced using the assumption that the flames were planar. However, planar flames are idealized; usually, flame fronts have curves and are stretched out. The flame speed is influenced by the flame stretch rate, which is given in Equation 2.31 [37].

$$K = \frac{1}{A}\frac{dA}{dt} \tag{2.31}$$

Where A is the surface of the flame front. A positive value of the flame stretch rate means the flame is stretched out, and a negative value indicates the flame is compressed.

Up until now, a Lewis number close to unity has been assumed. However, the actual Lewis number and stretch type influence the flame speed and stability. To explain this effect, a control volume in a convex flame as in Figure 2.12 is considered. It can be seen that the heat flux into the preheat zone is divergent, resulting in lower local temperatures and, thereby also, a lower flame speed. Next, it can be seen that the mass flux is convergent, leading to an increase in the flame speed. The net effect of the heat and mass flux is dependent on the Lewis number. When the Lewis number is larger than one, the heat flux will be larger than the mass flux, resulting in a lower flame speed. For a Lewis number smaller than one, the mass flux is larger than the heat flux, resulting in a higher flame speed. When the flame is concave with respect to the reactants, the opposite is true; a Lewis number larger than one leads to an increase in flame speed, and a Lewis number smaller than one leads to a decrease in flame speed. Hence, a Lewis number larger than one will have a stabilizing effect on the flame front as the flame speed increases/decreases for a concave/convex flame front.

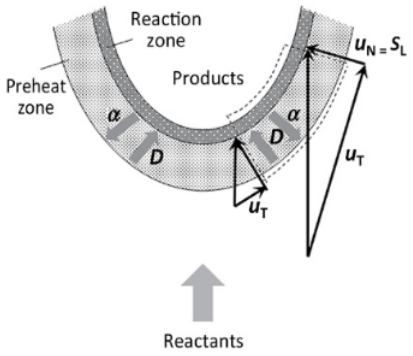

Figure 2.12: Overview of a convex flame front [11].

The flame speed of a stretched flame is related to the flame speed of an unstretched and planar flame, S_L^0. This relation is given in Equation 2.32 [38].

$$\frac{S_L^0}{S_L} = 1 + MaKa \tag{2.32}$$

Where Ma is the Markstein number, which is defined by Equation 2.33, and it describes the effect of the local heat release on changes in the flame surface. Ka is the Karlovitz number, which is defined by Equation 2.34. The Karlovitz number is defined as the ratio between the chemical timescale τ_c and the Kolmogrov timescale τ_η and will be further discussed in Section 2.8.

$$Ma = \frac{L_M}{\delta_L} \tag{2.33}$$

$$Ka = \tau_C K = \frac{\delta_L K}{S_L} \tag{2.34}$$

L_M in Equation 2.33 is defined as the Markstein length. Positive Markstein numbers and positive Markstein lengths indicate that the flame speed is decreased for an increase in stretch rate. Negative Markstein numbers mean that the flame speed is increased for an increase in stretch rate.

Computation of Effective Lewis Number

The effective Lewis number of a fuel and air mixture can be determined as follows [39]:

$$Le_{eff} = 1 + \frac{(Le_E - 1) + (Le_D - 1) * A}{1 + A} \tag{2.35}$$

Where Le_E and Le_D are the Lewis numbers (Equation 2.28) of, respectively, the excess and deficient reactants. For lean conditions, O_2 is the excess reactant, and the fuel (ethanol or methane) is the deficient reactant. These can be determined using flame parameters provided by the Cantera FreeFlame simulation. A is a measure of the mixture's strength and can be determined for lean conditions by Equation 2.36.

$$A = 1 + \beta(\frac{1}{\phi} - 1) \tag{2.36}$$

Where ϕ is the equivalence ratio and β represents the Zeldovich number, which is given by $\beta = E(T_b - T_u)/RT_b^2$. In this equation, T_b and T_u are the temperatures of the burned and unburned reactants, and R is the gas constant. E is the activation energy of the combustion reaction and can be determined using Equation 2.37 [40].

$$\frac{E}{R} = -2\frac{dln(\rho_u S_L)}{d(1/T_b)} \tag{2.37}$$

Where $\rho_u S_L$ should be calculated for different values of T_b using the Cantera FreeFlame simulation.

2.8. Turbulent Premixed Flames

Up to now, only laminar flames have been considered. However, there will be turbulent flow, explained in Section 2.2, in most practical applications of combustion. The velocity fluctuations of the turbulent flow cause curving and wrinkling of the flame front. Consequently, turbulent premixed flames will have an increased flame speed [32].

Flame Regimes

Different turbulent flame regimes can be determined based on velocity and length scale ratios. These premixed turbulent combustion regimes can be displayed in a so-called Borghi-Peters diagram, named after two researchers that contributed to this subject [41, 42]. First, a non-dimensional analysis should be done to construct these diagrams.

For this approach, a Schmidt number ($Sc = \nu/D$) of unity was assumed. This is basically the same as assuming that the Lewis and Prandtl numbers are equal to unity. For the analysis, the flame thickness δ_L and the flame time τ_T were defined by respectively Equation 2.38 and Equation 2.39.

$$\delta_L = \frac{D}{S_L} = \frac{\alpha}{S_L} \tag{2.38}$$

$$\tau_T = \frac{D}{S_L^2} \tag{2.39}$$

Then, using the turbulent intensity u' and the characteristic length scale for turbulent eddies l_0, the Reynolds number of the turbulent regime could be defined by Equation 2.40. As explained in Section 2.2, turbulent flows are characterized by high Reynolds numbers.

$$Re_T = \frac{u' l_0}{\nu} = \frac{u' l_0}{S_L \delta_L} \tag{2.40}$$

The turbulent Damköhler number Da is the ratio between the flow timescale and the chemical timescale. The turbulent Damköhler number can be determined using Equation 2.41.

$$Da_T = \frac{\tau_T}{\tau_C} = \frac{l_0 S_L}{\delta_L u'} \tag{2.41}$$

The turbulent Karlovitz number is the ratio between the chemical timescale and the Kolmogrov timescale, as can be seen in

$$Ka_T = \frac{\tau_C}{\tau_\eta} = \left(\frac{\delta_L}{\delta\eta}\right)^2 \tag{2.42}$$

Based on the aforementioned non-dimensional parameters, one could identify different flame regimes as seen in Figure 2.13. This figure's line for $Re_T = 1$ denotes the boundary between a laminar and a turbulent flow. The different turbulent flame regimes are explained below:

- **Wrinkled Flamelets**: $\frac{u'}{S_L} < 1$ and $Ka_T < 1$
  The structure of wrinkled flamelets is similar to that of a laminar flame. However, the turbulent flow weakly wrinkles the flame front.
- **Corrugated Flamelets**: $\frac{u'}{S_L} > 1$ and $Ka_T < 1$
  Again, corrugated flamelets retain a laminar flame structure. But in contrast to the wrinkled flamelets regime, the flow is now more turbulent, which results in more flame wrinkling. This could eventually lead to the folding of the flamelets, which might result in the breaking of the flame front. This causes pockets of burned and unburned mixtures.
- **Thickened Wrinkled Flames**: $Da_T > 1$ and $Ka_T > 1$
  For thickened wrinkled flames, small turbulent eddies are still larger than the reaction zone thickness. However, the eddies are small enough to penetrate the preheat zone of the flame, which increases the heat and mass transfer. For this regime, turbulent mixing plays a significant role, and the flame is not quasi-laminar anymore.

- **Well-Stirred Reactor**: $Da_T < 1$ and $Ka_T > 1$
  In this regime, the smallest turbulent eddies can penetrate the reaction zone, drastically affecting diffusion and chemical reactions. Due to enhanced heat loss to the preheat zone, the temperature will drop in the reaction zone, and this causes the flame to extinguish.

Typical flames in gas turbines have high Reynolds numbers ($Re_T > 10^4$), Damköhler numbers of around one, and Karlovitz numbers larger than ten [43]. This means gas turbine flames are typically in the thickened wrinkled flame regime.

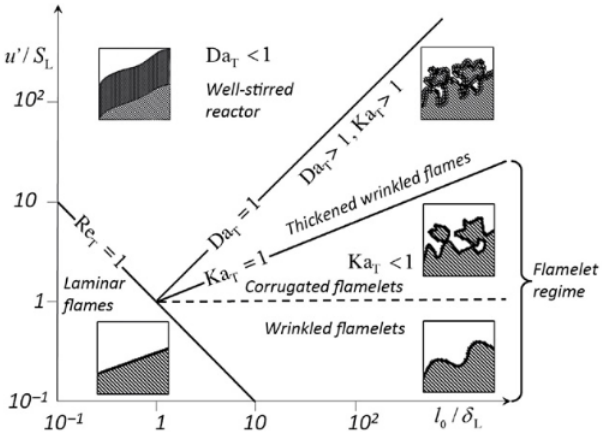

Figure 2.13: Different flame regimes based on non-dimensional parameters [11].

Turbulent Flame Speed

As mentioned earlier in section 2.7, the laminar flame speed depends on the reactants' chemical and thermal properties. However, the flame speed of turbulent flows cannot be easily defined. The turbulent flame speed S_T is not a property existing in physics or chemistry, but it is a function of the turbulence and the geometry of the combustor [35]. It is defined as the average flame propagation rate through the turbulent flow of reactants. It can be seen in Figure 2.13 that each regime will have a different effect on the flame front and, hence, the position of the flame.

In 1940, Damköhler laid a foundation for the theoretical framework of turbulent flame speeds [44]. He equated the mass flow rate $\dot{m}$ that passes the turbulent flame front area A_T with the mass flow rate through the total duct area A as can be seen in Figure 2.14. The laminar flame speed was used for the former mass flow rate, and for the latter mass flow rate, the turbulent flame speed was used. This resulted in Equation 2.43. As the turbulent flow causes flame wrinkling, and thereby an increase in the flame front area, it can be concluded from Equation 2.43 that turbulent flow increases the flame speed.

$$\dot{m} = \rho_u S_L A_T = \rho_u S_T A \tag{2.43}$$

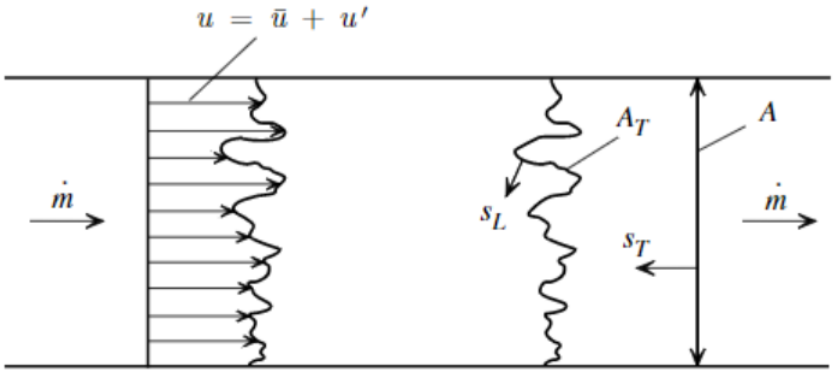

Figure 2.14: An idealized premix flame in a duct as proposed by Damköhler [11].

Adjusting Equation 2.43 leads to Equation 2.44, where Damköhler proposed the approximation of the area ratio.

$$\frac{S_T}{S_L} = \frac{A_T}{A} = 1 + \frac{u'}{S_L} \tag{2.44}$$

Usually, the turbulent intensity is significantly larger than the laminar flame speed. This means that the fuel choice has a minor influence on the turbulent flame speed. Next, Equation 2.44 is often modified into a more general form, shown below as in Equation 2.45.

$$\frac{S_T}{S_L} = A + B(\frac{u'}{S_L})^n \tag{2.45}$$

In the above equation, A, B, and n are empirical parameters determined by experimental work. An example of such an expression for the wrinkled flame regime is determined by Gülder and can be seen in Equation 2.46 [45].

$$\frac{S_T}{S_L} = 1 + 0.6(\frac{u'}{S_L})^{0.5} Re_L^{0.25} \tag{2.46}$$

2.9. NOx formation mechanisms

Nitrogen oxides (NOx) are one of the primary concerning emissions of natural gas-fired gas turbines. NOx denotes both nitric oxide (NO) and nitrogen dioxide (NO_2). In combustion processes, NO is formed and subsequently oxidizes to NO_2. NOx emissions can mainly be produced by four mechanisms: Thermal NO, Nitrous Oxide, Prompt Nitric Oxide, and Fuel Nitric Oxide [32]. However, the latter mechanism is irrelevant, as methane and ethanol do not contain any nitrogen.

- **Thermal NO**
  The thermal NO mechanism was first postulated by Zeldovich [46]. The mechanism consists of the reaction between the present oxygen and nitrogen in the air. This reaction only reaches a significant reaction rate at temperatures exceeding 1850 K. Thermal NO is the main mechanism of NOx formation in conventional gas turbines [32]. However, Thermal NO emissions are reduced by lean premixed combustion due to the lower flame temperatures.

$$O_2 = 2O \tag{2.47a}$$

$$N_2 + O = NO + N \tag{2.47b}$$

$$N + O_2 = NO + O \tag{2.47c}$$

$$N + OH = NO + H \tag{2.47d}$$

- **Nitrous Oxide**
  This mechanism describes the NO formation by reactions of nitrous oxide (N_2O) and is given by Equation 2.48 [47]. This mechanism often occurs in lean conditions [48].

$$N_2 + O + M = N_2O + M \tag{2.48a}$$

$$N_2O + O = 2NO \tag{2.48b}$$

$$N_2O + H = NO + NH \tag{2.48c}$$

- **Prompt NO**
  The mechanism of Prompt NO was first postulated by Fenimore [49]. This mechanism describes the NO formation due to a reaction between hydrocarbon flames and nitrogen in the flame front and is given as in Equation 2.49 [18]. The HCN molecules oxidize to NO by a sequence of reactions, where first CN is produced from HCN, CN oxidizes then into NCO, which dissociates into NO.

$$N_2 + CH = HCN + N \tag{2.49}$$

Usually, Thermal NO would be the only dominant mechanism in combustion. However, the Thermal NO formation mechanism is slightly suppressed for lean conditions, meaning the temperature is relatively low. Next to that, the formation of CH is suppressed, which leads to less Prompt NO. The Nitrous Oxide formation mechanism has a relatively low activation energy, meaning that the low temperatures at lean conditions do not affect the NO formation that much. So, it can be concluded that Thermal NO and Nitrous Oxide NO are the dominant mechanisms in lean conditions [32, 48].

2.10. Gas Turbine Combustor

In a premixed gas turbine combustor, fuel and air will be premixed and passed through swirlers before the mixture is burned in the combustion chamber. A schematic of this can be seen in Figure 2.15. Premixing is often achieved by injecting a fuel jet perpendicular to the airflow.

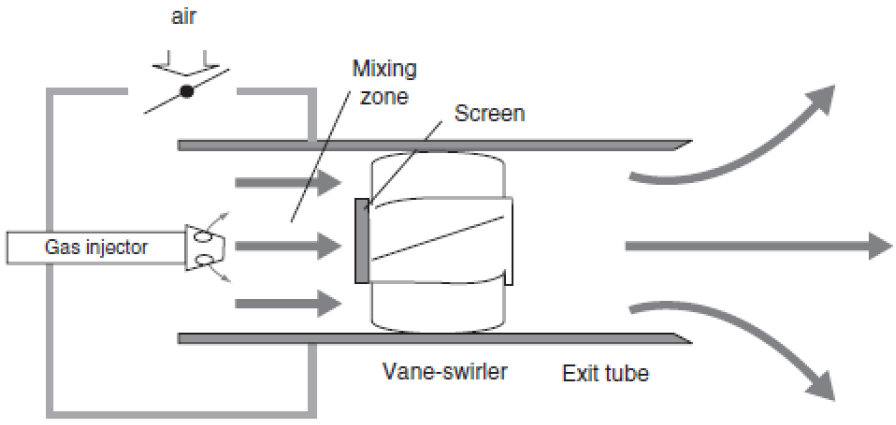

Figure 2.15: Schematic of a premixed and swirl-stabilized burner [13].

Jet in Crossflow

A jet in crossflow (JICF), or transverse jet, refers to a situation where a high-speed jet interacts with a fluid in crossflow. Due to the efficient mixing characteristics in a limited space, JICF is often applied

for gas turbine combustors. The importance of the quality of mixing will be further discussed in Section 2.12.

Four types of coherent structures can be determined in a JICF: shear-layer vortices, horseshoe vortices, wake vortices, and a counter-rotating vortex pair [14]. These can be seen in Figure 2.16. In the far field of the flow, the counter-rotating vortex pair becomes dominant over the other vortical structures. So, downstream of the jet inlet, the counter-rotating vortex pair is synonymous with the jet itself.

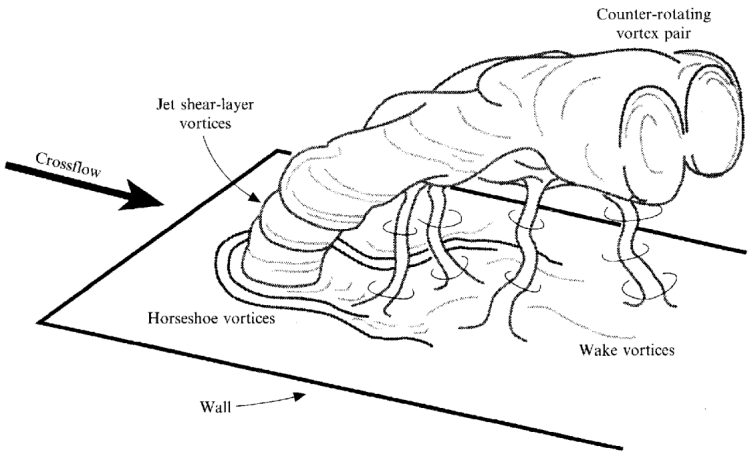

Figure 2.16: Vortical structures in a JICF [14].

An important parameter to characterize a JICF is the momentum flux ratio J, which can be determined by Equation 2.50.

$$J = \frac{\rho_{jet} U_{jet}^2}{\rho_\infty U_\infty^2} \tag{2.50}$$

Where ρ_{jet} and ρ_∞ are, respectively, the densities of the fuel jet and the air crossflow, and U_{jet} and U_∞ are their velocities. Logically, higher values of J indicate that the fuel jet can penetrate further into the air crossflow than for lower values of J.

Flame Stabilization

Flames are positionally stabilized when the local flame speed and flow velocity of reactants are balanced. When there is such a local balance, the flame will be anchored at that position. In a gas turbine, air leaves the compressor at velocities significantly higher than the turbulent flame speed of the fuel-air mixture. To keep the flame at the same position, setting up local regions in the flow with smaller velocities is necessary. This is usually done by creating a local region where the flow is reversed, which can be achieved using different techniques such as a bluff body, opposing fuel jets, pilot flames, and a swirler. In this report, only the use of a swirler will be discussed.

Swirl

The application of swirlers in burners can be seen in Figure 2.17. Close to the walls, External Recirculation Zones (ERZ) are created, and in the center, an Internal Recirculation Zone (IRZ) arises. The IRZ assists in stabilizing the flame, as it brings back the hot combustion products that serve as a heat source for the combustion of the unburned reactants. Next to that, the existence of an IRZ and ERZs causes regions with high-velocity shear layers. This means that if there is a sudden change in the local flame speed, the flame will stabilize close to its original position.

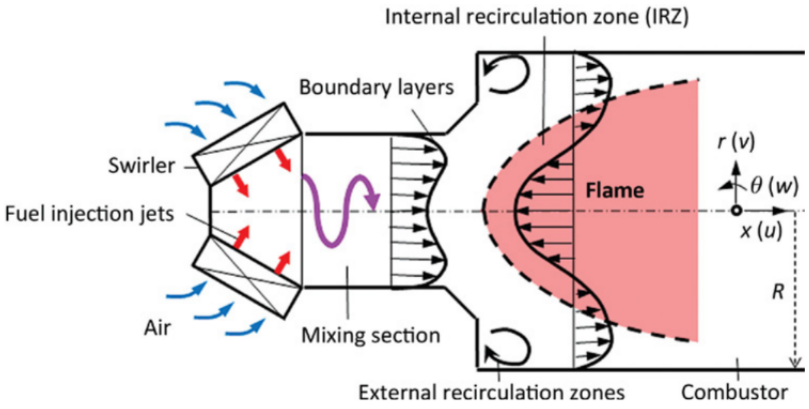

Figure 2.17: Sketch of a premix swirl burner [11].

The incoming axial flow will be deflected When it passes a swirler. This creates a velocity component in the tangential or azimuthal direction, which explains the existence of the recirculation zones. This can be further discussed with the use of the Swirler number S, which is a non-dimensional parameter defining the amount of swirl. The Swirl number is determined by dividing the axial flux of swirl momentum G_θ by the axial flux of axial momentum G_x times the nozzle radius r_n as can be seen in Equation 2.51.

$$S = \frac{G_\theta}{G_x r_n} \tag{2.51}$$

As the flow expands downstream of the swirler, velocities will decay. But for a low degree of swirl, characterized by swirl numbers smaller than 0.4, the adverse pressure gradient is not large enough to cause axial flow recirculation. In contrast, higher degrees of swirl will result in both an axial and radial pressure gradient. This can be seen in Figure 2.18.

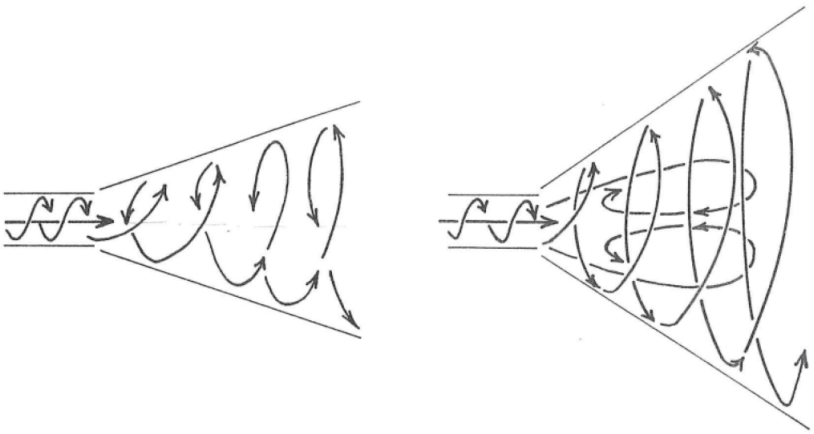

Figure 2.18: Flow patterns for low degrees of swirl (left) and higher degrees of swirl (right) [15].

2.11. Combustion Stability

Stability is a crucial design consideration in gas turbines, and the stability limit defines the operability of a given design for a given inlet condition. Combustion systems have a stability loop for a specific fuel, temperature, and pressure, as seen in Figure 2.19.

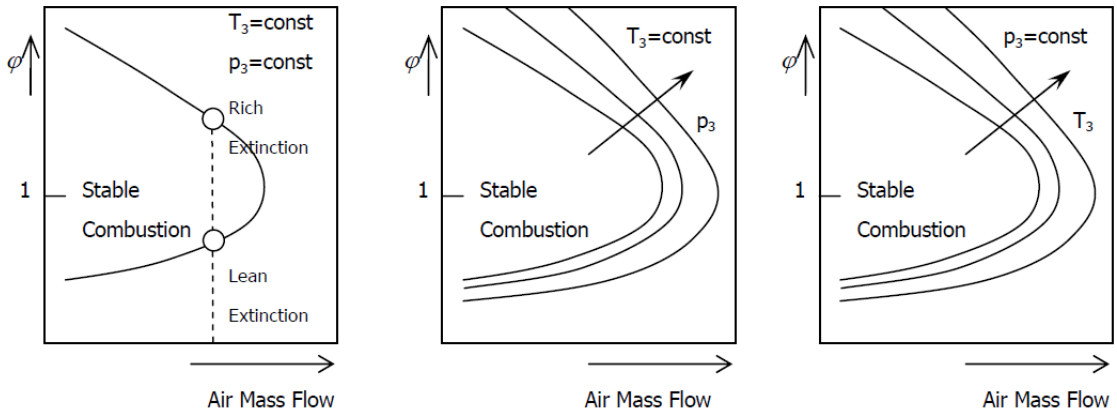

Figure 2.19: Influence of pressure and temperature on the combustor stability loop [16].

Autoignition

Autoignition is when the fuel mixture spontaneously ignites without an external ignition source. A minimum temperature is required for the autoignition of the fuel mixture, which is defined as the autoignition temperature AIT. The onset of autoignition requires some time, called the autoignition delay time τ_{ig}. A longer residence time in the mixing section enhances the mixing quality. But, when the residence time is longer than the autoignition delay time, it could lead to local flashes of the fuel-air mixture. These flashes can result in potential overheating of the burner components.

Blow-off

Blow-off is the phenomenon where the flame detaches from the burner and propagates further downstream in the combustion chamber until the flame is physically blown off. This occurs when the flow velocity of the mixture is larger than the flame speed. Another cause of the blow-off could be a reduction of the fuel-to-air ratio below the lean limit, resulting in the extinction of the flame. When blow-off occurs, the flame is not self-sustained anymore.

Flashback

In contrast to blow-off, flashback occurs when the flow velocity of the mixture is smaller than the flame speed. The flame will then propagate upstream against the mixture's flow direction, which could cause severe damage to the burner and premixer hardware. Possible flashback is one of the major challenges for the design of a premixed combustor. The different flashback-causing mechanisms are defined as [11]:

- **Turbulent flame propagation within core flow**
  Flashback may occur when the turbulent flame speed exceeds the velocity of the core flow. When there is such an imbalance of the turbulent flame speed and the core flow velocity, the flame will propagate upstream, potentially leading to a flashback. However, this flashback type is uncommon in gas turbines, as the flow velocity of unburned reactants is usually significantly larger than the turbulent flame speed [11].

- **Flame propagation within boundary layer**
  Due to the no-slip boundary condition at the combustion wall, the flow velocity is reduced to zero within the boundary level. So, flashback can occur as local flow velocities close to the wall become smaller than the flame velocity. However, heat loss to the wall introduces flame quenching, which counteracts the flashback. Flame quenching only occurs when the distance to the wall is small enough. A study by Hatem showed that higher swirl burners have thinner boundary layers, which makes boundary layer flashback less feasible [50].

- **Combustion instabilities**
  Large amplitude acoustic pressure oscillations driven by unsteady heat release can cause combustion instabilities. The pressure and heat release oscillations should have a phase difference

smaller than 90°for the combustion instabilities to occur. These combustion instabilities, which will be further described in Figure 2.11, introduce velocity fluctuations. The velocity fluctuations may trigger flashback.

- **Combustion induced vortex breakdown**
  Swirling motion is often applied in combustion chambers for flame stabilization. The flame is typically anchored upstream of the internal recirculation zone created by the swirling motion, as is explained in Equation 2.10. This internal recirculation zone introduces negative axial velocities in the core flow, which triggers so-called vortex breakdown [51]. The negative axial velocity in the core flow could result in a possible flashback. So, this type of flashback is typical for swirl burners.

Dynamic Instabilities

Combustion instabilities (known as dynamics/oscillations) are undesirable as they can lead to catastrophic damage to the gas turbine hardware. However, this phenomenon is very complex, so it is still an active area of research in combustion science. The combustion instabilities are caused by a feedback loop, which can be seen in Figure 2.20. Fluctuations in the heat release add energy to the acoustic field. This leads to pressure and velocity fluctuations, leading to flow and mixture perturbations. These will cause heat release fluctuations, so the feedback loop is closed. The oscillatory combustion process adds energy to the acoustic oscillations when their phase difference is smaller than 90°. This is demonstrated by Rayleigh's criterion [52]:

$$\int_V \int_t p'(x,t) q'(x,t) dt dV > 0 \tag{2.52}$$

Where $p'(x,t)$ and $q'(x,t)$ are, respectively, the combustor pressure oscillations and the heat release oscillations. Different mechanisms can cause oscillations, activating the aforementioned feedback loop. The most important mechanisms for premixed combustion are [17]:

- **Equivalence Ratio Oscillations**
  Pressure oscillations caused by the combustion process may propagate into the premixer. The pressure oscillations will affect the mixture's air and fuel supply, resulting in a mixture with a periodically varying equivalence ratio. This will, in turn, result in oscillatory heat release.
- **Oscillatory Flame Area**
  The oscillatory flame can be caused by interaction with acoustic velocity oscillations or due to the present vortices in the flow. This varying flame area will cause variations in the heat release of the flame and could have a driving effect on combustion instabilities.

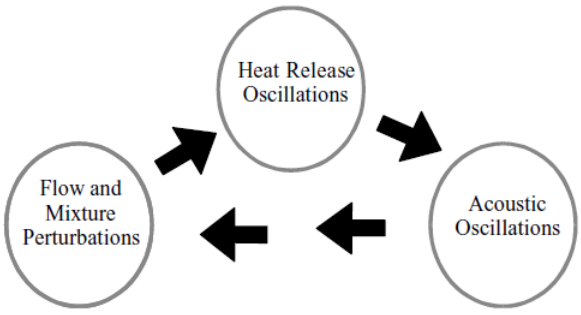

Figure 2.20: Feedback loop causing combustion instabilities [17].

Energy can also be removed from unstable acoustic modes by one of the following damping mechanisms:

- **Viscous and Heat Transfer Damping**
  The acoustic mode may lose energy due to boundary layers or flow separation. For boundary layer losses, the no-slip boundary condition and the zero-amplitude temperature oscillations

cause energy from the acoustic wave to be transferred in vortical velocity or entropy fluctuations, respectively. So, due to these fluctuations, the acoustic wave will have less energy when reflected from a wall. Flow separation losses occur at sharp edges or rapid flow expansions, and this will convert the energy of the acoustic waves into vorticity.

- **Radiation and Convection**
  In this mechanism, acoustic energy may leave the system due to propagation or convection caused by the fluid motion out of the system.

- **Transfer of Energy**
  The acoustic oscillations will occur at one or more of the natural frequencies of the combustion chamber. However, acoustic energy may also be transferred from these natural frequencies to other modes that oscillate at frequencies that are not amplified. This phenomenon is caused by random modulation processes, such as the reflection and scattering of sound waves due to turbulent eddies. The transfer of acoustic energy has a damping effect for the specific mode.

When the driving mechanisms are more significant than the damping mechanisms, the amplitudes of the acoustic oscillations will increase. The feedback loop will then cause a situation where the amplitude is increased even further. Active or passive measures could be taken to counteract the driving mechanisms. Active measures focus on reducing the amplitudes of the combustor pressure and heat release oscillations or ensuring that both oscillations are out of phase. Passive measures ensure that the damping mechanisms are larger than the driving mechanisms. This can be done, for example, by Helmholtz resonators or combustion tuning [17].

2.12. Gas Turbine Emissions

The exhaust gases from the combustion process in a gas turbine contain several pollutants. The pollutants that will be discussed are NOx, Carbon Monoxide (CO), and Unburned Hydrocarbons (UHC). Parameters, such as the temperature, time, and power load, influence the concentration of these pollutants in the exhaust gases. The effect of temperature on the formation of CO and NOx can be seen in Figure 2.21. As the equivalence ratio controls the temperature, Figure 2.21 can be modified into a figure similar to Figure 2.22. However, it is essential to note that Figure 2.22 uses an air/fuel equivalence ratio, where the fuel/air equivalence ratio was considered in this report.

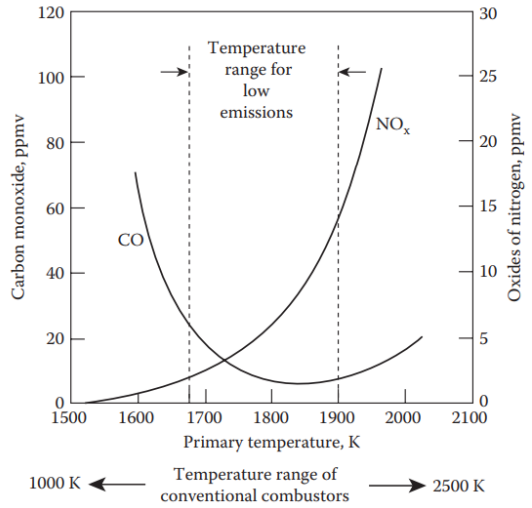

Figure 2.21: Influence of the temperature on the NOx and CO formation [18].

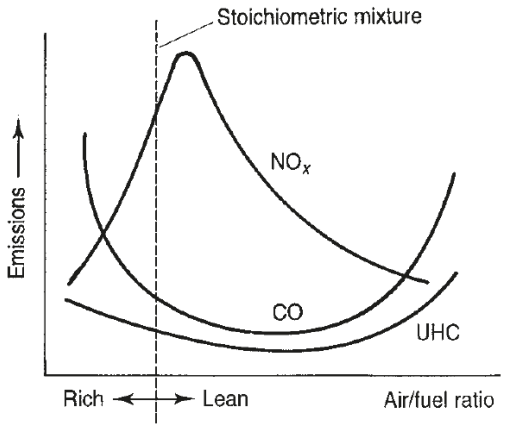

Figure 2.22: NOx, CO, and UHC emissions versus the equivalence ratio [19].

NOx

The following events mainly cause higher NOx levels:

- **Quality of Mixing**
  The quality of mixing has a significant impact on the NOx emissions from a gas turbine. In poorly mixed mixtures, there will be fuel-rich and fuel-poor pockets. As NOx emissions have an almost exponential relation with the temperature, a higher local equivalence ratio in fuel-rich pockets will cause an overall increase in NOx emissions when compared to perfectly mixed mixtures [53].
- **Residence Time**
  Another factor impacting NOx emissions is the residence time in the combustion chamber. As NOx formation mechanisms consist of slow reactions, an increase in residence time at high temperatures will lead to more NOx emissions. Next, it was found that NOx emissions are increased by an increase in pressure [53].

Carbon Monoxide and Unburned Hydrocarbons

Typical reasons for higher CO emissions are:

- **Excess Fuel**
  When the combustion zone has excess fuel, it generates high levels of carbon monoxide (CO) because there is not enough oxygen available to complete the combustion reaction and produce carbon dioxide (CO_2).
- **Residence Time**
  Also, in lean conditions, significant amounts of CO may be formed because the oxidation reaction of CO into CO_2 is relatively slow. This means that when the residence time is too short, an increase in CO emissions could be experienced.
- **Overcooling**
  Overcooling could result in quenching of the oxidation reaction of CO, thereby leading to higher CO emissions.

As for CO emissions, unburned hydrocarbon (UHC) emissions are caused by incomplete combustion. So, UHC emissions will typically follow the trends of CO emissions.

2.13. Mixing Quality

As mentioned in section 2.12, the mixing quality significantly impacts the NOx (and, to a lesser extent, CO) emissions. A lower quality of mixing will lead to a higher NOx emission level. The quality of mixing can be evaluated using different parameters, but for this research, the unmixedness described by Hornsby and Norster will be used [54]. They characterize the mixing in a combustion system using the mass flow weighted standard deviation of the fuel distribution (denoted as S) at a specified plane. The mass flow weighted standard deviation of the fuel distribution S can be calculated by Equation 2.53.

$$S = \sqrt{\frac{\sum \left(C_i^2 M_i\right)}{\sum M_i} - \left(\frac{\sum C_i M_i)}{\sum M_i}\right)^2} \tag{2.53}$$

Where C_i is the mass fraction of the fuel at cell i, M_i is the massflow through cell i, and A_i is the area of cell i. Now Equation 2.53 can be normalized with the use of Equation 2.54.

$$S_N = \frac{S}{S_0} \tag{2.54}$$

Where S_0 is a value for the situation where the fuel and air are unmixed. S_0 can be calculated with the use of Equation 2.55.

$$S_0 = \sqrt{\left(\frac{1}{F+1}\right) - \left(\frac{1}{F+1}\right)^2} \tag{2.55}$$

In this equation, F is the mass-based air-to-fuel ratio. To conclude, a S_N of 0 indicates the unmixed situation, and a S_N of 1 indicates that the fuel and air are perfectly mixed.

3

Methodology

This chapter will serve as the link between the research questions, theoretical background, and the research itself. The research goal is to get an overview of how the use of ethanol will affect the process design and the combustion characteristics of Killingholme. Section 3.1 will discuss how the effect on the process design will be studied, and the workflow for the research of the combustion characteristics will be addressed in Section 3.2.

3.1. Process Design

First, burner inlet conditions were measured during a baseload performance test performed by Uniper. This baseload performance test was performed during actual operation, so natural gas was used as the fuel. As discussed in Chapter 1, the research focuses on comparing ethanol and methane, which means that different mass flows are required to have the same energy output from the gas turbine. The burner inlet conditions will also be used to determine the required minimum temperature of ethanol to be in vapor form. Then, the MWI (discussed in Section 2.4) of ethanol and methane will be calculated and compared. With the use of additional literature research, the feasibility of ethanol using existing fuel storage and supply systems will be assessed. The possibilities for heat integration will also be studied, where the heat integration should provide the required heat for the ethanol evaporation. A preliminary baseload design will be modeled with the use of Aspen Hysys. Finally, the workflow can be summarized in Figure 3.1.

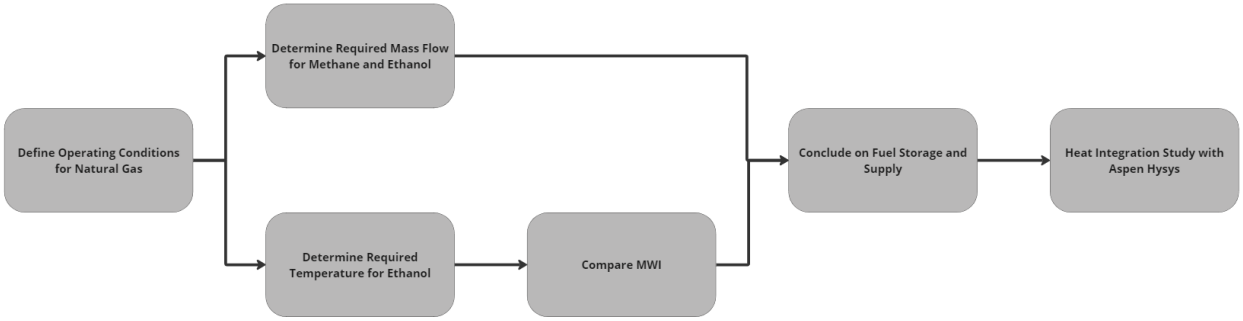

Figure 3.1: Workflow for the process design of ethanol.

3.2. Combustion Characteristics

The combustion characteristics will be evaluated based on a few criteria: flame length/position, autoignition, flashback/blowoff, NOx emissions, and combustion dynamics. The effect of ethanol with respect to these criteria can be determined with the use of different relevant parameters, such as the adiabatic flame temperature, laminar flame speed, effective Lewis number, autoignition delay time,

and the fuel-air mixing quality. To determine the effect of ethanol on the combustion characteristics, a comparison of the aforementioned parameters will be performed for ethanol and methane. Table 3.1 describes which parameters will be used to evaluate each criterion.

Table 3.1: Summary of the parameters that will be used to evaluate the criteria for the combustion characteristics.

Criterion	**Relevant Parameters**
Autoignition	Autoignition Delay Time
Flame Length/Position	Laminar Flame Speed - Effective Lewis Number - Fuel-Air Mixing Quality
Flashback/Blowoff	Laminar Flame Speed - Effective Lewis Number - Flame Length
NOx Emissions	Adiabatic Flame Temperature - Fuel-Air Mixing Quality - Flame Length
Combustion Dynamics	Fuel-Air Mixing Quality - Flame Length

The adiabatic flame temperature, laminar flame speed, effective Lewis number, and the autoignition delay time will be determined for ethanol and methane at relevant conditions with the use of a kinetic modeling study. The fuel-air mixing quality for ethanol and methane will be compared using a computational fluid dynamics (CFD) model of the premixing section of the HR3 burner.

Kinetic Modeling Study

Several combustion parameters for ethanol and methane will be compared to evaluate the effect of implementing ethanol as a fuel for the gas turbine. These combustion parameters will be determined using a chemical kinetics simulation performed with the Cantera package in Python [55]. In a chemical kinetics simulation, the rate of chemical reactions will be studied, which was already briefly mentioned in Section 2.5. First, a suitable kinetic mechanism should be selected for the chemical kinetics simulation. As most kinetic mechanisms are provided in the CTI format, and Cantera requires files in the YAML format, the kinetic mechanism should be converted. This can be done with the use of the cti2yaml script that can be downloaded from the Cantera website [55]. Then, the kinetic mechanism will be validated for conditions relevant to the Siemens SGT5-2000E gas turbine.

When the validation is successful, the kinetic mechanism can be used for a FreeFlame and an IdealGasReactor simulation. The FreeFlame function in Cantera simulates a one-dimensional, freely-propagating, and premixed flame. The laminar flame speed and the adiabatic temperature can be directly determined from this simulation. The effective Lewis number will be determined following the equations described in Section 2.7.

The autoignition delay time will be determined using the IdealGasReactor function of Cantera. This function models a specified mixture in a constant-volume batch reactor. The time before the mixture ignites without the addition of an ignition source, i.e., the autoignition delay time, will be determined by monitoring the OH concentration in the mixture. A sudden increase of OH indicates that autoignition has taken place.

The methodology for the kinetic modeling study can be summarized in Figure 3.2.

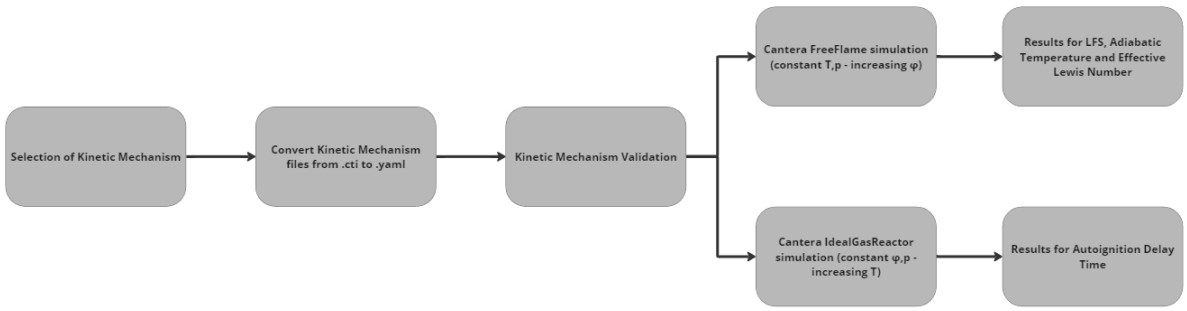

Figure 3.2: Workflow for the kinetic modeling study.

Fuel Air Mixing Study

Figure 3.3 shows the workflow for the CFD analysis of the fuel-air mixing. The Ansys Fluent software was used for the CFD analysis [27]. First of all, the selected turbulence models should be validated. The validation will be performed using a reference case that provides experimental data. Based on the performance of the turbulence models in the reference case, a turbulence model will be selected for the remaining CFD analysis.

After the turbulence model selection, the geometry of the mixing section of the HR3 burner will be defined, and a model will be made using the DesignModeler package of Ansys Fluent. Then, a mesh will be designed based on the geometry. The mesh will be verified by a mesh independence study, and different quality measures will also be checked. If the mesh provides acceptable solutions, the quality of the fuel-air mixing can be studied by performing steady RANS simulations. These simulations provide the results that were used to compare ethanol with methane.

Figure 3.3: Workflow for the fuel-air mixing study.

4

Process Design

In this chapter, the current conditions of the Killingholme power plant will be discussed first in Section 4.1. These conditions will be used to determine the required conditions for the ethanol case. Then, a preliminary design for the ethanol case during baseload operation will be given in Section 4.2. And finally, Section 4.3 discusses some important aspects that should be considered before ethanol can be implemented.

4.1. Operating Data

Uniper provided some burner inlet conditions that were established in a baseload performance test. These parameters can be found in Table 4.1. This baseload performance test is based on the use of natural gas as a fuel. However, for the remaining research, ethanol will be compared to methane instead of natural gas. This simplification is deemed acceptable, as natural gas used in the United Kingdom consists for 92% out of methane [56].

Table 4.1: Parameters obtained from a performance test of a single gas turbine at the Killingholme site provided by Uniper.

Parameter	**Value**	**Unit**
Compressor Discharge Pressure	11.2	bar
Compressor Discharge Temperature	608	K
Fuel Gas Temperature	294	K
Maximum Fuel Pressure	18	bar
LHV_{fuel} (Natural Gas)	47.1	MJ/kg
Fuel Net Mass Flow ($\dot{m}_{fuel}$)	9.2	kg/s
MW_{th} Input	433	MW
Compressor Outlet Mass Flow	512.9	kg/s
Turbine Inlet Temperature	1296	K

As can be seen in Table 4.1, the maximum fuel pressure was measured to be 18 bar. The required temperature for ethanol evaporation can be determined by equating the maximum fuel pressure to the vapor pressure. The Antoine equation relates the vapor pressure to the temperature and is given in Equation 4.1 [24].

$$log_{10}(p) = A - (B/(T + C)) \tag{4.1}$$

Where T is the temperature in Kelvin, and A, B, and C are empirically determined parameters. A, B, and C are respectively 4.92531, 1432.526, and -61.819 for ethanol [57]. This leads to a minimum

required temperature of 452 K (179 $^{\circ}C$) for a pressure of 18 bar. However, Siemens advised having a fuel temperature that is 15 K above its boiling point to avoid condensation of the fuel, so the required fuel temperature of ethanol was determined to be 467 K (194 $^{\circ}C$) [58]. For methane, a typical temperature of 293.15 K (20 $^{\circ}C$) was assumed. This indicates that there is no efficiency preheating.

Methane has an LHV of 50 MJ/kg and ethanol of 26.7 MJ/kg [59]. Methane and ethanol will be compared to natural gas with the use of the WI and MWI, where the former is calculated by Equation 2.22 and the latter is calculated by Equation 2.23. The MWI is the same as WI with an added temperature factor. For both calculations, the reference temperature was taken to be 273 K (0 $^{\circ}C$). The results are summarized in Table 4.2.

Table 4.2: Comparison between the WI and MWI of methane and ethanol.

Parameter	**Natural Gas**	**Methane**	**Ethanol**	**Unit**
Fuel Temperature	293	293	467	K
LHV	47.1	50	26.7	MJ/kg
WI	46.4	48.1	43.5	MJ/m^3
MWI	43.1	46.4	33.3	MJ/m^3

Siemens stated that their SGT5-2000E gas turbines can run without problems on fuels varying within five percent of the WI that is specified on-site during commissioning. It is also stated that this variation range of five percent can also be extended by minor adjustments [58]. The WI of ethanol is slightly out of the aforementioned variation range (-6.3 %) for natural gas, but this is deemed acceptable. The lower WI of ethanol suggests an increased pressure drop, leading to an increase in the required maximum fuel pressure. Another option would be to change the valve settings to ensure the same fuel pressure. However, for the remaining part of this research, the maximum fuel pressure was still considered to be 18 bar.

The kinetic modeling and fuel-air mixing study will be based on Table 4.1. It is essential to discuss some assumptions before these parameters can be modified for the methane and ethanol case. Firstly, it is assumed by Uniper that 90% of the Fuel Net Mass Flow will be used for the premixed combustion, and the remaining 10% will be used as pilot fuel. Secondly, it is assumed that the premix flame reaches a temperature of 1773 K (1500 $^{\circ}C$), which is in agreement with literature from Siemens [4]. From these assumptions, the amount of air flowing out of the compressor that will be mixed with the fuel ($\dot{m}_{main}$) can be determined with the use of an energy balance. From Equation 4.2, it was determined that the amount of air used for combustion was 284.8 kg/s. This means that around 56% of the compressor outlet mass flow will be mixed with fuel for combustion, and the remaining part will be used for cooling. This value will be evaluated later on in this chapter.

$$\dot{m}_{main} = \frac{Q}{C_{p,2}T_2 - C_{p,1}T_1} \tag{4.2}$$

Where $C_{p,2}$ denotes the isobaric specific heat at the premix flame temperature of 1773 (T_2), and $C_{p,1}$ denotes the isobaric specific heat at the compressor discharge temperature (T_1). Q is the energy that is generated by combusting the fuel that was reserved for premix combustion. It is also important to note that for the remaining part of this paper, it will be assumed that air consists for 79% out of nitrogen and 21% out of oxygen. The mass flows of methane and ethanol are determined on an LHV basis to ensure the same energy output and are given to be 7.8 and 14.6 kg/s, respectively, for the premixed combustion. The mass flows are summarized in Table 4.3.

Table 4.3: Mass flows for air, methane, and ethanol.

Substance	Name	Mass Flows
Air	Combustion	284.8 kg/s
	Cooling	228.1 kg/s
Methane	Premix	7.8 kg/s
	Pilot	0.9 kg/s
Ethanol	Premix	14.6 kg/s
	Pilot	1.6 kg/s

4.2. Preliminary Baseload Design for Ethanol

The data that was presented in Table 4.1, Table 4.2 and Table 4.3 will be used to make a preliminary process design for baseload operation with ethanol as the fuel. Aspen Hysys was used for the process design and this resulted in Figure 4.1, where the main goal was to get an overview of how much heat was required to evaporate the ethanol. The gas turbine is modeled as a separate compressor, combustor, and turbine unit. The inlet and outlet conditions of the compressor are constrained by the values given in Table 4.1. As can be seen, only a part of the air from the compressor flows to the combustor, where it will be mixed with the evaporated ethanol before the mixture gets ignited. The mass flow rates from Table 4.3 were used, which resulted in the combustion exhaust gas having a temperature of 1776 K. As this value is almost equal to the assumed premix flame temperature of 1773 K, it was concluded that the calculation of the air mass flow rates was reasonably accurate. The combustion exhaust gas mixes with the cooling air before it flows into the turbine. For the turbine, the outlet temperature was assumed from literature to be 808 K (535 $^{\circ}C$) [60].

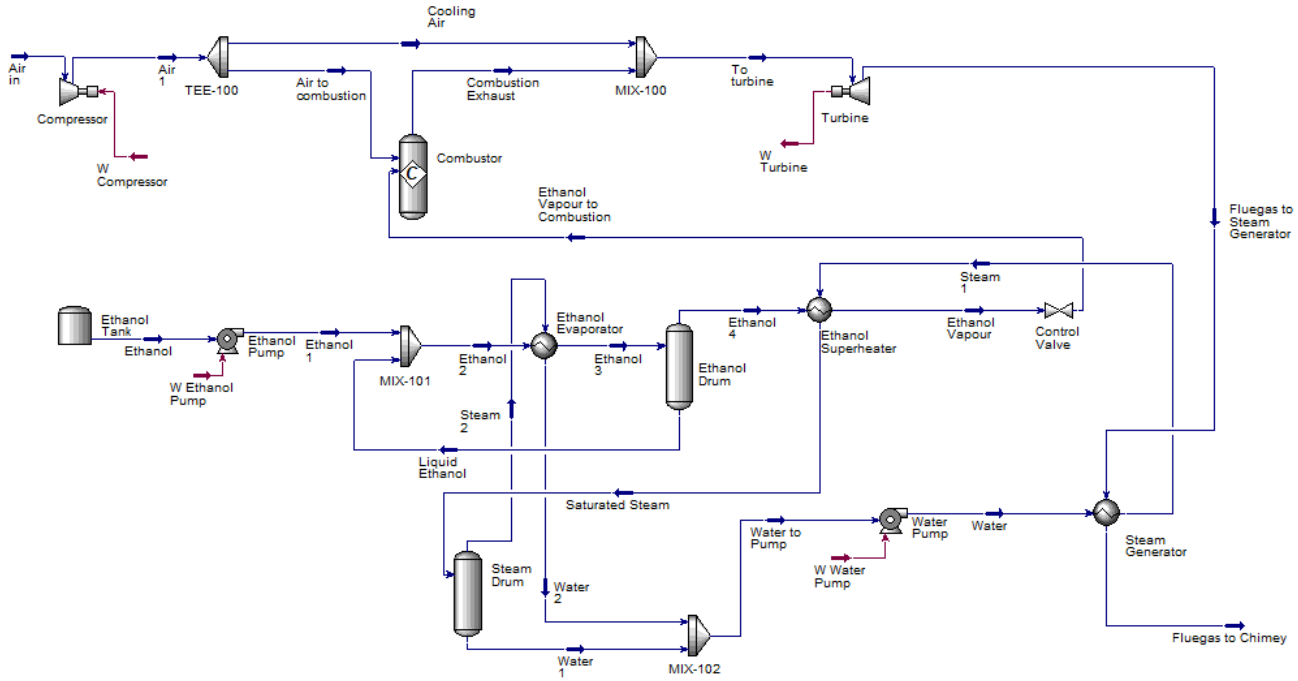

Figure 4.1: Schematic of the preliminary process design for baseload operation.

It can be seen that ethanol is stored in a tank. Ethanol will be pumped out of the tank before it

is evaporated, and later on, it is superheated. The ethanol evaporator and superheater use steam as the working fluid because it is safe and easy to control. The steam first passes through the ethanol superheater, where part of the steam condenses, and this will be fed into the steam drum, where water and steam will be split. The remaining steam is then fed into the ethanol evaporator. The steam generator, ethanol evaporator, and ethanol superheater are modeled as shell and tube heat exchangers. From Table 4.2 and Table 4.3, it was given that liquid ethanol with a mass flow of 16.2 kg/s should be evaporated and superheated to a temperature of 467 K. The flow parameters of the working fluids in the steam generator, ethanol evaporator, and ethanol superheater are summarized in Table 4.4.

Table 4.4: Flow parameters for the steam generator, ethanol evaporator, and ethanol superheater.

Name	**Parameter**	**Value**	**Parameter**	**Value**
Steam Generator	Q	19.6 MW		
	$\dot{m}_{fluegas}$	529.1 kg/s	$\dot{m}_{steam}$	9.4 kg/s
	$T_{fluegas,in}$	818.2 K	$T_{steam,in}$	422.8 K
	$T_{fluegas,out}$	786.2 K	$T_{steam,out}$	495.0 K
	$p_{fluegas,in}$	1.1 bar	$p_{steam,in}$	25 bar
Ethanol Superheater	Q	0.7 MW		
	$\dot{m}_{ethanol}$	16.2 kg/s	$\dot{m}_{steam}$	9.4 kg/s
	$T_{ethanol,in}$	449.6 K	$T_{steam,in}$	495.0 K
	$T_{ethanol,out}$	467.2 K	$T_{steam,out}$	492.8 K
	$p_{ethanol,in}$	18 bar	$p_{steam,in}$	24 bar
Ethanol Evaporator	Q	18.9 MW		
	$\dot{m}_{ethanol}$	16.2 kg/s	$\dot{m}_{steam}$	9.1 kg/s
	$T_{ethanol,in}$	293.2 K	$T_{steam,in}$	492.8 K
	$T_{ethanol,out}$	449.6 K	$T_{water,out}$	455.3 K
	$p_{ethanol,in}$	18 bar	$p_{steam,in}$	23 bar

Figure 4.2, Figure 4.3 and Figure 4.4 show the T-Q diagrams for the three heat exchangers. Note that the process design can potentially be further improved. However, the process design is not the main focus of this research, so any process improvements are left for further research.

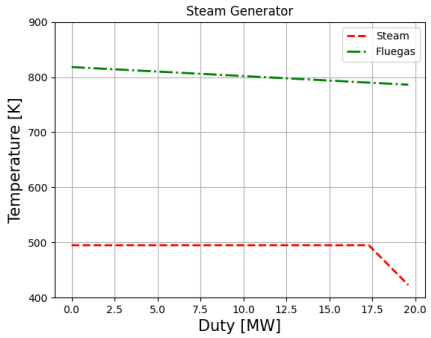

Figure 4.2: T-Q diagram for the Steam Generator.

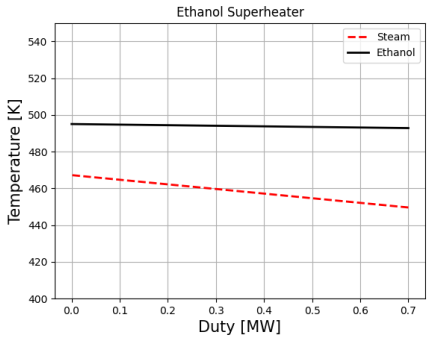

Figure 4.3: T-Q diagram for the Ethanol Superheater.

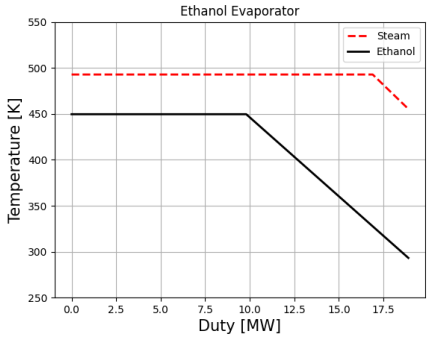

Figure 4.4: T-Q diagram for the Ethanol Evaporator.

4.3. Implementation of Ethanol

As touched upon earlier in this chapter, the mass-based heating value is lower for ethanol when compared to methane, and this leads to higher required volume flow rates to deliver the same energy output. However, the volumetric heating value of ethanol is only 4% lower than that of methane; ethanol has a volumetric heating value of 354.0 MJ/m^3 (T = 467 K and p = 11 bar), and methane has a volumetric heating value of 367.7 MJ/m^3 (T = 293 K and p = 11 bar). This means that only slightly higher volume flow rates are required for ethanol, and therefore, further research should determine whether larger pipes and fittings are required to keep the fuel pressure within the desired limits.

Next to that, ethanol's characteristics may be changed due to contaminants. These contaminants may influence the combustion process and could potentially lead to material degradation of the gas turbine. Ethanol is highly hygroscopic, and oxygen and carbon dioxide are very soluble in ethanol [61]. Water, oxygen, and carbon dioxide may react into different contaminants such as carbonic acid. With this in mind, it is important to store ethanol in a tank where it is not in contact with moisture or air. To prevent this, purging the storage tank would be a good option as this removes unwanted substances from the tank. Another measure could be nitrogen blanketing within the storage tank, which prevents the ethanol from being in contact with air [61].

Another important aspect is the materials that are used in the fuel system. The use of ethanol leads to an increased risk of corrosion of the used metals [62]. Possible metals that can be used for ethanol pipelines are stainless steel and carbon steel, where the use of corrosion inhibitors or coatings could help prevent corrosion [63]. Other suitable materials could be non-metals or ceramics.

It can be concluded from this section that minor adjustments to the fuel system are required for ethanol. However, these adjustments are not within the scope of this paper and are left for further research.

5

Kinetic Modeling Study

As mentioned in Chapter 3, a kinetic modeling study was performed to study the effect of ethanol on the combustion characteristics. For this kinetic modeling study, a kinetic mechanism will be selected in Section 5.1. Then, the kinetic mechanism will be validated for ethanol and methane in Section 5.2, before the results of the kinetic modeling study will be presented in Section 5.3.

5.1. Kinetic Mechanism Selection

As mentioned in Section 3.2, a kinetic mechanism will be selected, which will be used to determine some parameters that characterize the combustion of ethanol and methane. Table 5.1 provides an overview of existing kinetic mechanisms designed to simulate ethanol's oxidation reaction. It could be observed that some kinetic mechanisms are more detailed than others, as the number of species and reactions vary between different mechanisms. To select a suitable kinetic mechanism, one should check whether the mechanism is validated for the preferred conditions, such as the pressure, temperature, and equivalence ratio. Table 5.1 also provides information about the validated conditions of the kinetic mechanisms.

Table 5.1: Kinetic Mechanisms suitable for ethanol oxidation.

Reference	**# of Species**	**# of Reactions**	**Pressure [bar]**	**Temperature [K]**	**ϕ [-]**
Dunphy [64]	30	97	1.8-4.6	298-1660	0.25-2.0
Marinov [65]	56	351	1.0-4.5	>1000	0.2-2.0
Saxena [66]	57	288	1.0-4.6	298-1700	0.5-2.0
Cancino [67]	136	1136	0.9-50	700-1600	0.25-2.0
Ranzi [68]	159	2459	1-10	298-1250	0.5-1.5
Metcalfe [69]	124	766	0.65-260	300-2500	0.05-5.0
Olm [70]	49	251	0.2-91.2	750-2400	0.3-2.0
Zyada [71]	107	1795	1-30	298-1400	0.5-2.0
Roy [72]	67	1016	1-50	300-1450	0.3-2.0
Marques [73]	43	188	10-50	770-1430	0.5-1.0
	44	205			

The only kinetic mechanism that can be used for both the combustion of ethanol and methane is the CRECK mechanism designed by Ranzi et al. from a research group of the Politecnico di Milano [68, 74]. Hence, the CRECK mechanism will be considered for the kinetic modeling study. However, it should be

noted that the CRECK mechanism was not validated for both ethanol and methane at the typical gas turbine conditions, so it was decided that the kinetic mechanism should be further validated.

5.2. Kinetic Mechanism Validation

As mentioned in Section 5.1, the CRECK mechanism should be validated for methane and ethanol. The performance for the laminar flame speed and autoignition delay time will be checked by experimental data that is collected from literature.

Ethanol

Figure 5.1 shows the results from the CRECK mechanism and experimental work at different temperatures and pressures. From Figure 5.1a, Figure 5.1b, Figure 5.1c and Figure 5.1d, it can be deduced that the CRECK mechanism can give a good representation of the laminar flame speed at atmospheric pressure and relatively low temperatures (T<453 K). However, when the temperature is increased to a value of 600 K, it can be seen that the CRECK mechanism slightly overestimates the laminar flame speed. When you compare Figure 5.1a and Figure 5.1d, it can be noticed that the laminar flame speed increases with increasing temperature.

Figure 5.1e and Figure 5.1f show the performance of CRECK mechanisms at an elevated pressure of 10 bar. This pressure is relatively close to the compressor discharge pressure of the Siemens SGT5-2000E gas turbine. It can be concluded that the CRECK mechanism is able to represent the laminar flame speed at higher pressures relatively well. Next to that, from the comparison between Figure 5.1b and Figure 5.1e, it can be deduced that an increasing pressure has a damping effect on the laminar flame speed.

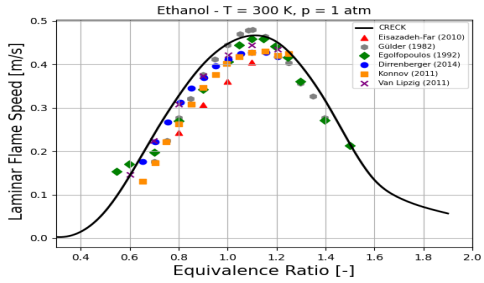

(a) CRECK mechanism versus experimental work at T = 300 K, p = 1 atm [75–80].

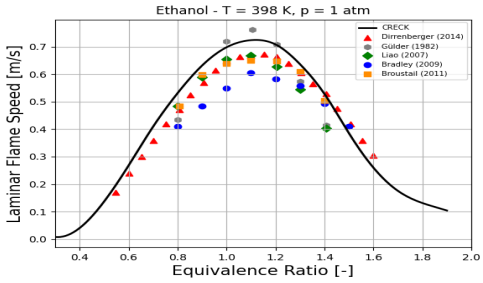

(b) CRECK mechanism versus experimental work at T = 398 K, p = 1 atm [76, 78, 81–83].

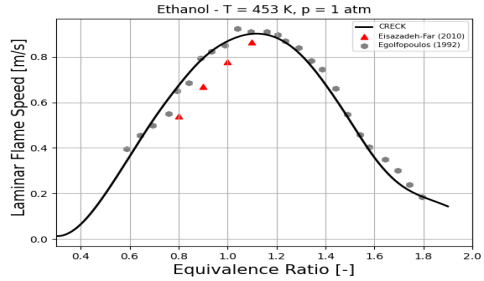

(c) CRECK mechanism versus experimental work at T = 453 K, p = 1 atm [75, 77].

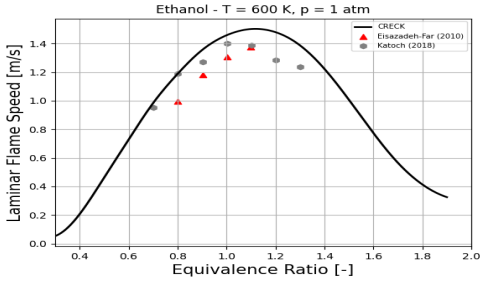

(d) CRECK mechanism versus experimental work at T = 600 K, p = 1 atm [75, 84].

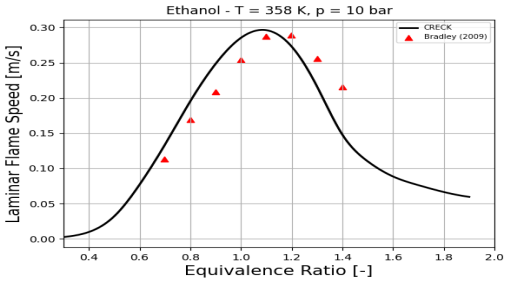

(e) CRECK mechanism versus experimental work at T = 358 K, p = 10 bar [82].

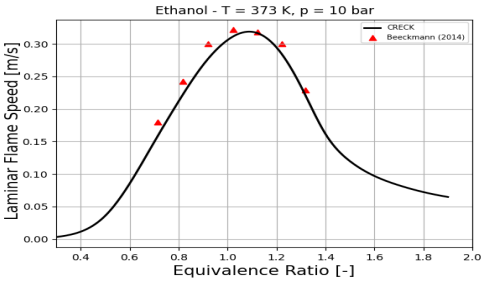

(f) CRECK mechanism versus experimental work at T = 373 K, p = 10 bar [85].

Figure 5.1: Validation of laminar flame speed of ethanol calculated at different temperatures using the CRECK mechanism (represented by the black lines) for different temperatures and pressures.

Figure 5.2 shows the performance of the CRECK mechanism for the autoignition delay time for different equivalence ratios and pressures. When looking at Figure 5.2a and Figure 5.2b, it can be seen that an increase in the equivalence ratio leads to a decrease in the autoignition delay time. The same effect on the autoignition delay time can be recognized for an increase in pressure, as can be seen in Figure 5.2c and Figure 5.2f. However, the pressure and equivalence ratio effects are deduced to be relatively small compared to the temperature effects.

In general, the CRECK mechanism can accurately represent the autoignition delay time for ethanol for different equivalence ratios, pressures, and temperature regions. Only in Figure 5.2d, it can be seen that there is a significant deviation between the CRECK mechanism and data from Laich (2019) for the region where the temperature is larger than 1250 K. The significant differences can be explained as the experiments are performed at a lower pressure of 19.57 atm [86]. Next to that, as the CRECK mechanism produces similar results to the other experiments presented in Figure 5.2d, it was concluded that the difference is acceptable.

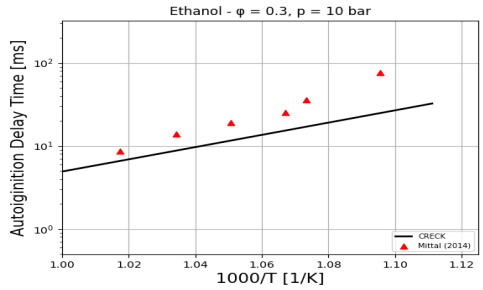

(a) CRECK mechanism versus experimental work at ϕ = 0.3, p = 10 bar [87].

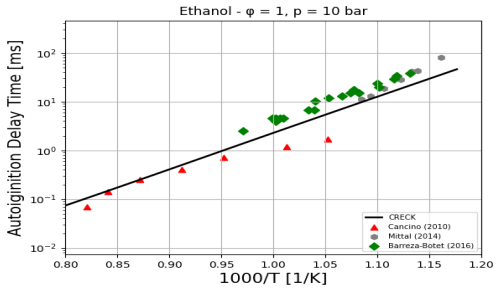

(b) CRECK mechanism versus experimental work at ϕ = 1, p = 10 bar [67, 87, 88].

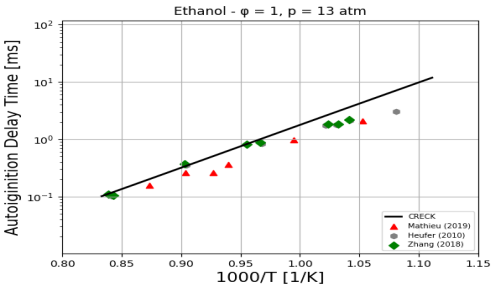

(c) CRECK mechanism versus experimental work at ϕ = 1, p = 13 atm [89–91].

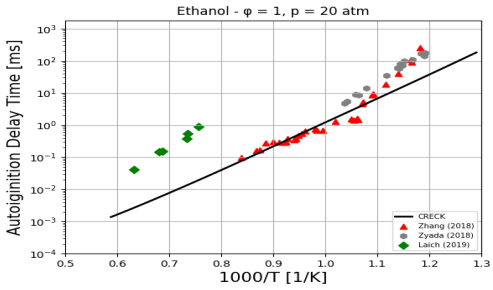

(d) CRECK mechanism versus experimental work at ϕ = 1, p = 20 atm [71, 86, 91].

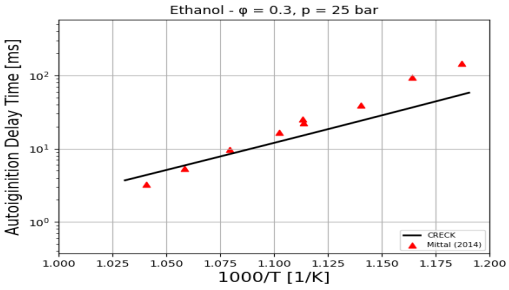

(e) CRECK mechanism versus experimental work at ϕ = 0.3, p = 25 bar [87].

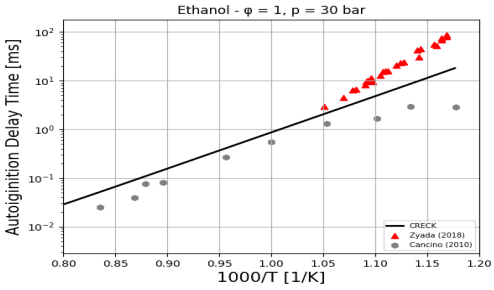

(f) CRECK mechanism versus experimental work at ϕ = 1, p = 30 bar [67, 71].

Figure 5.2: Validation of autoignition delay time of ethanol calculated using the CRECK mechanism (represented by the black lines) for different equivalence ratios and pressures.

Methane

Just as for ethanol, the CRECK mechanism was validated for methane at different conditions. Figure 5.3 shows the comparison between the CRECK mechanism and experimental work for the laminar flame speed of methane. Again, it can be seen that a temperature increase introduces an increase in laminar flame speed and that an increase in pressure leads to a decrease in the laminar flame speed.

When comparing Figure 5.3a, Figure 5.3b, and Figure 5.3d, it can be seen that the CRECK mechanism can accurately model the laminar flame speed for varying temperatures, even at higher temperatures (T = 873 K). However, Figure 5.3c (where the temperature is close to the compressor outlet temperature) shows a significant difference between the CRECK mechanism and experimental work from Akram [92]. The data from Akram agreed with simulations made with the GRI 3.0 mechanism, which is a broadly accepted mechanism for the combustion of methane [21]. So, it is concluded that the CRECK mechanism will slightly overestimate the laminar flame speed of methane at the relevant conditions for the Siemens SGT5-200E gas turbine. Lastly, Figure 5.3e and Figure 5.3f show that the CRECK mechanism can cope with elevated pressures.

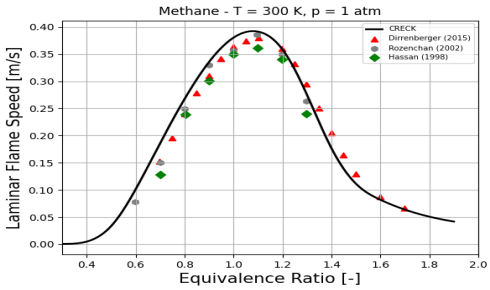

(a) CRECK mechanism versus experimental work at T = 300 K, p = 1 atm [93–95].

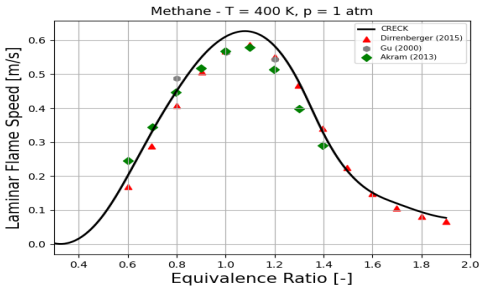

(b) CRECK mechanism versus experimental work at T = 400 K, p = 1 atm [92, 93, 96].

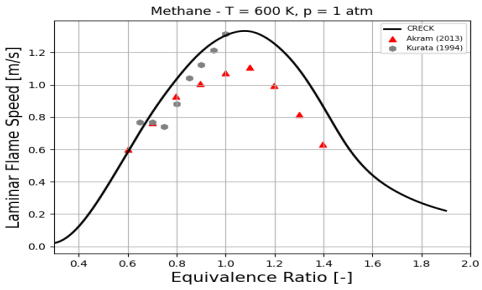

(c) CRECK mechanism versus experimental work at T = 600 K, p = 1 atm [92, 97].

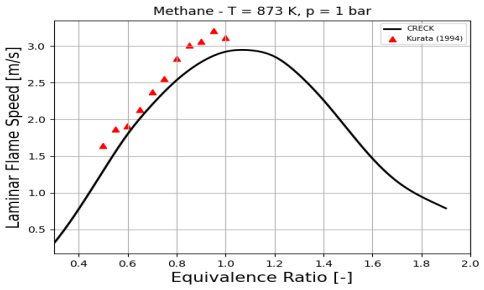

(d) CRECK mechanism versus experimental work at T = 873 K, p = 1 bar [97].

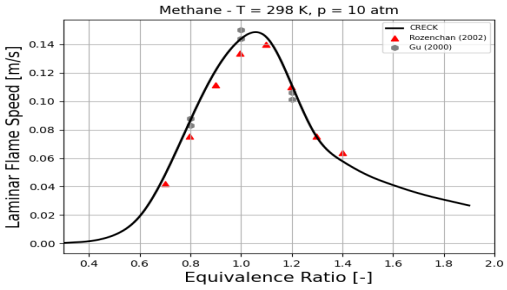

(e) CRECK mechanism versus experimental work at T = 298 K, p = 10 atm [94, 96].

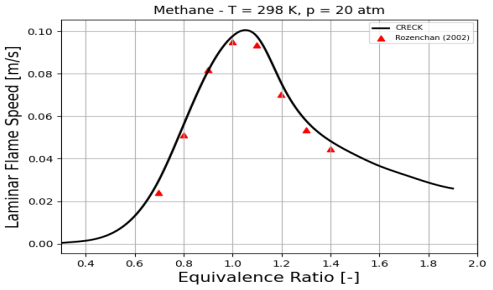

(f) CRECK mechanism versus experimental work at T = 298 K, p = 20 atm [94].

Figure 5.3: Validation of laminar flame speed of methane calculated using the CRECK mechanism (represented by the black lines) for different temperatures and pressures.

The performance of the CRECK mechanism for the autoignition delay time of methane is shown in Figure 5.4. Just as for ethanol, it can be seen that an increase in equivalence ratio and pressure will cause slightly lower autoignition delay times.

Again, the CRECK mechanism shows good results for a broad range of equivalence ratios, pressures, and temperatures. However, Figure 5.4c and Figure 5.4d show some significant differences in the lower temperature regions (T< 1250 K) between the CRECK mechanism and experimental work from Goy (2001) and De Vries (2007) for elevated pressures of 10 and 20 atm [98, 99]. The aforementioned studies used the shock tube method to measure the autoignition delay time for all considered temperatures. In contrast, a more recent study from Burke et al. suggested using the shock tube method only for high-temperature regions and the rapid compression machine method for lower-temperature regions [100]. As the results from the CRECK mechanism are well aligned with the measurements from Burke et al„ it is expected that the mechanism gives a good representation of the autoignition delay time of methane at the relevant gas turbine conditions.

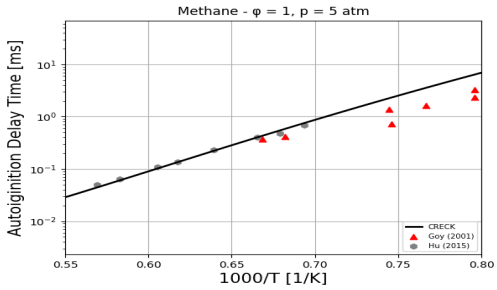

(a) CRECK mechanism versus experimental work at ϕ = 1, p = 5 atm [98, 101].

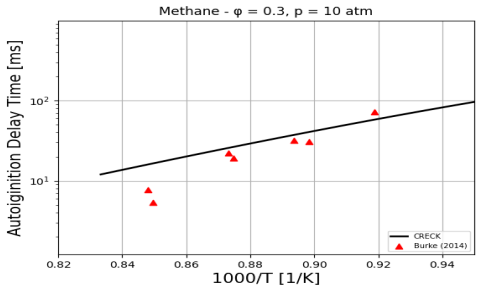

(b) CRECK mechanism versus experimental work at ϕ = 0.3, p = 10 atm [100].

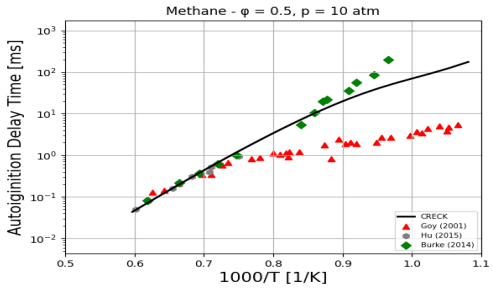

(c) CRECK mechanism versus experimental work at ϕ = 0.5, p = 10 atm [98, 100, 101].

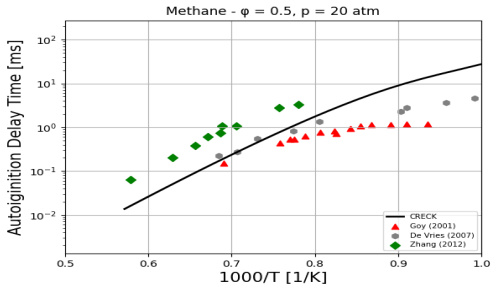

(d) CRECK mechanism versus experimental work at ϕ = 0.5, p = 20 atm [98, 99, 102].

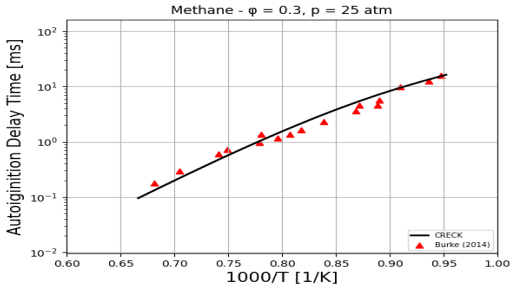

(e) CRECK mechanism versus experimental work at ϕ = 0.3, p = 25 atm [100].

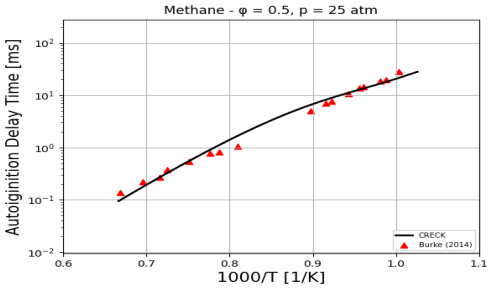

(f) CRECK mechanism versus experimental work at ϕ = 0.3, p = 25 atm [100].

Figure 5.4: Validation of autoignition delay time of methane calculated using the CRECK mechanism (represented by the black lines) for different equivalence ratios and pressures.

Conclusion on Mechanism Performance

Unfortunately, no experimental data was found close to the relevant gas turbine (T = 600 K and p = 11 bar). The different works usually research the effect of varying a single parameter on the laminar flame speed and autoignition delay time. Therefore, the accuracy of the CRECK mechanism for a varying temperature or pressure should be assessed separately. The performance is summarized in Table 5.2.

The CRECK mechanism slightly overestimates the laminar flame speeds for ethanol and methane at a temperature of 600 K and a pressure of 1 atm. As this overestimation is the case for both fuels, this will not significantly affect the comparison. It was also found that an increase in pressure has no major effect on the accuracy of the CRECK mechanism regarding the laminar flame speed prediction of ethanol and methane.

Next to that, the CRECK mechanism was able to give a good representation of the autoignition delay time of ethanol and methane for various equivalence ratios, pressures, and temperature regions.

Table 5.2: Performance of CRECK mechanism on relevant gas turbine conditions

	Laminar Flame Speed	**Autoignition Delay Time**
Ethanol	Minor overestimation at T = 600 K and p = 1 atm Good performance for T = 373 K and p = 10 bar	Good performance for various equivalence ratios, pressures, and temperature regions.
Methane	Minor overestimation at T = 600 K and p = 1 atm Good performance at T = 298 K and p = 10 atm	Good performance for various equivalence ratios, pressures, and temperature regions.

5.3. Results

The adiabatic flame temperature can be determined from the Cantera FreeFlame simulation by taking the maximum value of the temperature that is reached by the flame of the specified mixture. Figure 5.5 displays the results for the adiabatic flame temperature for ethanol and methane versus the equivalence ratio. It can be seen that the adiabatic flame temperatures that are reached are slightly higher for ethanol when compared to methane. However, the differences are relatively small compared to other fuels in Figure 2.7. The green vertical line in Figure 5.5 depicts the required average equivalence ratios of ethanol and methane (both close to 0.55) that were calculated in Section 4.1. It can be seen that the adiabatic flame temperature of ethanol for this equivalence ratio is around 1850 K, and the adiabatic flame temperature of methane is around 1820 K. From literature, it was found that Siemens controls the HR3 burner at a flame temperature of 1773 K [4]. The difference between the adiabatic flame temperature and the control temperature of 1773 K is expected, as the adiabatic flame temperature is a measure under ideal conditions.

The higher adiabatic flame temperature of ethanol suggests that the average equivalence ratio of ethanol should be decreased to ensure the control temperature of the HR3 burner. Because the energy input is reduced, the power output will also be slightly lower when ethanol is used as a fuel. Next to that, Section 2.9 and Section 2.12 explained that the flame temperature is an essential factor that affects the NOx emissions of a gas turbine. Considering a constant control temperature of the flame, no change in NOx emissions is expected due to the difference in adiabatic flame temperature of ethanol and methane.

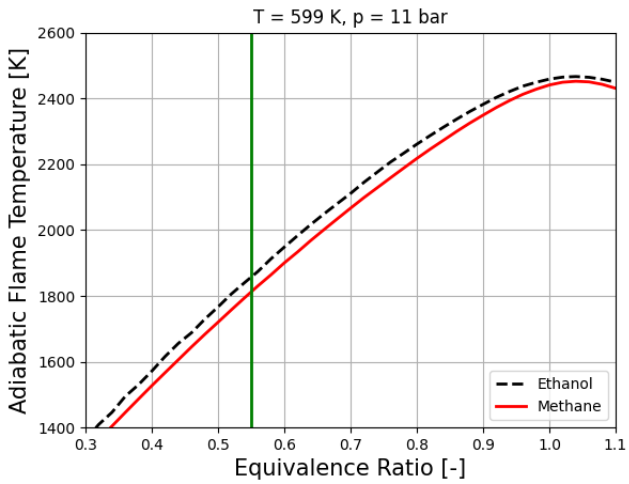

Figure 5.5: Adiabatic flame temperature versus the equivalence ratio for the relevant gas turbine conditions.

Another important parameter that affects the combustion characteristics is the turbulent flame speed. As was explained in Section 2.8, the turbulent flame speed is not a physical property, and past research has struggled to model it accurately. Considering that the turbulent flow and geometry of the burner are not changed for the comparison between ethanol and methane, the laminar flame speed remains an important factor affecting the turbulent flame speed. The laminar flame speed was determined by the Cantera FreeFlame simulation, which models the flame as an one-dimensional planar flame. However, in reality, flames will be wrinkled and stretched. Therefore, another important property for the comparison is the effective Lewis number, which was also determined by the Cantera FreeFlame simulation.

Figure 5.6 shows the laminar flame speed of ethanol and methane versus the adiabatic flame temperature. The green vertical line indicates the aforementioned control temperature of the Siemens HR3 burner (T = 1773 K). It can be seen that for this temperature, the laminar flame speed is significantly higher for ethanol than for methane. At these conditions, ethanol has a laminar flame speed of approximately 0.16 m/s, and methane has a laminar flame speed of 0.09 m/s, meaning that the laminar flame speed is increased by 78% when ethanol is used as the fuel. This difference suggests that the use of ethanol will lead to a higher turbulent flame speed when compared to methane.

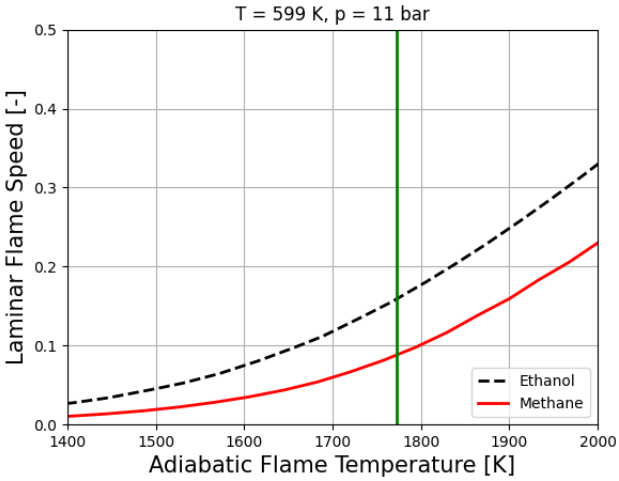

Figure 5.6: Laminar flame speed versus the adiabatic flame temperature for the relevant gas turbine conditions.

Figure 5.7 shows the calculated effective Lewis number for ethanol and methane at the specified conditions. It can be seen that methane has an effective Lewis number close to unity for different adiabatic flame temperatures, whereas ethanol has an effective Lewis number that is significantly larger than unity. Again, the green line represents the HR3 burner control temperature, at which ethanol has an effective Lewis number of 1.56. As explained in Section 2.7, a Lewis number larger than unity will have a smoothing effect on the wrinkled flame, and thereby a dampening effect on the actual flame speed. This means that the difference in turbulent flame speed between ethanol and methane will be smaller than was first expected.

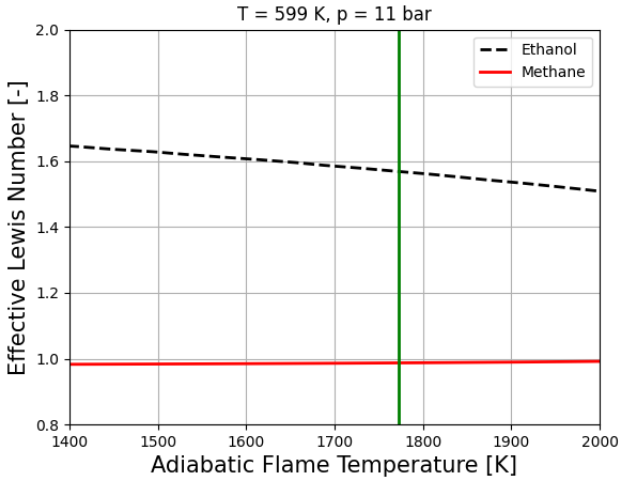

Figure 5.7: Laminar flame speed versus the adiabatic flame temperature for the relevant gas turbine conditions.

As mentioned in Section 2.11, flashback may occur when the flame speed exceeds the local flow velocities. The increase in laminar flame speed, and therefore increased turbulent flame speed, suggests that there is an increased risk of flashback when ethanol is used. However, these increased flashback risks may be within the flashback margin. An experimental study by Blaette et al. showed that hydrogen could be added to natural gas to a value of 60%vol for the Siemens SGT5-4000F gas turbine, which also uses HR3 burners, without causing flashback [103]. The value of the aforementioned research will be assessed by comparing the laminar flame speed and effective Lewis number effects of ethanol to that of hydrogen/methane mixtures. At relevant conditions (T = 723 K and p = 20 bar) for the SGT5-4000F gas turbine, it was found that a 60%vol hydrogen/40%vol methane mixture has a laminar flame speed of approximately 0.17 m/s [104]. Next, it was found that the effective Lewis number is decreased below unity when hydrogen is added to methane [105]. Because the laminar flame speed of ethanol (0.16 m/s) is lower than that of the 60%vol hydrogen/40%vol methane mixture (0.17 m/s), and ethanol has a dampening effect on the turbulent flame speed in contrast to hydrogen due to the different Lewis number effects, it is expected that the use of ethanol will be within the flashback margin that was described by Blaette et al. [103]. In contrast to the higher flashback risks, the use of ethanol will reduce the blowout risks due to the higher flame speed.

Also, the flame position will be affected by the use of ethanol. The higher turbulent flame speed of ethanol suggests that the flame will be shorter, which is in accordance with the study of Blaette et al. [103]. The shorter flame length will cause an increase in NOx emissions as the residence time at higher temperatures is increased. Next to that, the shorter flame length will alter the combustion dynamics, as the 'time lag' is shortened due to the shorter flame length. Therefore, it can be expected that the driving energy source for the combustion dynamics shifts to higher frequency nodes. This could be beneficial as the SGT5-2000E gas turbines have large silo combustors with relatively low natural frequencies. But besides this, it is hard to determine whether the use of ethanol will be really beneficial for the combustion dynamics. It is expected that combustion tuning is needed to ensure acceptable behavior regarding the combustion dynamics.

Another effect of ethanol on the combustion characteristics is the increased risk of autoignition of the unburned fuel-air mixture. The autoignition delay time was calculated with the use of the Cantera IdealGasReactor simulation to compare ethanol to methane. The autoignition delay time was plotted against the temperature for three different ethanol and methane mixture strengths. This can be seen in Figure 5.8. It can be seen that the ethanol mixtures have a shorter autoignition delay time than the methane mixtures. Next to that, it can be noted that a higher equivalence ratio leads to shorter autoignition delay times. The average equivalence ratio of both ethanol and methane was close to 0.55, but it can be concluded from Figure 5.8 that there is an increased risk of autoignition for fuel-rich pockets. This means that enhanced mixing decreases the risk of autoignition.

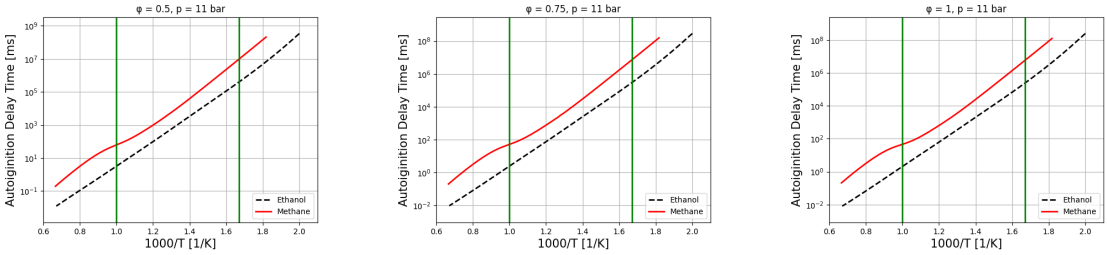

(a) ϕ = 0.5, p = 11.1732 bar (b) ϕ = 0.75, p = 11.1732 bar (c) ϕ = 1, p = 11.1732 bar

Figure 5.8: Autoignition delay time versus 1/T for ethanol and methane at different equivalence ratios..

Mixing of the fuel and air in the HR3 burner occurs at a temperature of approximately 600 K (denoted by the vertical green line at 1000/T = 1.67), which is close to the compressor discharge temperature. As can be seen from Figure 5.8, for all three mixture strengths, both ethanol and methane will have autoignition delay times larger than $10^5 ms$. These values are so high compared to the mixing section residence time that autoignition in the actual mixing section is not expected. However, there are regions where the unburned reactants get heated by the burned products due to the existence of recirculation zones. From literature, it was deduced that the unburned reactants typically reach a temperature of approximately 1000 K [104]. This temperature is denoted by the vertical green lines in Figure 5.8 at 1000/T = 1. For this temperature, ethanol has an autoignition delay time in the order of 10^0 ms, and methane has an autoignition delay time in the order of 10^1 ms. This means there is a significantly higher probability of periodic flashes of the fuel-air mixture when ethanol is used as a fuel. These periodic flashes could eventually lead to a steady flashback. Therefore, it is concluded that the shorter autoignition delay times of ethanol increase the risk of possible flashback compared to methane.

Conclusion on Kinetic Modeling Study

In conclusion, the results from the kinetic modeling study show that ethanol has a higher laminar flame speed than methane, which also leads to an increase in turbulent flame speed. However, this increase is not directly proportional, as the Lewis number of ethanol has a smoothing effect on the flame front. The increase in turbulent flame speed causes an increase in flashback risks, but it is expected that this will be within the margin of the gas turbine. The higher turbulent flame speed of ethanol will also cause shorter flames. Lastly, it was found that ethanol leads to higher probabilities of autoignition.

6

Fuel-Air Mixing Study

This chapter will focus on how the use of ethanol will affect the quality of fuel-air mixing within the combustor when compared to methane. As mentioned in Section 2.12, the quality of fuel-air mixing has a significant impact on the NOx emissions of a gas turbine due to the almost exponential relation between the NOx emissions and the temperature. Next to that, the quality of fuel-air mixing also affects the flame length and combustion dynamics. It was discussed in Chapter 4 that ethanol has a lower LHV compared to methane, which means that a slightly higher volume flow will be required to ensure the same energy output from the gas turbine. This indicates different mixing characteristics, which will be studied by a CFD analysis of the HR3 burner. All CFD simulations are performed with the use of Ansys Fluent.

6.1. Turbulence Model Validation

The mixing of the fuel and air will be evaluated with the help of a steady RANS model. RANS is a CFD approach where the flow variables in the Navier-Stokes equations will be averaged over time. This limits the model's accuracy, but it has a relatively high computational efficiency compared to other CFD approaches. As mentioned in Section 2.3, the Boussinesq hypothesis and eddy viscosity models are used to close the RANS equations. This study will assess two different eddy viscosity models: the Realizable $k-\epsilon$ and SST $k-\omega$ model [29, 106]. The aforementioned models were chosen because a study by Karvinen and Ahlstedt proved that both models could accurately model a jet in crossflow [107]. To assess the performance of the models above, they will be used to simulate a reference case, and these results will be compared to experimental data.

Reference Case

As the mixing section of the HR3 burner consists of multiple opposed jets in a crossflow, it was decided to use the paper from Galeazzo et al. as a reference case [20]. This paper performed experimental work on the turbulent mixing of a single jet into a crossflow, where both flows consist of air. An overview of the experimental domain can be seen in Figure 6.1, and the boundary conditions are summarized in Table 6.1. The experimental domain consists of a channel with a square cross section of 108 mm X 108 mm. Air will flow into this channel with a bulk velocity of 9.08 m/s, a turbulence intensity of 1.5 %, and a Reynolds number of $6.24 * 10^4$. A jet with a diameter of 8 mm will enter the channel 328 mm downstream of the inlet. This jet has a bulk velocity of 37.72 m/s, a turbulence intensity of 7 %, and a Reynolds number of $1.92 * 10^4$. The pipe that is used to create the jet inlet is 250 mm, which ensures a fully developed velocity profile.

Table 6.1: Boundary conditions for the reference case [20].

Section	Parameter	
Crossflow Inlet	Bulk Velocity	9.08 m/s
	Turbulence Intensity	1.5%
	Re	$6.24 * 10^4$
Jet Inlet	Bulk Velocity	37.72 m/s
	Turbulence Intensity	7%
	Re	$1.92 * 10^4$

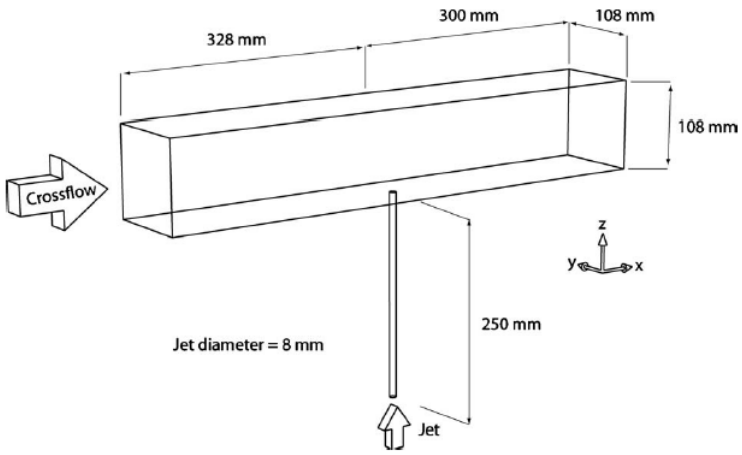

Figure 6.1: Overview of the domain for the experimental setup [20].

Different flow variables were measured using Laser Induced Fluorescence (LIF) and Particle Image Velocimetry (PIV). The former technique measures substances by exciting them with a laser, causing light emissions used for analysis or visualization, and the latter technique measures fluid flow by tracking particles illuminated by lasers. Aerosol particles were added to the air flows for the PIV measurements, and NO_2 was added to the jet flow for the LIF measurements. The measurement setup can be seen in Figure 6.2.

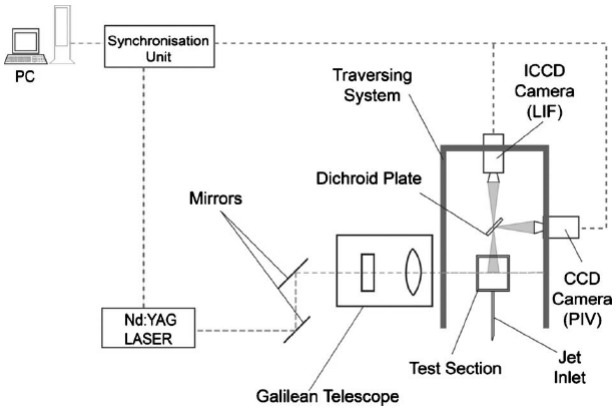

Figure 6.2: Overview of the setup for the LIF and PIV measurements [20].

Mesh Refinement

It is important to do a mesh refinement study to ensure that the results from the CFD analysis are accurate. A mesh refinement study aims to determine the spatial discretization errors of the simulations. These spatial discretization errors should approach zero when the mesh is refined. In other words, when the solutions of simulations on meshes converge for an increasing level of refinement, it can be said that the mesh refinement is successful, and the fine mesh will deliver accurate results.

This mesh refinement study was performed for the Realizable $k-\epsilon$ model, where three meshes were used ranging from coarse to fine. The coarse mesh consists of 4 million cells, the medium mesh consists of 10 million cells, and the fine mesh consists of 12 million cells. From Figure 6.3, it can be concluded that the results for the fine and finest mesh are almost identical, which indicates that the further use of the finest mesh is acceptable.

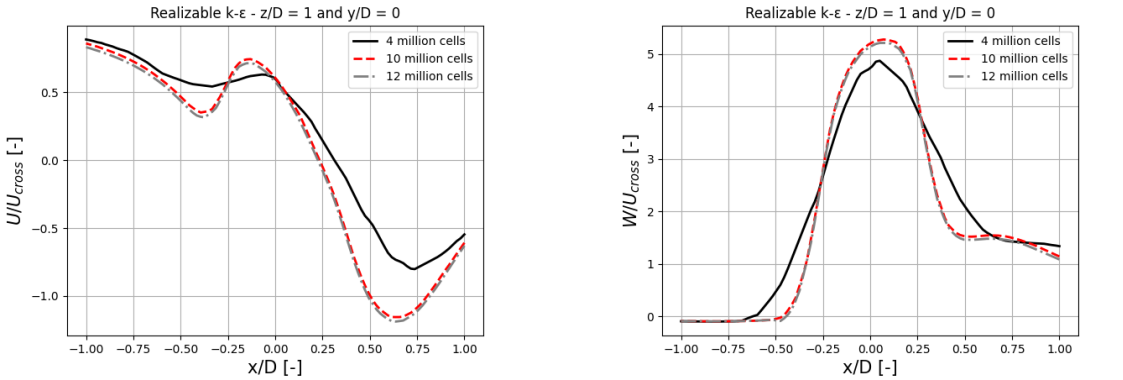

(a) Normalized velocity in the x-direction versus location in the x-direction.

(b) Normalized velocity in the z-direction versus location in the x-direction.

Figure 6.3: Results from the refinement study for the Realizable $k-\epsilon$ model for the coarse, fine and finest mesh.

Turbulence Model Comparison

This section will compare the Realizable $k-\epsilon$ and the SST $k-\omega$ models with experimental data from Galeazzo et al. [20]. The simulations are not expected to match the experimental data perfectly, as RANS simulations simplify the real flow. Both simulations used a first-order upwind scheme to ensure stability. Higher-order schemes were also considered, but these did not significantly increase the accuracy. Figure 6.4 displays the normalized velocity in the x- and z-direction for a varying location in the x-direction. It can be seen that the results of both models have the same shape as the experimental data. However, when considering Figure 6.4a, it can be concluded that the SST $k-\omega$ gives a better representation of the normalized velocity in the x-direction. Figure 6.5 displays the normalized velocity in the x-direction for a varying location in the z-direction. As can be seen, both models are similarly accurate in representing the velocity fields throughout different locations.

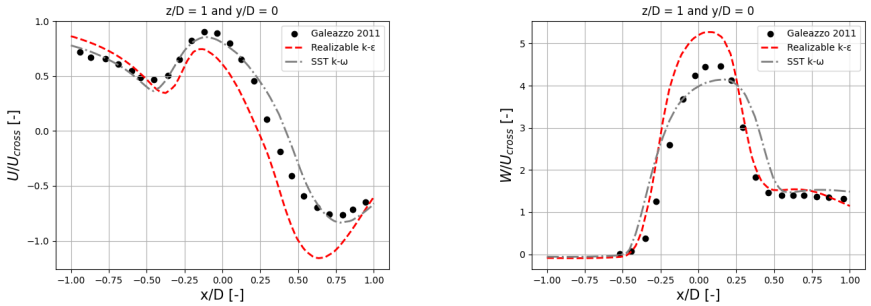

(a) Normalized velocity in the x-direction versus location in the x-direction.

(b) Normalized velocity in the z-direction versus location in the x-direction.

Figure 6.4: Turbulence model validation at z/D =1 and y/D = 0. Experimental work from Galeazzo et al. (•) is compared to simulations of the Realizable $k-\epsilon$ model and SST $k-\omega$ model [20].

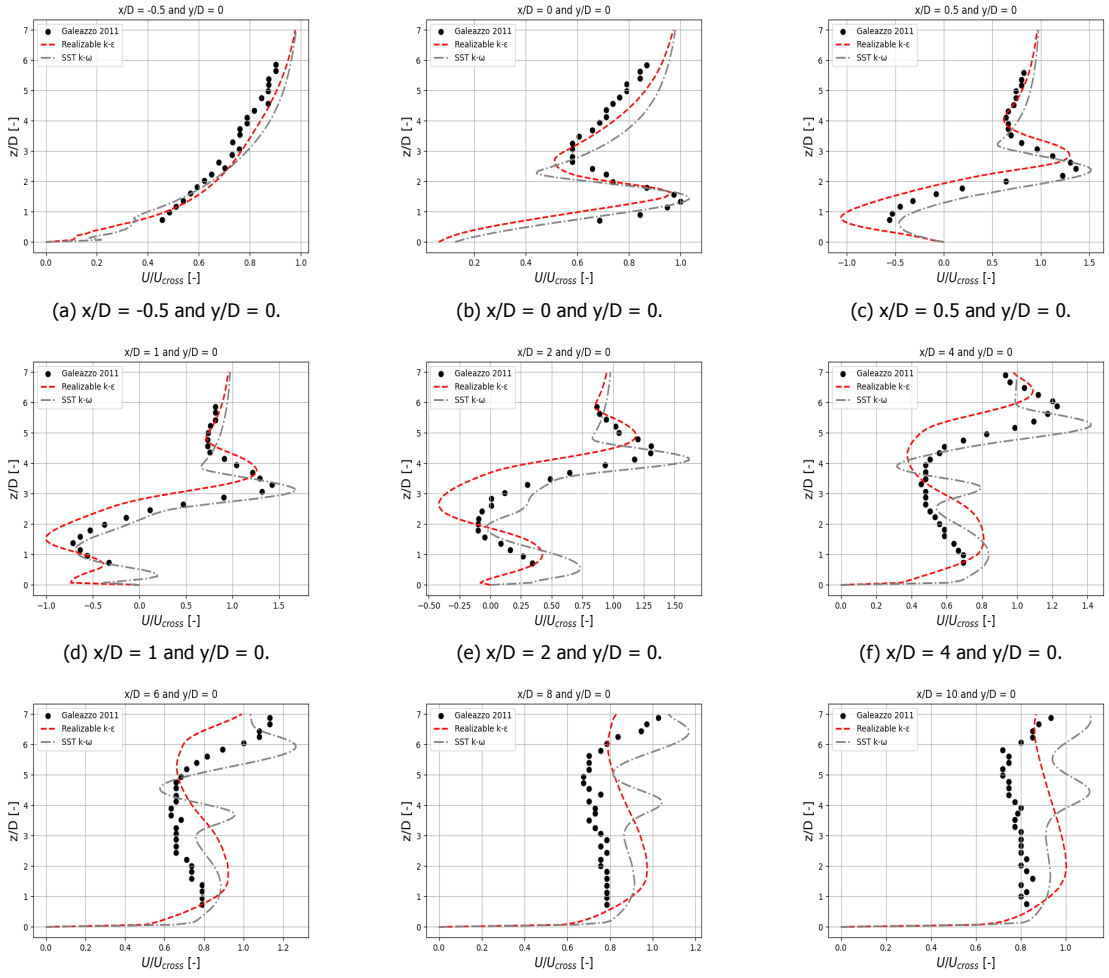

(a) x/D = -0.5 and y/D = 0.

(b) x/D = 0 and y/D = 0.

(c) x/D = 0.5 and y/D = 0.

(d) x/D = 1 and y/D = 0.

(e) x/D = 2 and y/D = 0.

(f) x/D = 4 and y/D = 0.

(g) x/D = 6 and y/D = 0.

(h) x/D = 8 and y/D = 0.

(i) x/D = 10 and y/D = 0.

Figure 6.5: Normalized velocity in the x-direction plotted versus location in the z-direction. Experimental work from Galeazzo et al, (•) is compared to simulations of the Realizable $k-\epsilon$ model and SST $k-\omega$ model [20].

Figure 6.6 shows the performance of the Realizable $k-\epsilon$ and the SST $k-\omega$ model for the mixing of the jet in crossflow. The data from the simulations was retrieved with the use of the user-defined scalar function in Ansys Fluent. Both models can roughly model the mixing, but there are some differences with the experimental data. However, it can be seen that the SST $k-\omega$ model performs slightly better

than the Realizable $k-\epsilon$ model.

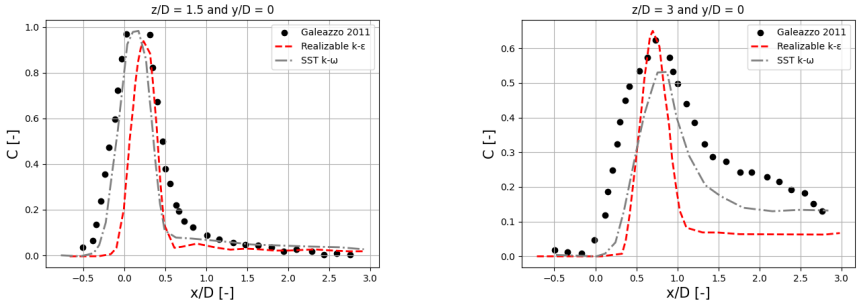

(a) z/D = 1.5 and y = 0.

(b) z/D = 3 and y = 0.

Figure 6.6: Dimensionless concentration versus the location in the x-direction. Experimental work from Galeazzo et al. (•) is compared to simulations of the Realizable $k-\epsilon$ model and SST $k-\omega$ model [20].

Overall, it can be concluded that both the Realizable $k-\epsilon$ and the SST $k-\omega$ can provide a reasonable representation of the flows. It was decided to use the SST $k-\omega$ model for the remaining part of the CFD study, as this turbulence model combines a $k-\epsilon$ and a $k-\omega$ model. This means that it will have the benefits of a $k-\omega$ model in regions that are close to a wall, and it will use the better performing $k-\epsilon$ model in regions further away from the walls.

6.2. HR3 Burner Model

Geometry

This study focuses on the differences in mixing between ethanol and methane, so it is decided that only a part of the actual HR3 burner will be modeled. As explained in Section 1.2, there are fuel inlets within the blades of the diagonal burner. Each swirler passage, i.e., the channel in between two swirler blades, is expected to have the same mixing characteristics. Such a swirler passage is highlighted in Figure 6.7. It can be seen that the cross section of each swirler passage may be approximated by an isosceles trapezoid.

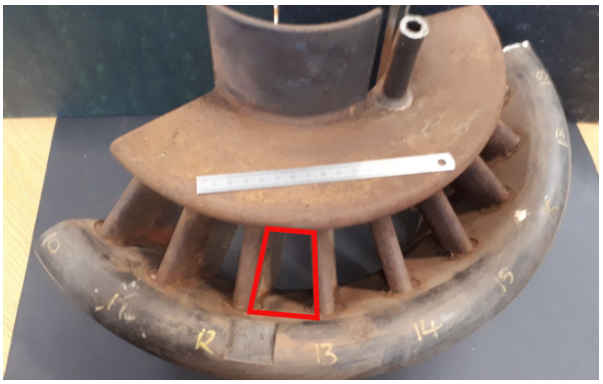

Figure 6.7: Top view of the HR3 burner. The picture is taken by Uniper.

Fuel is injected slightly downstream of the entrance of the swirler passage with five directly opposed pairs of jet inlets. In reality, the swirler passage is slightly converging, leading to an increase in the air velocity. However, for this study, it was assumed that each swirler passage has a constant cross section. The mixing zone is, therefore, approximated by a constant cross section trapezoidal prism with a length of 165 mm starting from the jet inlets. The dimensions of the cross section can be found in Figure 6.8. The diameters and spacing of the jet inlets are measured by Uniper but will be left out of this report for the sake of confidentiality.

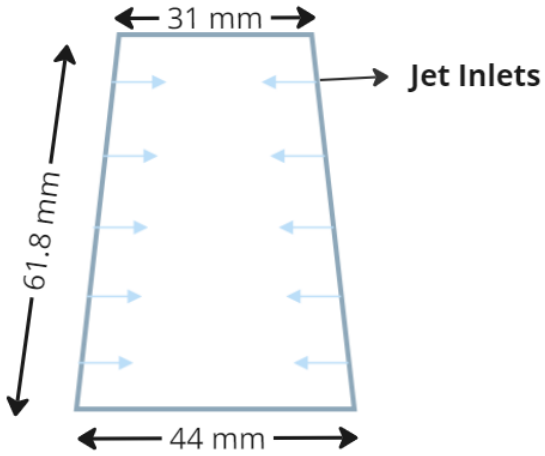

Figure 6.8: Relevant dimensions of the HR3 burner provided by Uniper.

The simplified geometry of the swirler passage was recreated with the use of the DesignModeler module of Ansys Fluent and can be seen in Figure 6.9. The trapezoidal cross section is displayed on the xy-plane so that the length of the swirler passage is perpendicular to this plane (z-direction). The origin was taken to be in the center of the cross section at the height of the jet inlets. As seen, the fuel jet will be injected via tubes, ensuring a developed velocity profile. Using the same reasoning, it was decided to have a space of 100 mm between the crossflow inlet and the jet inlets. Then, a mesh was created with the Fluent Meshing module of Ansys Fluent. The mesh is created using unstructured polyhedral cells to reduce the total number of cells. Next to that, polyhedral cells perform well when approximating a gradient, as polyhedral cells have many sides and, thereby also, many neighboring cells.

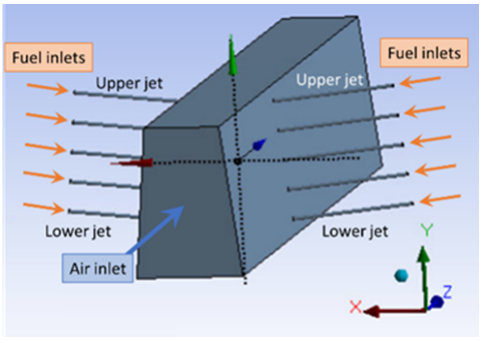

Figure 6.9: Simplified geometry of HR3 burner swirler passage from Ansys DesignModeler.

Mesh Refinement

As for the reference case, the HR3 burner model mesh will be assessed by a mesh refinement study for both the ethanol and methane cases. The equivalence ratio will be evaluated at a line with varying locations in the x-direction, where y = 0 mm and z = 165 mm. This was done for three meshes, where the coarse mesh consists of 9.5 million cells, the medium mesh consists of 14.2 million cells, and the fine mesh consists of 20.9 million cells. As seen in Figure 6.10, the solution for the equivalence ratio converges but has not yet reached the highest possible accuracy. However, as further mesh refinement was limited by the computation capability of the setup used, it was decided that the fine mesh gave acceptable solutions.

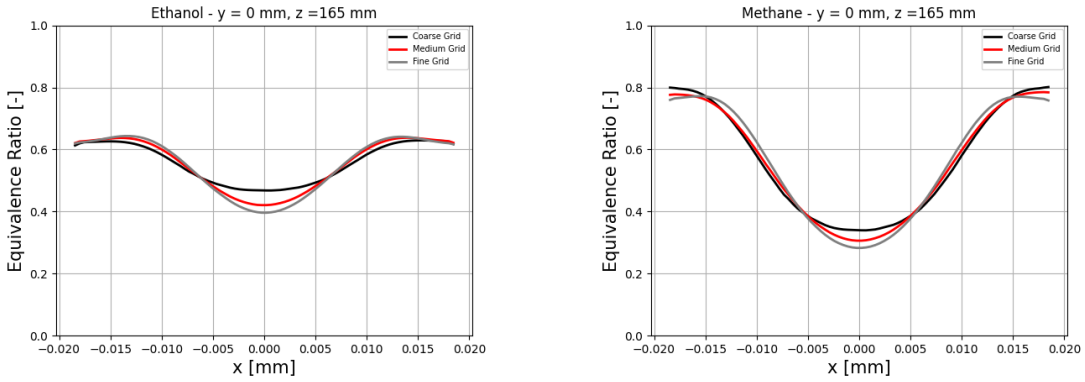

(a) Location in the x-direction versus equivalence ratio for the ethanol case.

(b) Location in the x-direction versus equivalence ratio for the methane case.

Figure 6.10: Refinement study with a coarse, medium and fine mesh.

Final mesh

The final mesh can be seen in Figure 6.11. Figure 6.11b and Figure 6.11c clearly show that the mesh is relatively coarse in the region upstream of the jet inlets. A maximum cell length of 0.35 mm was chosen for the region downstream of the jet inlets. In agreement with the literature, prism layers were added to regions close to the wall [108]. Both the mesh refinement and the prism layers can be seen in Figure 6.11d, and they ensure accuracy in regions where larger gradients are expected. This resulted in a mesh with 20,858,499 cells in total.

The orthogonal quality is an indication given by Ansys Fluent for the quality of the mesh. Bad cells will have an orthogonal quality close to 0, and good cells will have an orthogonal quality close to 1. When the minimum orthogonal quality is lower than 0.1, the mesh is considered to be of low quality [27]. However, as the final mesh has a minimum orthogonal quality of 0.4, the mesh has an acceptable orthogonal quality.

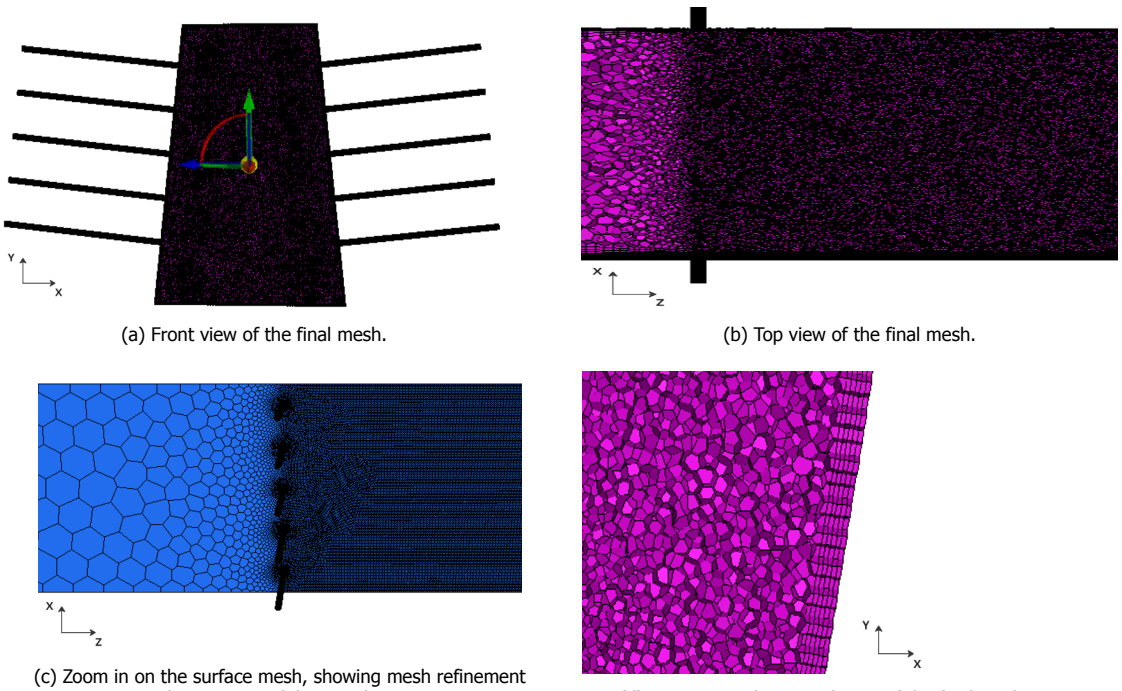

(a) Front view of the final mesh.

(b) Top view of the final mesh.

(c) Zoom in on the surface mesh, showing mesh refinement downstream of the jet inlets.

(d) Zoom in on the prism layers of the final mesh.

Figure 6.11: Plots of the final mesh used for the HR3 burner model.

As mentioned in Section 2.2, near-wall regions can be divided into three regions: the viscous sub-layer, the buffer layer, and the fully-turbulent layer. For CFD simulations, it is important to check the y^+ value of the mesh to get a better overview of the flow. As mentioned before, a $k-\omega$ model performs better in the viscous sub-layer, and $k-\epsilon$ models perform better in the fully turbulent layer, where the log-law is valid. The variables in the buffer layer are normally approximated with the use of wall functions. As turbulence will be the dominant factor in the fuel-air mixing, it is decided to assume fully turbulent flow, so y^+ that are larger than twenty are required. It can be seen in Figure 6.12 that the minimum y^+ value is 18.9. This is considered acceptable, as Ansys Fluent ensures that the SST $k-\omega$ model can be used for all y^+ values [27]. Next to that, most regions show values larger than twenty.

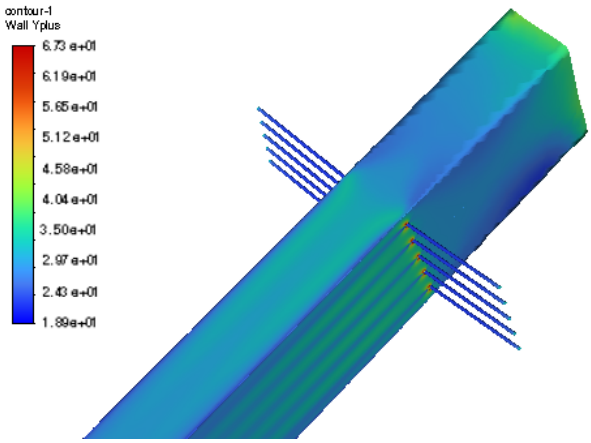

Figure 6.12: Overview of the y^+ values of the first layer of cells adjacent to the surface.

An overview of the final mesh is given in Table 6.2.

Table 6.2: Overview of the final mesh settings

Parameter	
Number of Cells	20,858,499
Mesh Type	Polyhedral
Number of Prism Layers	5
Orthogonal Equality	>0.4
Refinement Region	0<z<0.165 mm
Maximum Element Size in Refinement Region	0.35 mm
Maximum Element Size in Jet Inlet Region	0.075 mm
Maximum Element Size in Other Regions	7.5 mm

Boundary Conditions

For the fuel-air mixing study, three cases will be evaluated and compared. The first case is the mixing of ethanol with a temperature of 467 K and air. The second case is the mixing of methane with a temperature of 293 K and air. For the third case, the temperature of methane will be increased to 467 K to get a better overview of the temperature effects on the mixing of the fuels. For all three cases, the pressure and temperature of air were set equal to the compressor discharge conditions, which are respectively 11.2 bar and 608 K.

Mass flow inlet boundary conditions were used in Ansys Fluent for the crossflow inlet and the jets inlet. Considering that a Siemens SGT5-200E gas turbine has two silo combustors, each silo combustor

includes eight HR3 burners, each HR3 burner has twenty blades, and each blade has ten fuel holes, the mass flow of Table 4.1 should be divided by 3200 to get the mass flow for the boundary condition at the jet inlets. For the boundary condition at the crossflow inlet, $\dot{m_{air}}$ should be divided by 320. For both mass flow boundary conditions, it was assumed that the turbulent intensity was 10%, as both flows have Reynolds numbers in the order of millions [27, 109]. The hydraulic diameters of the air and jet inlets were calculated using the given physical dimensions. The hydraulic diameters and turbulent intensities are the same for the three studied cases.

In Ansys Fluent, wall boundary conditions were set for the walls of the HR3 burner swirler passage model. Lastly, a pressure outlet boundary condition was selected for the crossflow outlet. All mass flow inlet boundary conditions are given in Table 6.3. Note that the air flows are the same for the three cases.

Table 6.3: Used mass flow inlet boundary conditions for the CFD simulations.

Case	Region	Specific Information
1 - Ethanol	Crossflow Inlet	Mass Fraction: 0.79 N_2/0.21 O_2 , Massflow = 0.78 kg/s , T = 608 K
	Jet Inlet	Mass Fraction: 1 C_2H_5OH , Massflow = 0.00457 kg/s , T = 467 K
2 - Methane	Jet Inlet	Mass Fraction: 1 CH_4 , Massflow = 0.00244 kg/s , T = 293 K
3 - Methane (High T)	Jet Inlet	Mass Fraction: 1 CH_4 , Massflow = 0.00244 kg/s , T = 467 K

6.3. Results

Figure 6.13a, Figure 6.13b, and Figure 6.13c give an overview of how the fuel enters the swirler passage. It can be seen that the ten jets that enter the crossflow follow a typical jet in crossflow trajectory. The aforementioned figures display an isosurface where the equivalence ratio equals one. From Table 4.1, it can be derived that in Ansys Fluent, the mass fraction should be set to 0.055 and 0.030 for ethanol and methane, respectively, to make the isosurface. The turbulent kinetic energy k is plotted along the isosurface, where higher values of k indicate the existence of more turbulent eddies. The regions close to the jet inlets are expected to experience the highest fluctuations in flow variables. This is confirmed by Figure 6.13a, Figure 6.13b, and Figure 6.13c, as these figures show the highest values of k.

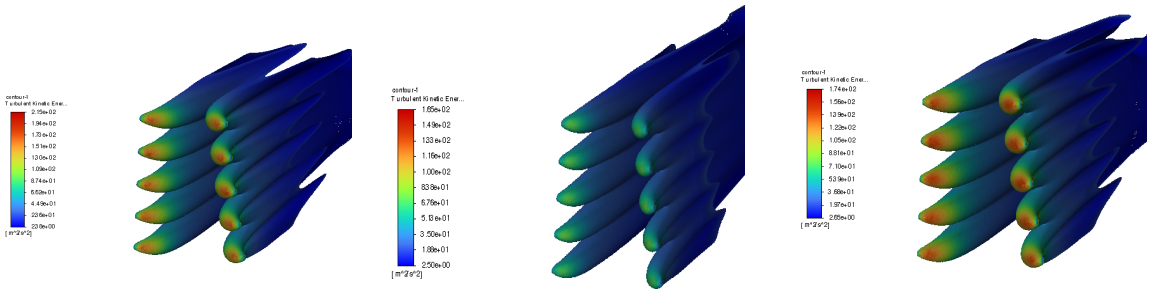

(a) Case 1 - Ethanol (b) Case 2 - Methane (c) Case 3 - Methane (High T)

Figure 6.13: Turbulent Kinetic Energy k at a defined isosurface, where the equivalence ratio is 1.

The equivalence ratio can also be normalized with the average equivalence ratio of the fuel and air mixture, which was determined with the use of Table 6.3. The mixing of the three cases will be compared using the normalized equivalence ratio, which is plotted for different cross sections of the swirler passage in Figure 6.14. It is important to notice that the scales change for each location in the

z-direction. This means that the scales are the same for each row in Figure 6.14.

Just downstream of the jet inlets (first row in Figure 6.14), small regions with a high normalized equivalence ratio can be seen, where the rest of the cross section does not contain any fuel yet as these regions have a normalized equivalence ratio of zero. The small regions with a high normalized equivalence ratio clearly represent the jets that penetrate the air crossflow. Further downstream, the jet shapes become more vague as the jet and crossflow mix. Next to that, the quality of mixing increases further downstream of the jet inlets for all three cases. This can be seen from the changing scales for an increase in Z, which is the location in the z-direction.

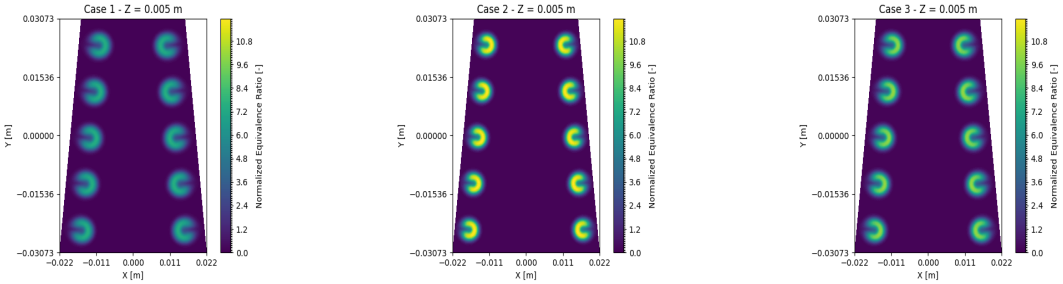

(a) Z = 0.005 m (b) Z = 0.005 m (c) Z = 0.005 m

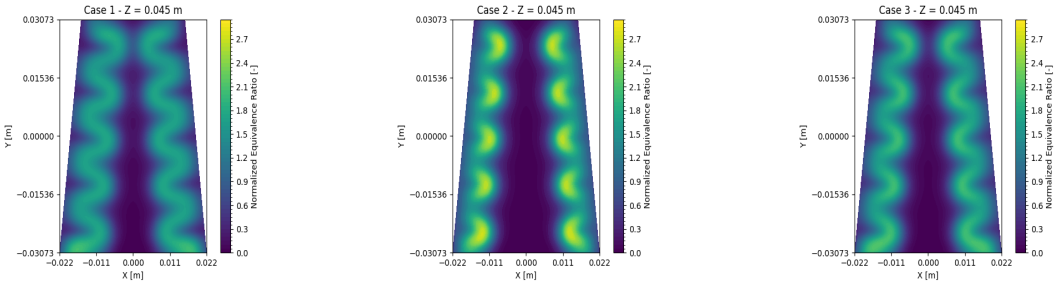

(d) Z = 0.045 m (e) Z = 0.045 m (f) Z = 0.045 m

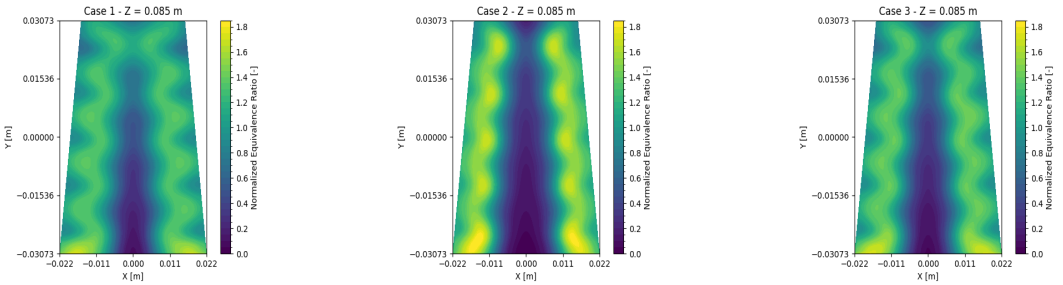

(g) Z = 0.085 m (h) Z = 0.085 m (i) Z = 0.085 m

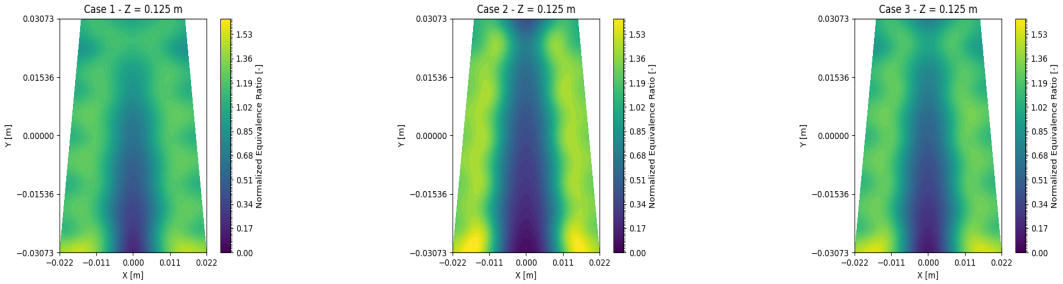

(j) Z = 0.125 m (k) Z = 0.125 m (l) Z = 0.125 m

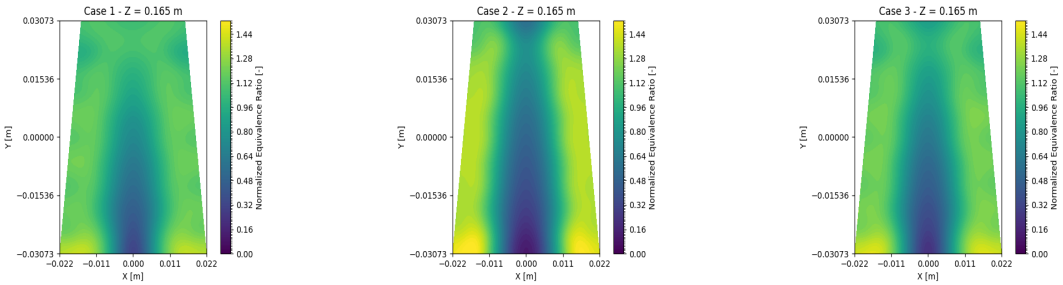

(m) Z = 0.165 m (n) Z = 0.165 m (o) Z = 0.165 m

Figure 6.14: Normalized equivalence ratio at different xy-planes, where the left column denotes Case 1 (Ethanol), the middle column is Case 2 (Methane), and the right column is Case 3 (Methane - High T).

However, it should be noted that Case 1 (Ethanol) and Case 3 (Methane - High T) have a better quality of mixing than Case 2 (Methane). This can be explained by the momentum flux ratio J, which was mentioned in Equation 2.50. A higher momentum flux ratio means that the jet will penetrate further into the crossflow. It was calculated that the momentum flux ratio J was equal to 5.27, 3.78, and 4.77 for, respectively, Case 1 (Ethanol), Case 2 (Methane), and Case 3 (Methane - High T). As Case 2 (Methane) has the lowest momentum flux ratio, the jets will penetrate less deep into the crossflow, leading to a lower quality of mixing.

Another thing that can be noted from Figure 6.14 is that the upper region of the cross section is better mixed than the lower region of the cross section. This can be explained by the trapezoidal shape of the cross section. Because of this shape, the upper region will be smaller than the lower region, and therefore, the distance of the opposing jets within the crossflow will be smaller for the upper region. This can be seen in Figure 6.15, Figure 6.16 and Figure 6.17. The left figures display the mass fraction of the fuel in an xz-plane at the lower jet inlets, and the right figures display the mass fraction of the fuel in an xz-plane at the upper jet inlets. Next to that, the difference in momentum flux ratios between the three cases can also be seen when you compare Figure 6.15b, Figure 6.16b, and Figure 6.17b.

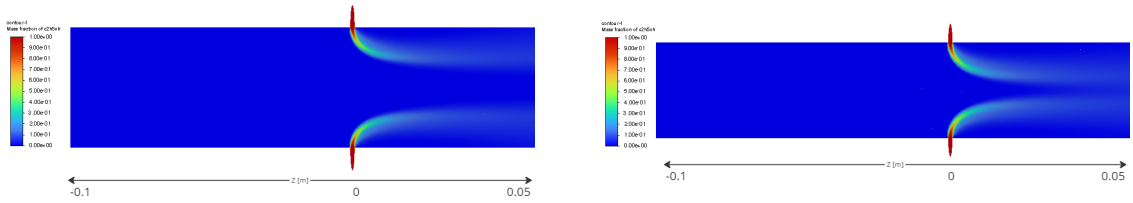

(a) Lower jet inlets (b) Upper jet inlets

Figure 6.15: Contour plot of the mass fraction of ethanol for Case 1.

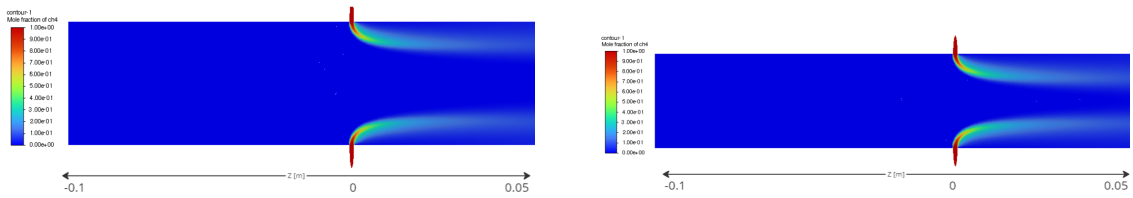

(a) Lower jet inlets (b) Upper jet inlets

Figure 6.16: Contour plot of the mass fraction of methane for Case 2.

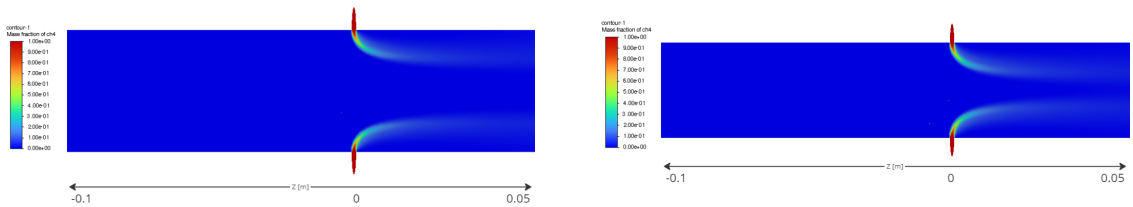

(a) Lower jet inlets (b) Upper jet inlets

Figure 6.17: Contour plot of the mass fraction of methane for Case 3.

The increased quality of mixing downstream of the jet inlets can also be explained by the normalized mass flow weighted standard deviation of the fuel distribution at a specific plane, which is denoted as

S_N and was mentioned before in Section 2.13. Figure 6.18 displays the relation between the quality of mixing and the location in the z-direction. As expected, Case 2 (Methane) has the poorest mixing quality at the outlet of the swirler passage.

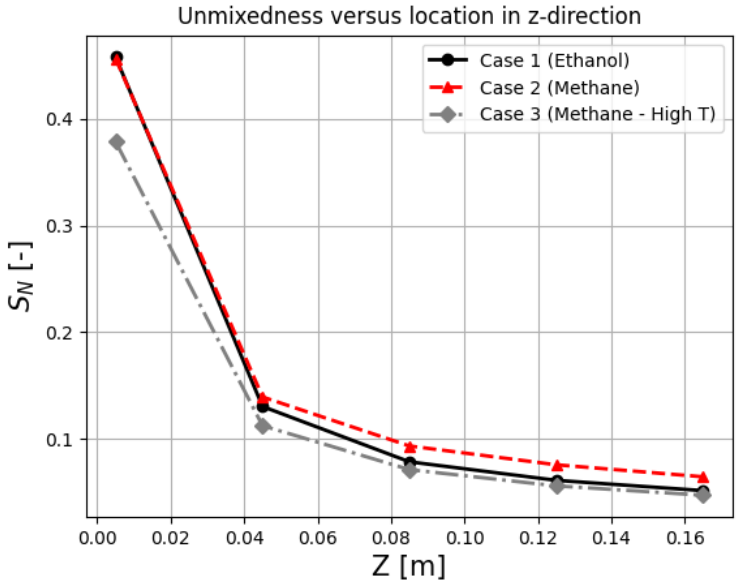

Figure 6.18: Normalized mass flow weighted standard deviation of the fuel distribution s_N versus the location in the z-direction for Case 1, Case 2 and Case 3.

Figure 6.18 also shows that Case 3 (Methane - Hight T) has a slightly better quality of mixing than Case 1 (Ethanol). This seems to contradict the momentum flux ratio reasoning discussed earlier in this section. To explain the difference in the quality of mixing between Case 1 (Ethanol) and Case 3 (Methane - High T), the diffusion coefficient was determined at different xy planes downstream of the jet inlets. An average diffusion coefficient was calculated at each plane, which can be seen in Figure 6.19. Figure 6.19 shows that Case 3 (Methane - High T) has a slightly higher diffusion coefficient throughout the mixing section when compared to Case 1 (Ethanol). This means that the turbulent mixing will also be slightly better for Case 3 (Methane - High T), which explains the differences in unmixedness of Figure 6.18.

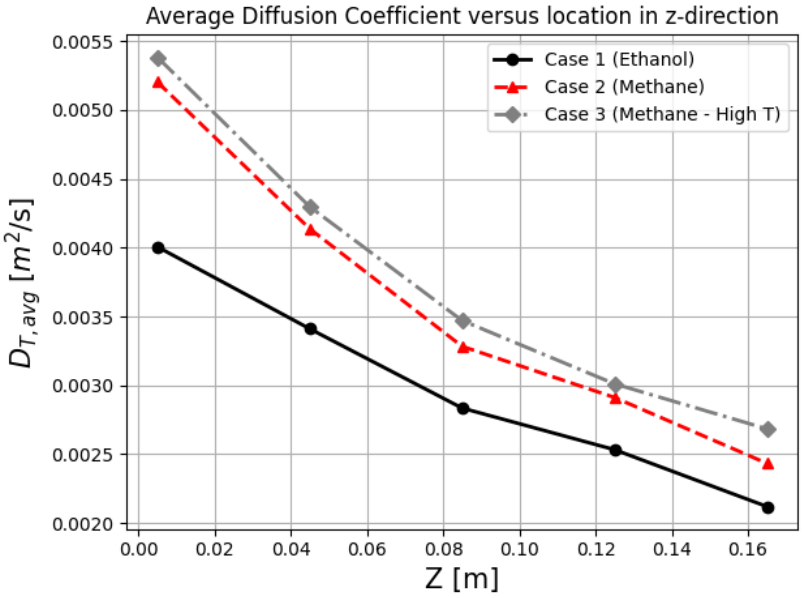

Figure 6.19: Average diffusion coefficient versus the location in the z-direction for Case 1, Case 2 and Case 3.

Conclusion on Fuel-Air Mixing Study

In conclusion, the results from the fuel-air mixing study show that the use of ethanol will be beneficial for the quality of mixing when compared to methane. However, it should be noted that the difference in the momentum flux ratio of ethanol and methane mainly causes this effect. The difference in momentum flux ratio is caused by the different fuel temperatures, which are 467 K for ethanol and 293 K for methane. As was explained in Section 2.12, poor quality of mixing will lead to higher NOx emissions. So, solely based on the quality of mixing, it can be concluded that the implementation of ethanol will be beneficial for the NOx emissions. Next to that, it is expected that the better quality of mixing of ethanol leads to a shorter and more uniform flame. Just as in Chapter 5, it can be reasoned that a shorter flame will decrease the 'time lag', and therefore favors higher frequency combustion instabilities.

7

Conclusion and Recommendations

This chapter concludes the research on the implementation of ethanol as a drop-in fuel for the Killingholme power plant. First of all, the research questions will be answered in Section 7.1, and later on recommendations for further research will be provided in Section 7.2.

7.1. Conclusion

To decarbonize the power generation sector, interest has shifted towards the use of biofuels as these are made from biomass so their use leads to a closed carbon cycle. Currently, the Killingholme power plant is still using natural gas, but biofuels can be prevaporized and premixed to mimic the natural gas characteristics. Ethanol is an interesting biofuel, as it has a relatively low boiling point, meaning that the evaporation process is not too energy-intensive. However, the implementation of ethanol would cause some differences regarding the process design and combustion characteristics. The research objective and additional research questions were:

How does the use of ethanol affect the process design and the combustion characteristics of the natural gas-fired power plant at Killingholme?

Process Design:

- What are the opportunities for heat integration to evaporate the ethanol during baseload operation?
- How can ethanol be implemented in terms of storage and fuel handling?

Combustion Characteristics:

- Are there any increased risks of autoignition?
- How does the use of ethanol affect the flame length/position?
- Does the use of ethanol introduce any increased flashback/blowoff risks?
- How does the use of ethanol affect the NOx emissions?
- What would be the effect of ethanol on the combustion dynamics?

First of all, ethanol should be heated to 467 K to be in vapor form at the relevant gas turbine conditions at Killingholme. Next to that, as ethanol has a lower LHV than natural gas (and methane), the mass flow rate should be increased to ensure the same energy output for the Killingholme power plant. With the use of data from a baseload performance test provided by Uniper, it was determined that the required mass flow rate of ethanol was 16.2 kg/s. A process design was made for the heat integration during baseload operation. Important additions to the process design are the steam generator, ethanol evaporator, and ethanol preheater. Flue gas runs through the steam generator to produce

steam, which will be used for the evaporation process of ethanol. The flue gas that exits the steam generator will be reused in the ethanol preheater.

As the use of ethanol requires slightly higher volume flow rates when compared to methane, slightly larger pipes, and fittings are required to keep the fuel pressure within the desired limits. Next to that, ethanol is highly hygroscopic, and oxygen and carbon dioxide are very soluble in ethanol. Therefore it is important to purge the storage tank and to use nitrogen blanketing during storage. This prevents the ethanol from being in contact with water and air. A lot of materials can be used in the fuel system for the implementation of ethanol: stainless steel, carbon steel, non-metals, or ceramics.

From the kinetic modeling study, it was found that ethanol has a lower autoignition delay time than methane. It is not expected that the decrease in autoignition delay time will directly cause autoignition in the mixing zone. For the Siemens SGT5-2000E gas turbine at Killingholme, fuel and air are mixed at a temperature close to 600 K and a pressure of 11 bar. Both ethanol and methane have autoignition delay times larger than 10^5 ms, which are significantly higher than the residence time in the mixing zone. However, due to the existence of recirculation zones, there are regions where the unburned reactants may be heated by the burned products to a temperature of 1000 K. At that temperature, the autoignition delay time of ethanol (10^0 ms) is significantly smaller than that of methane (10^1). This suggests that there is an increased probability of periodic flashes of the fuel-air mixture in the aforementioned regions.

The use of ethanol leads to an increase of 78% of the laminar flame speed, suggesting that the turbulent flame speed will also be significantly larger. However, as the Lewis number of ethanol (1.56) is significantly higher compared to methane (1.0), the difference between the turbulent flame speeds will be lower than was expected based purely on the laminar flame speeds. Next to that, it was found that the use of ethanol leads to a better quality of mixing. Both the increase in turbulent flame speed and the quality of mixing suggest a shorter flame length.

Due to the expected increase in turbulent flame speed and decrease in flame length, there will also be an increased flashback risk when ethanol is used. However, from a comparison with results from an experimental study of hydrogen/methane flames, it is expected that the increased flashback risk of ethanol could be within the flashback margin of the HR3 burner. In contrast to this, it is expected that the increase in turbulent flame speed and decrease in flame length will lead to a decrease in blowoff potential. This offers possibilities regarding the turndown of the gas turbine.

It was found that ethanol has a slightly higher adiabatic flame temperature than methane. As the combustor is controlled at a constant flame temperature, a small reduction in the average equivalence ratio is required when ethanol is used. This will lead to a slight decrease in the energy output, but it will not affect the NOx emissions. Other factors that could affect the NOx emissions are the enhanced mixing and the decreased flame length of ethanol. The enhanced mixing results in lower NOx emissions, where the decrease in flame length leads to higher NOx emissions due to the increase in residence time at higher temperatures. It should also be noted that the fuel-air mixture mixes up to the flame front, meaning that the shorter flame length of ethanol decreases the length of the total mixing section. It is not possible to determine how ethanol exactly affects the NOx emissions based on this research, but from the findings, it is expected that the NOx emissions will be similar compared to methane.

Combustion dynamics are a very complex phenomenon and is still an active area of research in combustion science. Therefore it is hard to determine the exact effect of ethanol on the combustion dynamics. However, due to the shorter flame length of ethanol, it is expected that the 'time lag' will be shorter and the driving energy source of the combustion dynamics will shift to higher frequencies. Combustion tuning would be required to cope with the changes in combustion dynamics.

7.2. Recommendations

This section will discuss some points of improvement for the research, and it will give some suggestions for further research. First of all, the process design was performed for baseload operation. During baseload operation, there is enough energy in the flue gas to evaporate the ethanol. However, during start-up, there is no energy available yet to evaporate the ethanol. Potential solutions could be to use natural gas as a starting fuel or to use an ethanol-fired or electrical boiler to produce enough heat to evaporate the ethanol. The feasibility of these (and other) potential solutions could be evaluated by a techno-economical study.

Another limitation of this research is that only pure ethanol is considered. As was described in Section 4.3, ethanol is highly hygroscopic. The effect of water contents on the combustion characteristics could also be an interesting topic for further research. Next to water, there will also be low content levels of other contaminants, such as organic acids, furan-related compounds, and sulfur compounds [110]. These contaminants could potentially damage the gas turbine hardware, so further research into these effects could be interesting.

The fuel-air mixing study was performed for only a small part of the HR3 burner. However, a CFD study of the complete burner could give more insights regarding the fuel-air mixing effects. Next to that, when combustion is also included in the CFD study, a better comparison between the NOx emissions of ethanol and methane could be made. The extended CFD study could also help in providing more insights regarding the combustion dynamics.

Another interesting option for further research would be the effect of blending natural gas and ethanol. From this research, it can be concluded that both fuels can be used in the lean premix burner, but the effects of blending both fuels are not considered. This could be interesting for scaling down the use of natural gas. Next to that, it is interesting because the production of non-food based ethanol is still rather immature compared to the production of conventional ethanol, meaning that the availability of ethanol could be scarce.

As this research showed some promising results for the implementation of ethanol as a fuel for the lean premix burner, the effect could eventually also be studied by similar high-pressure combustion tests as was performed for hydrogen [103]. The experimental results of such a test could add a lot to the results of this research, which were purely based on models.

Bibliography

[1] Department for Energy Security & Net Zero, *2022 UK greenhouse gas emissions, provisional figures.*, Tech. Rep. (UK Government, 2023).

[2] The Times, *Shell to develop blue hydrogen plant,* https://www.thetimes.co.uk/article/shell-to-develop-blue-hydrogen-plant-xv3ppssj8, accessed: 16-06-2023.

[3] Siemens Energy, *Sgt5-2000e heavy-duty gas turbine (50 hz),* https://www.siemens-energy.com/global/en/offerings/power-generation/gas-turbines/sgt5-2000e.html, accessed: 16-05-2023.

[4] Prade B., Streb H., Berenbrink P., Schnetter B., and Pyka G., *Development of an improved hybrid burner,* Proceedings of the ASME 1996 International Gas Turbine and Aeroengine Congress and Exhibition. **3** (1996).

[5] Moran M.J., Shapiro H.N., Boettner D.D., and Bailey M.B., *Fundamentals of Engineering Thermodynamics*, 7th ed. (John Wiley & Sons, 2011).

[6] Murad J,, *The reynolds number,* https://www.jousefmurad.com/fluid-mechanics/the-reynolds-number/, accessed: 11-12-2023.

[7] Wilcox D.C., *Turbulence Modeling for CFD*, 3rd ed. (DCW Industries, 2006).

[8] Glaude P.A. et al., *Combustion and Oxidation Kinetics of Alternative Gas Turbines Fuels.*, Tech. Rep. (Université de Lorraine, 2014).

[9] Kutkan H., *Modelling Turbulent Premixed CH4/H2/air Flames with Effects of Stretch, Heat Loss and Non-unity Lewis Number for Flame Stabilization and Dynamics.*, Tech. Rep. (University of Genoa, 2022).

[10] Zhen H.S., Leung C.W., and Cheung C.S., *A comparison of the heat transfer behaviors of biogas-h2 diffusion and premixed flames.* Internation Journal of Hydrogen Energy , pp. 1137 (2013).

[11] Benim A.C. and Syed K.J., *Flashback Mechanisms in Lean Premixed Gas Turbine Combustion*, 1st ed. (Academic Press, 2015).

[12] Peters N., *Combustion Theory* (2010).

[13] Dunn-Rankin D., *Lean Combustion*, 1st ed. (Academic Press, 2008).

[14] Fric T.F. and Roshko A., *Vortical structure in the wake of a transverse jet,* Journal of Fluid Mechanics **279**, pp. 1 (1994).

[15] Gupta A.K., Lilley D.G., and Syred N., *Swirl Flows*, 1st ed. (Abacus Press, 1984).

[16] Buijtenen J.P. van, Visser W.P.J, Tinga T., Shakariyants S., and Montella F., *Gas Turbines*, 3rd ed. (TU Delft, 2008).

[17] Lieuwen T.C. and Yang V., *Combustion instabilities in gas turbine engines: Operational experience, fundamental mechanisms, and modeling,* Progress in Astronautics and Aeronautics **210** (2005).

[18] Lefebvre A.H. and Ballal D.R., *Gas Turbine Combustion: Alternative Fuels and Emissions*, 3rd ed. (CRC Press, 2010).

[19] Saravanamuttoo H.I.H., Roger G.F.C., Cohen H., Straznicky P.V., and Nix A.C., *Gas Turbine Theory*, 7th ed. (Pearson, 2017).

[20] Galeazzo F.C.C et al., *Measurement and simulation of turbulent mixing in a jet in crossflow,* Journal of Engineering for Gas Turbines and Power **133** (2011).

[21] Smith G.P. et al., *Gri-mech 3.0,* http://www.me.berkeley.edu/gri_mech/, accessed: 22-05-2023.

[22] United Nations, *The Paris Agreement,* https://www.un.org/en/climatechange/paris-agreement, accessed: 23-05-2023.

[23] Eskin L.D. et al., *LONG-TERM DEMONSTRATION OF A LEAN, PREMIXED, PREVAPORIZED (LPP) SYSTEM FOR GAS TURBINES*, Tech. Rep. (LPP Combustion, 2012).

[24] NIST, *Ethanol,* https://webbook.nist.gov/cgi, accessed: 19-06-2023.

[25] Amiri Y. and Ghasemzadeh K., *Ethanol economy: Environment, demand, and marketing.* Ethanol Science and Engineering , pp. 451 (2019).

[26] Siemens, *Sgt-2000e series,* https://assets.new.siemens.com/siemens/assets/api/uuid:3dfaa18cadfb9d8376a5ed7117c815299892fac3/sgt-2000eseries-brochures.pdf, accessed: 16-06-2023.

[27] Ansys, *Ansys fluent 12.0/12.1 documentation,* https://www.afs.enea.it/project/neptunius/docs/fluent/index.htm, accessed: 25-11-2023.

[28] Pope S.B., *Turbulent Flows*, 1st ed. (Camebridge Univerity Press, 2000).

[29] Menter F.R., *Two-equation eddy-viscosity turbulence models for engineering applications,* AIAA Journal **32** (1994).

[30] Nemitallah M.A., Abdelhafez A.A., and Habib M.A., *Approaches for clean combustion in gas turbines,* Fluid Mechanics and Its Applications **122** (2020).

[31] Wind T., Güthe F., and Syed K., *Co-firing of hydrogen and natural gases in lean premixed conventional and reheat burners (alstom gt26),* Proceedings of ASME Turbo Expo 2014 (2014).

[32] Warnatz J., Maas U., and Dibble R.W., *Combustion: Physical and Chemical Fundamentals, Modeling and Simulation, Experiments, Pollutant Formation*, 4th ed. (Springer, 2006).

[33] Arrhenius S., *Über die reaktionsgeschwindigkeit bei der inversion von rohrzucker durch säuren,* Zeitschrift für Physikalische Chemie **4**, pp. 226 (1889).

[34] Chong C.T. and Ng J.H., *Biojet Fuel in Aviation Applications*, 1st ed. (Elsevier, 2021).

[35] Glassman I. and Yetter R.A., *Combustion*, 4th ed. (Academic Press, 2008).

[36] Law C.K. and Sung C.J., *Structure, aerodynamics, and geometry of premixed flamelets,* Progress in Energy and Combustion Science **26**, 459 (2000).

[37] Williams F.A., *Combustion Theory*, 2nd ed. (CRC Press, 1985).

[38] Markstein G.H., *Nonsteady Flame Propagation*, 1st ed. (Pergamon Press, 1964).

[39] Beeckmann J. et al., *Propagation speed and stability of spherically expanding hydrogen/air flames: Experimental study and asymptotics,* Proceedings of the Combustion Institute **36**, 1531 (2017).

[40] Peters N. and Williams F.A., *The asymptotic structure of stoichiometric methane-air flames.* Combustion and Flame **68**, 185 (1987).

[41] Borghi R., *On the structure and morphology of turbulent premixed flames.* Recent Advances in the Aerospace Science , 117 (1985).

[42] Peters N., *Turbulent Combustion*, 1st ed. (Camebridge University Press, 2000).

[43] Griebel P. et al., *Flow field and structure of turbulent high-pressure premixed methane/air flames.* Proceedings of ASME Turbo Expo 2003 (2003).

[44] Damköhler G., *Der einfluss der turbulenz auf die flammengeschwindigkeit in gasgemischen.* Zeitschrift für Elektrochemie und Angewandte Physikalische Chemie **11**, 601 (1940).

[45] Gülder Ö., *Turbulent premixed flame propagation models for different combustion regimes.* Symposium (international) on Combustion **23**, pp. 743 (1991).

[46] Zeldovich Y.B., *The oxidation of nitrogen in combustion and explosions,* Acta Physicochimica **21**, 577 (1946).

[47] Miller J.A., *Mechanism and modeling of nitrogen chemistry in combustion,* Progress in Energy and Combustion Science **15**, 287 (1989).

[48] Correa S.M., *A review of nox formation under gas-turbine combustion conditions,* Combustion Science Technology **87**, 329 (1993).

[49] Fenimore C.P., *Formation of nitric oxide in premixed hydrocarbon flames,* Symposium (International) on Combustion **13**, 373 (1971).

[50] Hatem F.A., *FLASHBACK ANALYSIS AND AVOIDANCE IN SWIRL BURNERS.*, Tech. Rep. (Cardiff University, 2017).

[51] Brown G.L. and Lopez J.M., *Axisymmetric vortex breakdown part 2. physical mechanisms,* Journal of Fluid Mechanics **221**, 553 (1990).

[52] Rayleigh J.S.W., *The Theory of Sound*, 2nd ed. (Cambridge University Press, 1945).

[53] Leonard G. and Stegmaier J., *Development of an aeroderivative gas turbine dry low emissions combustion system.* Engineering for Gas Turbines and Power **116**, pp. 542 (1994).

[54] Hornsby C. and Norster E.R., *Application of cfd to dln combustion.* Proceedings of the ASME 1997 International Gas Turbine and Aeroengine Congress and Exhibition. Volume 2: Coal, Biomass and Alternative Fuels (1997).

[55] Goodwin D.G., Moffat H.K., Schoegl I., Speth R.L., and Weber B.W., *Cantera: An object-oriented software toolkit for chemical kinetics, thermodynamics, and transport processes,* https://www.cantera.org (2022), version 2.6.0, accessed: 16-05-2023.

[56] Bains M., Hill L., and Rossington P., *Material comparators for end-of-waste decisions. Fuels: Natural Gas.*, Tech. Rep. (Environment Agency, 2016).

[57] Ambrose D., Sprake C.H.S., and Townsend R., *Thermodynamic properties of organic oxygen compounds. xxxvii. vapour pressures of methanol, ethanol, pentan-1-ol, and octan-1-ol from the normal boiling temperature to the critical temperature.* Journal of Chemical Thermodynamics **7**, 185 (1975).

[58] Kliemke H. and Johnke T., *Gas Turbine Modernization – Fuel Conversion and Special Fuel Applications for the Asian Market*, Tech. Rep. (Siemens, 2012).

[59] The Engineering Toolbox, *Fuels - higher and lower calorific values,* https://engineeringtoolbox.com/fuels-higher-calorific-values-d_169.html, accessed: 24-11-2023.

[60] Egware H.O. and Obanor A.I., *The investigation of an sgt5-2000e gas turbine power plant performance in benin city based on energy analysis.* Energy Conversion and Management: X **16** (2022).

[61] Wongsurakul P. et al., *Comprehensive review on potential contamination in fuel ethanol production with proposed specific guideline criteria.* Energies **15**, 2986 (2022).

[62] US Department of Energy, *Handbook for Handling, Storing, and Dispensing E85 and Other Ethanol-Gasoline Blends.*, Tech. Rep. (Government of the United States, 2016).

[63] Singh R., *Ethanol corrosion in pipelines.* Materials Performance **48**, pp. 53 (2009).

[64] Dunphy M.P. and Simmie J.M., *High-temperature oxidation of ethanol. part 1.-ignition delays in shock waves.* Journal of the Chemical Society, Faraday Transactions **87**, 1691 (1991).

[65] Marinov N.M., *A detailed chemical kinetic model for high temperature ethanol oxidation.* International Journal of Chemical Kinetics **31**, 183 (1999).

[66] Saxena P. and Williams F.A., *Numerical and experimental studies of ethanol flames.* Proceedings of the Combustion Institute **31**, 1149 (2007).

[67] Cancino L.R., Fikri M., Oliveira A.A., and Schulz C., *Measurement and chemical kinetics modeling of shock-induced ignition of ethanol– air mixtures.* Energy and Fuels **24**, 2830 (2010).

[68] Ranzi E., Frassoldati A., Grana R., Cuoci A., Faravelli T., Kelley A.P., and Law C.K., *Hierarchical and comparative kinetic modeling of laminar flame speeds of hydrocarbon and oxygenated fuels,* Progress in Energy Combustion Science **38**, pp. 468 (2012).

[69] Metcalfe W.K., Burke S.M., Ahmed S.S., and Curran H.J., *A hierarchical and comparative kinetic modeling study of c1– c2 hydrocarbon and oxygenated fuels.* International Journal of Chemical Kinetics **45**, 638 (2013).

[70] Olm C., Varga T., Valkó É., Hartl S., Hasse C., and Turányi T., *Development of an ethanol combustion mechanism based on a hierarchical optimization approach.* International Journal of Chemical Kinetics **48**, 423 (2016).

[71] Zyada A., *Ethanol Autoignition Modeling And Validation At Wide Ranges Of Mixture Temperatures, Pressures, And Equivalence Ratios Mixture Temperatures, Pressures, And Equivalence Ratios.*, Tech. Rep. (Wayne State University, 2018).

[72] Roy S., *Detailed chemical mechanism generation of oxygenated biofuel*, Tech. Rep. (Mississippi State University, 2021).

[73] Marques C.S.T. and Da Silva J.R.M., *Reduced reaction mechanisms for ethanol under ultra-lean conditions in internal combustion engines,* ACS Omega **6**, 206 (2021).

[74] The Creck Modeling Group - Politecnico di Milano, *C1-c3 + nox mechanism (version 2003, march 2020),* http://creckmodeling.chem.polimi.it/menu-kinetics/menu-kinetics-detailed-mechanisms/107-category-kinetic-mechanisms/400-mechanisms-1911-c1-c3-ht-nox, accessed: 21-06-2023.

[75] Eisazadeh-Far K., Moghaddas A., Al-Mulki J., and Metghalchi H., *Laminar burning speeds of ethanol/air/diluent mixtures.* Proceedings of the Combustion Institute **33**, 1021 (2011).

[76] Gülder Ö., *Laminar burning velocities of methanol, ethanol and isooctane-air mixtures.* Symposium (international) on Combustion , 275 (1982).

[77] Egolfopoulos F.N., Du D.X., and Law C.K., *A study on ethanol oxidation kinetics in laminar premixed flames, flow reactors, and shock tubes.* Symposium (international) on Combustion **24**, 833 (1992).

[78] Dirrenberger P. et al., *Laminar burning velocity of gasolines with addition of ethanol.* Fuel **115**, 162 (2014).

[79] Konnov A.A., Meuwissen R.J., and Goey L.P.H. de, *The temperature dependence of the laminar burning velocity of ethanol flames,* Proceedings of the Combustion Institute **33**, 1011 (2011).

[80] Van Lipzig J.P.J., Nilsson E.J.K., De Goey L.P.H., and Konnov A.A., *Laminar burning velocities of n-heptane, iso-octane, ethanol and their binary and tertiary mixtures.* Fuel **90**, 2773 (2011).

[81] Liao S.Y., Jiang D.M., Huang Z.H., Zeng K., and Cheng Q., *Determination of the laminar burning velocities for mixtures of ethanol and air at elevated temperatures.* Applied Thermal Engineering **27**, 374 (2007).

[82] Bradley D., Lawes M., and Mansour M.S., *Explosion bomb measurements of ethanol–air laminar gaseous flame characteristics at pressures up to 1.4 mpa.* Combustion and Flame **156**, 1462 (2009).

[83] Broustail G. et al., *Experimental determination of laminar burning velocity for butanol/iso-octane and ethanol/iso-octane blends for different initial pressures,* Fuel **106**, 310 (2013).

[84] Katoch A., Millán-Merino A., and Kumar S., *Measurement of laminar burning velocity of ethanol-air mixtures at elevated temperatures,* Fuel **231**, 37 (2018).

[85] Beeckmann J., Cai L., and Pitsch H,, *Experimental investigation of the laminar burning velocities of methanol, ethanol, n-propanol, and n-butanol at high pressure,* Fuel **117**, 340 (2014).

[86] Laich A.R. et al., *High-pressure shock tube study of ethanol oxidation: Ignition delay time and co time-history measurements.* Combustion and Flame (2019).

[87] Mittal G., Burke S.M., Davies V.A., Parajuli B., Metcalfe W.K., and Curran H.J., *Autoignition of ethanol in a rapid compression machine.* Combustion and Flame **161**, 1164 (2014).

[88] Barraza-Botet C.L., Wagnon S.W., and Wooldridge M.S., *Combustion chemistry of ethanol: ignition and speciation studies in a rapid compression facility.* The Journal of Physical Chemistry A **120**, 7408 (2016).

[89] Mathieu O., Pinzón L.T., Atherley T.M., Mulvihill C.R., Schoel I., and Petersen E.L., *Experimental study of ethanol oxidation behind reflected shock waves: Ignition delay time and h2o laser-absorption measurements.* Combustion and Flame **208**, 313 (2019).

[90] Heufer K.A. and Olivier H., *Determination of ignition delay times of different hydrocarbons in a new high pressure shock tube.* Shock Waves **20**, 307 (2010).

[91] Zhang Y. et al., *Probing the low-temperature chemistry of ethanol via the addition of dimethyl ether.* Combustion and Flame **190**, 74 (2018).

[92] Akram M., Saxena P., and Kumar S., *Laminar burning velocity of methane–air mixtures at elevated temperatures.* Energy and Fuels **27**, 3460 (2013).

[93] Dirrenberger P. et al., *Measurements of laminar burning velocities above atmospheric pressure using the heat flux method -application to the case of n-pentane.* Energy and Fuels **29**, 398 (2015).

[94] Rozenchan G., Zhu D.L., Law C.K., and Tse S.D., *Outward propagation, burning velocities, and chemical effects of methane flames up to 60 atm,* Proceedings of the Combustion Institute **29**, 1461 (2002).

[95] Hassan M.I., Aung K.T., Kwon O.C., and Faeth G.M., *Properties of laminar premixed hydrocarbon/air flames at various pressures,* Journal of Propulsion and Power **14** (1998).

[96] Gu X.J. et al., *Laminar burning velocity and markstein lengths of methane–air mixtures.* Combustion and Flame **121**, 41 (2000).

[97] Kurata O., Takahashi S., and Uchiyama Y., *Influence of preheat temperature on the laminar burning velocity of methane-air mixtures.* Journal of Fuels and Lubricants **103**, 1766 (1994).

[98] Goy C.J., Moran A.J., and Thomas G.O., *Autoignition characteristics of gaseous fuels at representative gas turbine conditions.* Proceedings of the ASME Turbo Expo 2001: Power for Land, Sea, and Air. Volume 2: Coal, Biomass and Alternative Fuels; Combustion and Fuels; Oil and Gas Applications; Cycle Innovations. (2001).

[99] Vries J. de and Petersen E.L., *Autoignition of methane-based fuel blends under gas turbine conditions,* Proceedings of the Combustion Institute **31**, 3163 (2007).

[100] Burke U. et al., *An ignition delay and kinetic modeling study of methane, dimethyl ether, and their mixtures at high pressures.* Combustion and Flame **162**, 315 (2015).

[101] Hu E. et al., *Laminar flame speeds and ignition delay times of methane–air mixtures at elevated temperatures and pressures.* Fuel **158**, 1 (2015).

[102] Zhang Y. et al., *Experimental and modeling study on ignition delays of lean mixtures of methane, hydrogen, oxygen, and argon at elevated pressures.* Combustion and Flame **159**, 918 (2012).

[103] Blaette et al., *Sgt5-4000f hydrogen capability – high pressure combustion rig tests.* Proceedings of ASME Turbo Expo 2023 (2023).

[104] Eroglu A. et al., *Hydrogen capabilities of siemens energy gas turbines, an oem perspective,* 10th International Gas Turbine Conference (2021).

[105] Bouvet et al., *On the effective lewis number formulations for lean hydrogen/hydrocarbon/air mixtures,* International Journal of Hydrogen Energy **38**, pp. 5949 (2013).

[106] Shih T.H. et al., *A new $k-\epsilon$ eddy viscosity model for high reynolds number turbulent flows.* Computer Fluids **24**, 227 (1995).

[107] Karvinen A. and Ahlstedt H., *Comparison of turbulence models in case of jet in crossflow using commercial cfd code,* Engineering Turbulence Modelling and Experiments **6** (2005).

[108] Soroush A., *CFD evaluation of a jet in cross flow related to a gas turbine burner.*, Tech. Rep. (Chalmers University of Technology, 2012).

[109] SimsScale, *Defining turbulent boundary conditions,* https://www.simscale.com/forum/t/defining-turbulent-boundary-conditions/80895, accessed: 31-12-2023.

[110] Habe H. et al., *Chemical analysis of impurities in diverse bioethanol samples,* Journal of the Japan Petroleum Institute **56**, pp. 414 (2013).

A

Two Equation Turbulence Models

A.1. Realizable k-ϵ Model

Transport Equations

"The modeled transport equations for the realizable k-ϵ model are [27, 106]:

$$\frac{\partial}{\partial t}(\rho k) + \frac{\partial}{\partial x_i}(\rho u_i k) = \frac{\partial}{\partial x_j}\left[(\mu + \sigma_k \mu_t)\frac{\partial k}{\partial x_j}\right] + G_k + G_b - \rho\epsilon - Y_M + S_k \tag{A.1}$$

and

$$\frac{\partial}{\partial t}(\rho \epsilon) + \frac{\partial}{\partial x_i}(\rho u_i \epsilon) = \frac{\partial}{\partial x_j}\left[(\mu + \sigma_\epsilon \mu_t)\frac{\partial \epsilon}{\partial x_j}\right] + C_{1\epsilon}\frac{\epsilon}{k}G_b + S_\epsilon \tag{A.2}$$

where

$$C_1 = \max\left[0.43, \frac{\eta}{\eta + 5}\right], \qquad \eta = S\frac{k}{\epsilon}, \qquad S = \sqrt{2S_{ij}S_{ij}} \tag{A.3}$$

In these equations, G_k represents the generation of turbulence kinetic energy due to the mean velocity gradient, G_b is the generation of turbulence kinetic energy due to buoyancy, Y_M represents the contribution of the fluctuating dilatation in compressible turbulence to the overall dissipation rate, and C_2 and $C_{1\epsilon}$ are constants. σ_k and σ_ϵ are the turbulent Prandtl numbers for k and ϵ, respectively. S_k and S_ϵ are user-defined source terms.

This model has been extensively validated for a wide range of flows. The performance of the model has been found to be substantially better than that of the standard k-ϵ model. Especially noteworthy is the fact that the realizable k-ϵ model resolves the round-jet anomaly; i.e., it predicts the spreading rate for axisymmetric jets as well as that for planar jets.

Modeling the Turbulent Viscosity

As in other k-ϵ models, the eddy viscosity is computed from:

$$\mu_t = \rho C_\mu \frac{k^2}{\epsilon} \tag{A.4}$$

The difference between the realizable k-ϵ model and the standard and RNG k-ϵ models is that C_μ is no longer constant. It is computed from:

$$C_\mu = \frac{1}{A_0 + A_s\frac{kU^*}{\epsilon}} \tag{4.4-18}$$

where

$$U^* \equiv \sqrt{S_{ij}S_{ij} + \widetilde{\Omega}_{ij}\widetilde{\Omega}_{ij}}, \qquad \widetilde{\Omega}_{ij} = \Omega_{ij} - 2\epsilon_{ijk}\omega_k, \qquad \Omega_{ij} = \overline{\Omega_{ij}} - \epsilon_{ijk}\omega_k \tag{A.5}$$

where $\overline{\Omega_{ij}}$ is the mean rate-of-rotation tensor viewed in a rotating reference frame with the angular velocity ω_k. The model constants A_0 and A_s are given by:

$$A_0 = 4.04, \qquad A_s = \sqrt{6}\cos\phi \qquad \phi = \frac{1}{3}\cos^{-1}(\sqrt{6}W), \qquad W = \frac{S_{ij}S_{ij}}{2} - \frac{\partial u_j}{\partial x_i} + \frac{\partial u_i}{\partial x_j} \tag{A.6}$$

It can be seen that C_μ is a function of the mean strain and rotation rates, the angular velocity of the system rotation, and the turbulence fields (k and ϵ).

Model Constants

The model constants C_2, σ_k, and σ_ϵ have been established to ensure that the model performs well for certain canonical flows. The model constants are:

$$C_{1\epsilon} = 1.44, \qquad C_2 = 1.9, \qquad \sigma_k = 1.0, \qquad \sigma_\epsilon = 1.2 \tag{A.7}$$

A.2. SST k-ω Model

Transport Equations

The transport equations for the SST k-ω model are [27, 29]:

$$\frac{\partial}{\partial t}(\rho k) + \frac{\partial}{\partial x_i}(\rho u_i k) = \frac{\partial}{\partial x_j}\left((\mu + \frac{\mu_t}{\sigma_k})\frac{\partial k}{\partial x_j}\right) + \widetilde{G}_k - Y_k + S_k \tag{A.8}$$

and

$$\frac{\partial}{\partial t}(\rho \omega) + \frac{\partial}{\partial x_i}(\rho u_i \omega) = \frac{\partial}{\partial x_j}\left((\mu + \frac{\mu_t}{\sigma_\omega})\frac{\partial \omega}{\partial x_j}\right) + G_\omega - Y_\omega + D_\omega + S_\omega \tag{A.9}$$

In these equations, $\widetilde{G}_k$ represents the generation of turbulence kinetic energy due to mean velocity gradients, G_ω represents the generation of ω, Γ_k and Γ_ω represent the effective diffusivity of k and ω, respectively. Y_k and Y_ω represent the dissipation of k and ω due to turbulence, D_ω represents the cross-diffusion term, and S_k and S_ω are user-defined source terms.

Modeling the Effective Diffusivity

The effective diffusivities for the SST k-ω model are given by:

$$\Gamma_k = \mu + \frac{\mu_t}{\sigma_k}, \qquad \Gamma_\omega = \mu + \frac{\mu_t}{\sigma_\omega} \tag{A.10}$$

where σ_k and σ_ω are the turbulent Prandtl numbers for k and ω, respectively. The turbulent viscosity, μ_t, is computed as follows:

$$\mu_t = \frac{\rho k}{\omega}\frac{1}{\max\left[\frac{1}{\alpha^*}, \frac{SF_2}{a_1\omega}\right]} \tag{A.11}$$

where S is the strain rate magnitude and:

$$\sigma_k = \frac{1}{F_1/\sigma_{k,1} + (1-F_1)/\sigma_{k,2}}, \qquad \sigma_\omega = \frac{1}{F_1/\sigma_{\omega,1} + (1-F_1)/\sigma_{\omega,2}} \tag{A.12}$$

The blending functions, F_1 and F_2, are given by:

$$F_1 = \tanh\left(\Phi_1^4\right), \qquad \Phi_1 = \min\left[\max\left(\frac{\sqrt{k}}{0.09\omega y}, \frac{500\mu}{\rho y^2 \omega}\right), \frac{4\rho k}{\sigma_{\omega,2} D_\omega^+ y^2}\right], \qquad D_\omega^+ = \max\left[2\rho \frac{1}{\sigma_{\omega,2}} \frac{1}{\omega} \frac{\partial k}{\partial x_j} \frac{\partial \omega}{\partial x_j}, 10^{-10}\right] \tag{A.13}$$

and

$$F_2 = \tanh\left(\Phi_2^2\right), \qquad \Phi_2 = \max\left[2\frac{\sqrt{k}}{0.09\omega y}, \frac{500\mu}{\rho y^2 \omega}\right] \tag{A.14}$$

where y is the distance to the next surface, and D_ω^+ is the positive portion of the cross-diffusion term.

Modeling the Turbulence Production

The term $\widetilde{G}_k$ represents the production of turbulence kinetic energy k and is defined as:

$$\widetilde{G}_k = \min(G_k, 10\rho\beta^* k\omega) \tag{A.15}$$

where G_k is defined in the same manner as in the standard k-ω model.

The term G_ω represents the production of ω and is given by:

$$G_\omega = \frac{\alpha}{\nu_t}\widetilde{G}_k \tag{A.16}$$

Modeling the Turbulence Dissipation

The term Y_k represents the dissipation of turbulence kinetic energy k and is defined as:

$$Y_k = \rho\beta^* k\omega \tag{A.17}$$

The term Y_ω represents the dissipation of ω and is defined as:

$$Y_\omega = \rho\beta\omega^2 \tag{A.18}$$

Instead of having a constant value, β_i is given by:

$$\beta_i = F_1\beta_{i,1} + (1 - F_1)\beta_{i,2} \tag{A.19}$$

Cross-Diffusion Modification

The SST k-ω model is based on both the standard k-ω model and the standard k-ϵ model. To blend these two models together, the standard k-ϵ model has been transformed into equations based on k and ω, which leads to the introduction of a cross-diffusion term D_ω, which is defined as:

$$D_\omega = 2\left(1 - F_1\right)\rho\sigma_{\omega,2}\frac{\partial k}{\partial x_j}\frac{\partial \omega}{\partial x_j} \tag{A.20}$$

Model Constants

The model constants for the SST k-ω model are:

$$\sigma_{k,1} = 1.176, \qquad \sigma_{\omega,1} = 2.0, \qquad \sigma_{k,2} = 1.0, \qquad \sigma_{\omega,2} = 1.168, \qquad a_1 = 0.31, \qquad \beta_{i,1} = 0.075, \qquad \beta_{i,2} = 0.0828 \tag{A.21}$$

All additional model constants (α_∞^*, α_∞, α_0, β_∞^*, R_β, R_k, R_ω, ζ^*, and M_{t0}) have the same values as for the standard k-ω model.

B

Python Code for Kinetic Modeling Study

B.1. Laminar Flame Speed versus Equivalence Ratio

```
import cantera as ct
import numpy as np
import matplotlib.pyplot as plt
import scipy

mechanism = 'CRECK1.yaml'
fuel_ethanol = 'C2H5OH' #Ethanol
fuel_methane = 'CH4' #Methane


T = 599.3961543  # [K] Temperature of the mixture
p = 11.1732*10**5  # [Pa] Pressure of the mixture

phi = []; #[-] Equivalence Ratio of the mixture
phi_i = 0.3; phi_max = 1.12; phi_incr = 0.02

ethanol = ct.Solution(mechanism)
sl_ethanol=[]; Tmax_ethanol=[]
Le_eff_ethanol =[]; Le_F_ethanol =[]; Le_O2_ethanol =[]
rhosl_ethanol = []; inv_tad_ethanol = []

methane = ct.Solution(mechanism)
sl_methane=[]; Tmax_methane = []
Le_eff_methane =[]; Le_F_methane =[]; Le_O2_methane =[]
rhosl_methane = []; inv_tad_methane = []


print('   phi (-)       Sl (m/s)     Tmax (K)')
phi_x = phi_i
while phi_x <= phi_max:
        ethanol.TP = T, p
        ethanol.set_equivalence_ratio(phi_x, fuel_ethanol, 'o2:1.0, n2:3.76')
        rho = ethanol.density_mass
        D_th = ethanol.thermal_conductivity/ethanol.density_mass/ethanol.cp_mass
        Le_F = D_th/ethanol.mix_diff_coeffs_mass[ethanol.species_index('C2H5OH')]
        Le_O2 = D_th/ethanol.mix_diff_coeffs_mass[ethanol.species_index('O2')]

        initial_grid = np.linspace(0, 0.03, 7)
        f_ethanol = ct.FreeFlame(ethanol, initial_grid)
        f_ethanol.transport_model = 'Mix'
        f_ethanol.set_refine_criteria(ratio=5, slope=0.2, curve=0.2, prune=0.0)
        f_ethanol.solve(loglevel=1, auto=True)
        rhosl = np.log(rho*f_ethanol.velocity[0])
        inv_tad = 1/max(f_ethanol.T)
```

```
        Le_F_ethanol.append(Le_F)
        Le_O2_ethanol.append(Le_O2)
        phi.append(phi_x)
        sl_ethanol.append(f_ethanol.velocity[0])
        Tmax_ethanol.append(max(f_ethanol.T))
        rhosl_ethanol.append(rhosl)
        inv_tad_ethanol.append(inv_tad)
        print('%10.3f %10.3f %10.3f' % (phi_x, f_ethanol.velocity[0], max(f_ethanol.T)))
        output_file1.write(str(phi_x) + '\t' + str(f_ethanol.velocity[0]) + '\t' + str(max(
                                                    f_ethanol.T)) + '\n')
        phi_x = phi_x + phi_incr


phi_x = phi_i
while phi_x <= phi_max:
        methane.TP = T, p
        methane.set_equivalence_ratio(phi_x, fuel_methane, 'o2:1.0, n2:3.76')
        rho = methane.density_mass
        D_th = methane.thermal_conductivity/methane.density_mass/methane.cp_mass
        Le_F = D_th/methane.mix_diff_coeffs_mass[methane.species_index('CH4')]
        Le_O2 = D_th/methane.mix_diff_coeffs_mass[methane.species_index('O2')]

        initial_grid = np.linspace(0, 0.03, 7)
        f_methane = ct.FreeFlame(methane, initial_grid)
        f_methane.transport_model = 'Mix'
        f_methane.set_refine_criteria(ratio=5, slope=0.2, curve=0.2, prune=0.0)
        f_methane.solve(loglevel=1, auto=True)
        rhosl = np.log(methane.density_mass*f_methane.velocity[0])
        inv_tad = 1/max(f_methane.T)

        Le_F_methane.append(Le_F)
        Le_O2_methane.append(Le_O2)
        sl_methane.append(f_methane.velocity[0])
        Tmax_methane.append(max(f_methane.T))
        rhosl_methane.append(rhosl)
        inv_tad_methane.append(inv_tad)
        print('%10.3f %10.3f %10.3f' % (phi_x, f_methane.velocity[0], max(f_methane.T)))
        output_file1.write(str(phi_x) + '\t' + str(f_methane.velocity[0]) + '\t' + str(max(
                                                    f_methane.T)) + '\n')
        phi_x = phi_x + phi_incr

inv_tad_ethanol = np.array(inv_tad_ethanol)
rhosl_ethanol = np.array(rhosl_ethanol)
sorted_idxs = np.argsort(inv_tad_ethanol)
arr11 = inv_tad_ethanol[sorted_idxs]
arr22 = rhosl_ethanol[sorted_idxs]
coeff = np.polyfit(arr11,arr22,1)
ER_ethanol = -2*coeff[0]

inv_tad_methane = np.array(inv_tad_methane)
rhosl_methane = np.array(rhosl_methane)
sorted_idxs = np.argsort(inv_tad_methane)
arr11 = inv_tad_methane[sorted_idxs]
arr22 = rhosl_methane[sorted_idxs]
coeff = np.polyfit(arr11,arr22,1)
ER_methane = -2*coeff[0]

for i in range(len(phi)):
    beta_ethanol= ER_ethanol*(Tmax_ethanol[i]-T)/(Tmax_ethanol[i]**2)
    beta_methane = ER_methane * (Tmax_methane[i] - T) / (Tmax_methane[i] ** 2)
    if phi[i]<1:
        PHI = 1/phi[i] # capital phi
        Le_E_ethanol = Le_O2_ethanol[i]
        Le_D_ethanol = Le_F_ethanol[i]
        Le_E_methane = Le_O2_methane[i]
        Le_D_methane = Le_F_methane[i]
    else:
        PHI = phi[i]
        Le_E_ethanol = Le_F_ethanol[i]
        Le_D_ethanol = Le_O2_ethanol[i]
        Le_E_methane = Le_F_methane[i]
```

```
        Le_D_methane = Le_O2_methane[i]

    A_ethanol = 1 + beta_ethanol * (PHI - 1)
    A_methane = 1 + beta_methane * (PHI - 1)

    Le_ethanol = 1 + ((Le_E_ethanol - 1) + (Le_D_ethanol - 1) * A_ethanol) / (1 + A_ethanol)
    Le_methane = 1 + ((Le_E_methane - 1) + (Le_D_methane - 1) * A_methane) / (1 + A_methane)

    Le_eff_ethanol.append(Le_ethanol)
    Le_eff_methane.append(Le_methane)

plt.figure(1)
plt.plot(phi, sl_ethanol, 'b-')
plt.plot(phi, sl_methane, 'r-')
plt.xlabel('Equivalence ratio [-]')
plt.ylabel('Laminar burning velocity [m/s]')

plt.figure(2)
plt.plot(phi, Tmax_ethanol, 'b-')
plt.plot(phi, Tmax_methane, 'r-')
plt.xlabel('Equivalence ratio [-]')
plt.ylabel('Adiabatic Temperature [K]')

plt.figure(3)
plt.plot(phi, Le_eff_ethanol, 'b-')
plt.plot(phi, Le_eff_methane, 'r-')
plt.xlabel('Equivalence ratio [-]')
plt.ylabel('Effective Lewis Number [-]')

plt.show()
```

B.2. Autoignition Delay Time versus Temperature: Ethanol

```
import matplotlib.pyplot as plt
import cantera as ct
import numpy as np

mechanism = 'CRECK1.yaml'
gas = ct.Solution(mechanism)
fuel = 'C2H5OH'


Ti = 500; Tmax = 1510; T_incr = 10
T = np.arange(Ti,Tmax,T_incr)
p = 11.1732*10**5
phi =0.5;



Ti_log = []; IDT_log = []
IDT = []
print('   Ti (K)      IDT (ms)   ')
for i in range(len(T)):
    T_i = T[i]
    gas.TP = T_i, p
    gas.set_equivalence_ratio(phi, fuel, 'o2:1.0, n2:3.76')


    r = ct.IdealGasReactor(gas)
    sim = ct.ReactorNet([r])

    sim.rtol = 1.0e-4
    sim.atol = 1.0e-15
    if T[i] >= 900:
        max_time = 10
        sim.max_time_step = 5e-4
    elif T[i] >=700 and T[i]<900:
        max_time = 100
        sim.max_time_step = 5e-3
```

```
    elif T[i] >=600 and T[i]<700:
        max_time = 1000
        sim.max_time_step = 5e-2
    elif T[i] >=550 and T[i]<600:
        max_time = 100000
        sim.max_time_step = 5e0
    elif T[i] >=500 and T[i]<550:
        max_time = 1000000
        sim.max_time_step = 5e1
    else:
        max_time = 100000000
        sim.max_time_step = 5e3
    n=0; t=0.0; max_OH = 0.0

    states = ct.SolutionArray(gas, extra=['t'])

    while sim.time < max_time:
        sim.step()
        states.append(r.thermo.state, t=1000*sim.time)
        if gas['oh'].concentrations > max_OH:
            max_OH = gas['oh'].concentrations
            max_OH_locator = n
        n = n+1
    for j in range(n):
        if j == max_OH_locator:
            IDT=states.t[j]

    Ti_log.append(1000/(T_i*1.0))
    IDT_log.append(IDT)
    print('1/T(', i,') =',Ti_log[i])
    print('IDT(',i,')=',IDT_log[i])



plt.semilogy(Ti_log, IDT_log, 'b-')


plt.ylabel('IDT (ms)')
plt.xlabel('1000/T')
plt.show()
```

B.3. Autoignition Delay Time versus Temperature: Methane

```
import matplotlib.pyplot as plt
import cantera as ct
import numpy as np

mechanism = 'CRECK1.yaml'
gas = ct.Solution(mechanism)
fuel = 'CH4'


Ti = 550; Tmax = 1510; T_incr = 10
T = np.arange(Ti,Tmax,T_incr)
p = 11.1732*10**5
phi =1;



Ti_log = []; IDT_log = []
IDT = []
print('   Ti (K)      IDT (ms)   ')
for i in range(len(T)):
    T_i = T[i]
    gas.TP = T_i, p
    gas.set_equivalence_ratio(phi, fuel, 'o2:1.0, n2:3.76')


    r = ct.IdealGasReactor(gas)
```

```
    sim = ct.ReactorNet([r])

    sim.rtol = 1.0e-4
    sim.atol = 1.0e-15
    if T[i] >= 900:
        max_time = 1
        sim.max_time_step = 5e-5
    elif T[i] >=800 and T[i]<900:
        max_time = 10
        sim.max_time_step = 5e-4
    elif T[i] >=700 and T[i]<800:
        max_time = 100
        sim.max_time_step = 5e-3
    elif T[i] >=650 and T[i]<700:
        max_time = 10000
        sim.max_time_step = 5e-1
    elif T[i] >=550 and T[i]<650:
        max_time = 100000
        sim.max_time_step = 5
    n=0; t=0.0; max_OH = 0.0

    states = ct.SolutionArray(gas, extra=['t'])

    while sim.time < max_time:
        sim.step()
        states.append(r.thermo.state, t=1000*sim.time)
        if gas['oh'].concentrations > max_OH:
            max_OH = gas['oh'].concentrations
            max_OH_locator = n
        n = n+1
    for j in range(n):
        if j == max_OH_locator:
            IDT=states.t[j]

    Ti_log.append(1000/(T_i*1.0))
    IDT_log.append(IDT)
    print('1/T(', i,') =',Ti_log[i])
    print('IDT(',i,')=',IDT_log[i])



plt.semilogy(Ti_log, IDT_log, 'b-')


plt.ylabel('IDT (ms)')
plt.xlabel('1000/T')
plt.show()
```